

國立交通大學

電子工程學系 電子研究所

博士論文

氮化銦鎵/氮化鎵雷射二極體之理論研究



Theoretical Studies of InGaN/GaN Laser Diodes

研究生：黃士哲

指導教授：顏順通 教授

中華民國九十七年一月

氮化銦鎵/氮化鎵雷射二極體之理論研究

Theoretical Studies of InGaN/GaN Laser Diodes

研究生：黃士哲

Student : Shyh-Jer Huang

指導教授：顏順通

Advisor : Shun-Tung Yen

國立交通大學

電子工程學系 電子研究所



Submitted to Department of Electronics Engineering and
Institute of Electronics
College of Electrical and Computer Engineering
National Chiao Tung University
in partial Fulfillment of the Requirements
for the Degree of
Doctor of Philosophy
in
Electronics Engineering

January 2007

Hsinchu, Taiwan, Republic of China

中華民國九十七年一月

氮化銦鎵/氮化鎵雷射二極體之 理論研究

研究生：黃士哲

指導教授：顏順通 博士

國立交通大學電子工程學系暨研究所



本論文中，我們對氮化銦鎵/氮化鎵雷射二極體的活性區以及 p 型包覆層作理論性探討。在活性區方面，我們討論了溢出載子對臨界電流密度、增益頻譜以及自發性放射頻譜的影響，同時利用 p 型摻雜來降低溢出載子的負面效應。包覆區方面，我們分析氮化鋁鎵/氮化鎵超晶格的結構，找出造成高垂直阻抗的主要因素，並且提供最佳化的結構參數。

我們利用能量在量子井能障之上的綿密不連續次能帶來近似連續能帶，當載子溢出量子井時即佔據在這些能帶上。計算結果顯示，有

沒有考慮這些連續能帶，對輻射電流密度以及增益頻譜都有顯著差異。我們進一步探討在改變量子井寬度或深度、共振腔損耗及溫度時，載子溢出效應對輻射電流密度、增益頻譜跟自發性放射頻譜所造成的影響。對較淺的量子井而言，這個效應特別明顯。它會使得自發性放射頻譜變寬，進而增加雷射二極體的臨界電流。較長的共振腔以及多層量子井可以有效的降低溢出載子所造成的負面效應。我們提供了在考慮溢出載子效應下最佳的量子井寬度以及層數。此外，為了更進一步降低臨界電流，我們探討活性區中引入 n 型與 p 型摻雜對雷射的影響。結果顯示，p 型摻雜不但能有效降低因為溢出電子所造成的漏電流，而且可以讓增益頻譜變成更往峰值集中，能更有效率產生雷射光。而 n 型摻雜則恰恰產生相反的結果。我們進一步提出高 p 型摻雜的單量子井為最佳化結構，如果高 p 型摻雜在實作上不容易達成，則低濃度 p 型摻雜的雙量子井為最佳結構。

除了活性區，我們也對 p 型端的氮化鋁鎵/氮化鎵超晶格結構作最佳化。為了探討超晶格的垂直電阻，我們利用飄移擴散、穿隧以及熱放射電流方程式建立計算模型。我們發現造成高垂直電阻的主要因素是超晶格中能障的數量。即使這些能障能有效的提升 p 型雜質的解離率，它們本身卻形成電洞移動時主要的障礙。當這些能障夠窄，使得電洞在跨越能障時的散射效應可以忽略時，較寬的能障寬度反而能得到較小的垂直阻抗。我們的結果顯示，在能障的鋁濃度為 20% 且氮化鎵寬度固定 2 奈米時，當能障的寬度從 2 奈米增加到 6 奈米，垂直阻抗可以降低大概 50%。

Theoretical Studies of InGaN/GaN Laser Diodes

Student : Shyh-Jer Huang

Advisors : Dr. Shun-Tung Yen

Department of Electronics Engineering & Institute of Electronics
Engineering
National Chiao Tung University



ABSTRACT

In this dissertation, the InGaN/GaN laser diode is theoretically studied. We have optimized its active region and the cladding layer composed of a *p*-type AlGaIn/GaN superlattice by studying the spillover effect, the influence of dopants, and the key factor making the vertical resistance of the *p*-type superlattice large.

The effects of electron spillover from quantum wells on the optical property of InGaIn/GaN laser diodes are theoretically studied in detail. Six-band model including strain effect is used to calculate valence band states. Continuous subbands are simulated

deliberately by dense discretized subbands for the spillover electrons. The calculation results show obvious differences in the radiative current densities and the gain spectra between the cases with and without considering the spillover effect. We further investigate the spillover effect on the radiative current densities and the spontaneous emission spectra, with variations in the depth and the width of quantum wells, the total loss of the cavity, and the temperature. For shallow wells, the spillover effect is particularly important. It broadens both the gain and the spontaneous emission spectra and hence deteriorates the threshold of laser diodes. Such an effect can be alleviated by employing lasers with a long cavity and a multi-quantum-well active region. The concepts of the electron spillover studied in this work are not only applicable to the nitride lasers, but also to other kinds of quantum-well lasers.

The influences of the modulation-doping in InGaN/GaN laser diodes are also theoretically studied with the effects of electron spillover from quantum wells considered. The calculation results show that the threshold current can be significantly reduced by *p*-type modulation-doping around the wells but not by *n*-type doping, supposed that the layers are of a perfect quality and the impurity-induced defects are ignored. Also, the *p*-type modulation doping can make the threshold current more insensitive to the cavity loss compared with other cases. An optimized threshold current density can be achieved for single-quantum-well lasers by introducing *p*-type dopants. However, the dopant concentration is high and may be inaccessible. For double-quantum-well lasers an optimized low threshold current can be achieved with a slighter and practicable *p*-type doping level.

We also study the vertical transport of holes through *p*-type AlGaIn/GaN superlattices with both Ga- and N-face polarities by drift-diffusion, tunneling, and thermionic emission models to find the key factors that dominantly influence the average

vertical resistivity at different temperatures. It is shown that although the acceptors in the barriers are easily ionized to give a high spatially averaged density of holes, the barriers themselves are the main obstacle to the transport of holes through the superlattices. In our calculation results, the number of barriers in the superlattices dominantly affects the average vertical resistivity if the barriers are thin enough. So the resistivity can be reduced by decreasing the barrier number for a fixed total length of superlattices. Our results show that about 50% reduction in the resistivity can be expected when the structure varies from $\text{Al}_{0.11}\text{Ga}_{0.8}\text{N}(2\text{ nm})/\text{GaN}(2\text{ nm})$ to $\text{Al}_{0.11}\text{Ga}_{0.8}\text{N}(6\text{ nm})/\text{GaN}(2\text{ nm})$.



Acknowledgements

首先我要感謝顏順通教授的費心指導。如果沒有他犧牲自己的時間跟精神，我便無法察覺研究過程中的錯誤跟盲點，更無法完成博士生生涯中的所有研究。另外我想感謝實驗室的學弟妹們。雖然大家來來去去，相處時間短暫，但在需要相互扶持鼓勵的時候，大家總是毫不吝嗇的付出關懷。最後我想感謝我的父母跟兩個妹妹，不時地給我心裡溫暖的支持。



CONTENTS

ABSTRACT (Chinese)	i
ABSTRACT (English)	iii
ACKNOWLEDGMENTS	vi
CONTENTS	vii
TABLE CAPTIONS	ix
FIGURE CAPTIONS	x

CHAPTER 1 INTRODUCTION

1.1 Milestones of developing nitride-based optical devices	1
1.2 Motivation and background	12

CHAPTER 2 CALCULATION MEHTOD

2.1 Piezoelectric and spontaneous polarization	16
2.2 Band structure of quantized heterojunction	19
2.3 Calculation method for optical properties	26
2.4 Current transport in <i>p</i>-type layers	31
2.5 Numerical methods	34

CHAPTER 3 RADIATIVE LEAKAGE CURRENT

3.1 Some assumptions and definitions	41
3.2 Result and Discussion	43
3.3 Summary	71

CHAPTER 4 VERTICAL RESISTIVITY OF THE SUPERLATTICE

4.1 Some assumptions and definitions	73
4.2 Result and Discussion	74
4.3 Summary	83

CHAPTER 5 CONCLUSION AND SUGGESTION

5.1 Conclusion 84

5.2 Suggestion for Future Work 85

REFERENCE 87

VITA 94

PUBLICATION LIST 95



TABLE CAPTIONS

CHAPTER 1

Table 1.1 Key events of the development of nitride-based LED and LD (p.10)

CHAPTER 2

Table 2.1 Material parameters for $\mathbf{k} \cdot \mathbf{p}$ Luttinger-Kohn Hamiltonian used here (p.39)



FIGURE CAPTIONS

CHAPTER 1

Fig. 1.1 Bandgap energy of GaN, AlN, InN, and their ternary compounds or possible quaternary compounds as a function of the lattice constants (p.2)

Fig. 1.2 Schematic principle figure of two-flow MOCVD (p.4)

Fig. 1.3 Schematic diagram of the substrate for ELOG. in A. Usui's paper (p.4)

Fig. 1.4 (a) Cross section of the LD fabricated on ELOG substrate. (b) The schematic diagram of (a) (p.5)

Fig. 1.5 Resistivity of Mg-doped GaN films as a function of thermal annealing temperature. (p.7)

Fig. 1.6 Schematic valence band diagram of a AlGa_xN/GaN superlattice. (p.9)

Fig. 1.7 Free hole concentration against reciprocal temperature for Al_xGa_{1-x}N/GaN doped superlattices with x=10 and 20% aluminium content as well as carrier concentration in p-type bulk GaN sample. (i) E_a = 58 meV (Al_{0.2}Ga_{0.8}N/GaN); (ii) E_a = 70 meV (Al_{0.1}Ga_{0.9}N/GaN); (iii) E_a = 200 meV (p-type GaN). (p.9)

Fig. 1.8 The general structure of nitride-based laser diodes. (p.11)

CHAPTER 2

Fig. 2.1 Schematic drawing of the crystal structure of wurtzite Ga-face and N-face GaN (p.17)

Fig. 2.2 Orientation of the spontaneous and piezoelectric polarization in pseudomorphic grown wurtzite AlGa_xN/GaN and InGa_xN/GaN heterostructures with Ga- or N-face polarity. (p.18)

Fig. 2.3 Illustration of possible paths for holes flowing through the barriers. The valence band profile E_v considering piezoelectric field with Ga-face polarity is drawn as an example. W_1 and W_2 are the symbols for well 1 and well 2, respectively. B_{12} is the barrier between W_1 and W_2 . $J_{\text{tunneling}}$ and $J_{\text{thermionic}}$ are the F-N tunneling and thermionic emission current densities, respectively. (p.33)

Fig. 2.4 Flow diagram for Jacobian-Newton iteration. (p.38)

CHAPTER 3

Fig. 3.1 Schematic illustration of the band diagram of the neighborhood of the InGaN/GaN QW active region inside which four different kinds (bb , cb , bc , and cc) of interband processes occur. The cb (bb) process means the interband process between the continuous (bound) conduction and the bound valence subbands while the bc (cc) means the process between the bound (continuous) conduction and the continuous valence subbands. The well has a width L_w and the active region has a width L_a . The continuous subbands are simulated by dense discrete subbands that are discretized using two infinite potential boundaries. An AlGaIn EBL is placed immediately near the active region. (p.40)

Fig. 3.2 The current densities, J , J_{bb} , and J_0 , versus the peak gain for In_{0.2}Ga_{0.8}N/GaN single-QW LDs with well width $L_w = 3.6$ and 5.4 nm, assuming the partition ratio $Q_v = 0.33$ in panel (a) and $Q_v = 0.45$ in panel (b). The J is the total current density, the J_{bb} is due to the bb process, and the J_0 is calculated without considering the continuous subbands. (p.45)

Fig. 3.3 The gain spectra at threshold for In_{0.2}Ga_{0.8}N/GaN single-QW structures with $L_w = 3.6$ nm, assuming $Q_v = 0.33$ in panel (a) and $Q_v = 0.45$ in panel (b). The spectra g are the total gain, the spectra g_{bb} (g_{cb}) are due to the bb (cb) process, and the ones g_0 are obtained without considering the continuous subbands. Inseted is an illustration of the conduction band profile of the QW with the level of the lowest bound subband edge (level 1) and that of the lowest quasi-bound

subband edge (level 2). (p.47)

Fig. 3.4 The spectra of spontaneous emission rates at threshold for $\text{In}_{0.2}\text{Ga}_{0.8}\text{N}/\text{GaN}$ single-QW structures with $L_w = 3.6$ and 5.4 nm, assuming $Q_v = 0.33$ in panel (a) and $Q_v = 0.45$ in panel (b). The spectra r_{sp} are the total spontaneous emission rate and the ones $r_{sp,bb}$ ($r_{sp,cb}$) are due to the bb (cb) process. (p.49)

Fig. 3.5 The ratio J_{cb}/J for $\text{In}_{0.2}\text{Ga}_{0.8}/\text{GaN}$ single-QW LDs at threshold versus the well width L_w with Q_v as a variable parameter ($Q_v = 0.33, 0.37, 0.41$, and 0.45). The dashed line indicates the boundary across which the lowest quasi-bound subband changes to a bound subband. (p.51)

Fig. 3.6 The current densities J and J_{bb} for $\text{In}_{0.2}\text{Ga}_{0.8}/\text{GaN}$ single-QW LDs at threshold as a function of L_w for $Q_v = 0.33$ and 0.45 . (p.51)

Fig. 3.7 The ratio J_{cb}/J for $\text{In}_{0.2}\text{Ga}_{0.8}/\text{GaN}$ single-QW LDs at threshold versus the well width L_w for $Q_v = 0.33$ and 0.45 with the cavity loss α as a variable parameter ($\alpha = 40, 60$, and 80 cm^{-1}). (p.53)

Fig. 3.8 The current densities J , J_{bb} , and J_{cb} of $\text{In}_{0.2}\text{Ga}_{0.8}\text{N}/\text{GaN}$ multi-QW LDs at threshold versus the number of QWs for $Q_v = 0.33$ and 0.45 . (p.54)

Fig. 3.9 The current densities of InGaN/GaN multi-QW LDs at threshold versus the number of QWs in Nagahama's paper. (p.54)

Fig. 3.10 The spectra of the gain g and the spontaneous emission rate r_{sp} at two different temperatures $T = 300$ and 400 K for 3.6 nm $\text{In}_{0.2}\text{Ga}_{0.8}\text{N}/\text{GaN}$ single-QW LDs at threshold with (a) $Q_v = 0.33$ and (b) $Q_v = 0.45$. (p.56)

Fig. 3.11 The current densities J , J_{bb} , and J_{cb} at threshold as functions of temperature T for the 3.6 nm $\text{In}_{0.2}\text{Ga}_{0.8}/\text{GaN}$ single-QW LDs with $Q_v = 0.33$ and 0.45 . (p.58)

Fig. 3.12 The spectra of the total spontaneous emission rate r_{sp} and one of its components, $r_{sp,cb}$, at threshold for 3.6 nm $\text{In}_{0.2}\text{Ga}_{0.8}\text{N}/\text{GaN}$ single-QW LDs with various doping levels for $Q_v = 0.33$ in panel (a) and $Q_v = 0.45$ in panel (b). The $N_{D,s}^+$ and $N_{A,s}^-$ are the sheet concentrations of ionized donors and acceptors, respectively. (p.60)

Fig. 3.13 Excitation power dependent PL spectra of InGaN/GaN QW LEDs at 5 K (a) for an undoped structure and (b) for the structure doped with Si at 10^{18} cm^{-3} . (p.61)

Fig. 3.14 Schematic diagrams of the conduction and the valence bands together with the

Fermi level F , and the quasi-Fermi levels F_c and F_v at threshold for the cases of n -type doping (the left) and p -type doping (the right). (p.63)

Fig. 3.15 The current densities, J , J_{bb} , and J_0 , at threshold versus the ionized dopant concentration for 3.6 nm $\text{In}_{0.2}\text{Ga}_{0.8}\text{N}/\text{GaN}$ single-QW LDs, assuming $Q_v = 0.33$ in panel (a) and $Q_v = 0.45$ in panel (b). The J is the total threshold current density, the J_{bb} is the current density due to the bound-to-bound process, and the J_0 is the threshold current density calculated without considering the carrier spillover. (p.65)

Fig. 3.16 The current density, J , at threshold as functions of the cavity loss for 3.6 nm $\text{In}_{0.2}\text{Ga}_{0.8}\text{N}/\text{GaN}$ single-QW LDs with various doping levels for $Q_v = 0.33$ in panel (a) and $Q_v = 0.45$ in panel (b). (p.67)

Fig. 3.17 The current density, J , at threshold versus temperature for 3.6 nm $\text{In}_{0.2}\text{Ga}_{0.8}\text{N}/\text{GaN}$ single-QW LDs with various doping levels for $Q_v = 0.33$ in panel (a) and $Q_v = 0.45$ in panel (b). (p.69)

Fig. 3.18 The current densities, J , J_{bb} , and J_0 , at threshold versus the ionized dopant concentration for 3.6 nm $\text{In}_{0.2}\text{Ga}_{0.8}\text{N}/60$ nm GaN double-QW LDs, assuming $Q_v = 0.33$ in panel (a) and $Q_v = 0.45$ in panel (b). (p.70)

CHAPTER 4

Fig. 4.1 Valence band profile of the three superlattices constructed with equal well width (2 nm) but different barrier widths (2, 4 and 6 nm) under the same current density 3.6 kA/cm^2 for (a) Ga-face and (b) N-face polarities. (p.76)

Fig. 4.2 The proportion of the tunneling current density $J_{\text{tunneling}}$ to the total current density flowing through each barrier under the same condition in Fig. 2 for (a) Ga-face and (b) N-face polarities. (p.78)

Fig. 4.3 Valence band profile of the three superlattices constructed with equal well width (2 nm) but different barrier widths (2, 4 and 6 nm) under the same current density 3.6 kA/cm^2 for (a) Ga-face and (b) N-face polarities at 400 K. (p.80)

Fig. 4.4 The proportion of the tunneling current density $J_{\text{tunneling}}$ to the total current density

flowing through each barrier under the same condition in Fig. 2 for (a) Ga-face and (b) N-face polarities at 400 K. (p.81)

Fig. 4.5 The average vertical resistivities of the three SLs having different barrier widths (2, 4, and 6 nm) at 300 K and 400K. (p.82)



Chapter 1

Introduction

1.1 Milestones of developing nitride-based optical devices

In recent years, there has been a lot of research effort in exploring blue-violet light sources, such as light-emitting diodes (LEDs) and laser diodes (LDs), due to their potential applications in full-color displays and high-density optical storage. Potential materials for the short-wavelength emission include SiC-, [1] ZnSe-, [2,3] and GaN-based wide-gap semiconductors. [4] Among them, the nitrides, such as GaN and the related ternary (AlGaInN and InGaInN) and quaternary (AlGaInN) compounds, are considered more promising for high-brightness emission, and currently they have been used commercially in making up blue-violet and green LEDs and LDs. [5-7] Except for the blue-violet light sources, the nitrides also have the potential to become the main material of light sources for the whole range of visible light, due to their large variation of band gaps from 0.78 eV to 6.2 eV. Fig. 1.1 shows the bandgap energy of GaN, AlN, InN, and their ternary compounds or possible quaternary compounds as a function of the lattice constants. [8]

Before 1986, the progress of preparing the nitrides was not smooth. There were two main challenges, including (1) no lattice-matched substrate for nitrides and (2) the high activation energy of *p*-type dopants in nitrides. Owing to much effort, the obstacles were overcome step by step and the techniques for preparing nitrides make progress in recent twenty years. It is worthwhile to review some important breakthroughs here.

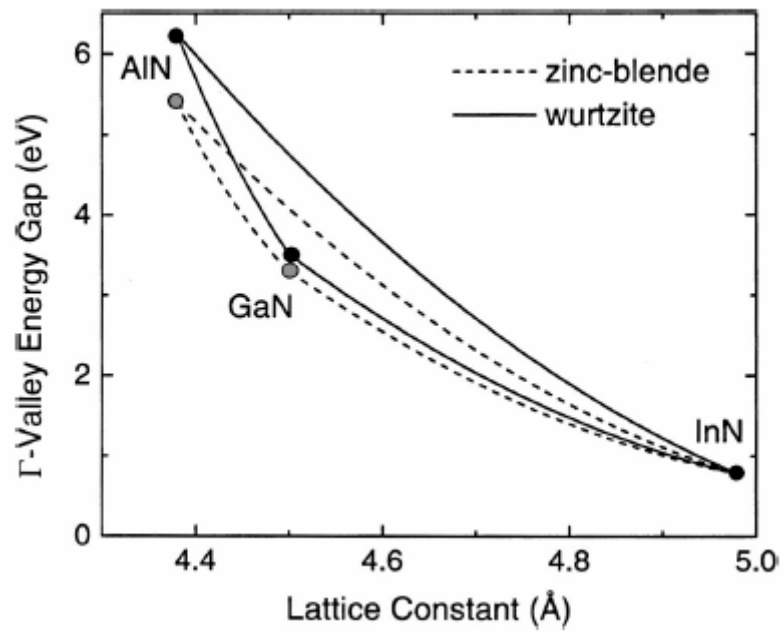


Fig. 1.1 Bandgap energy of GaN, AlN, InN, and their ternary compounds or possible quaternary compounds as a function of the lattice constants.[8]

1.1.1 Buffer layer

In order to reduce the stress resulting from the lattice mismatch between GaN films and the substrate, H. Amano et al. first used high-temperature (900 ~ 1000 °C) growth AlN as the buffer layer in 1986.[9] After two years, they used low-temperature (about 600 °C) growth AlN as the buffer layer and got good quality GaN films.[10] Then, S. Nakamura first chose low-temperature growth GaN as the buffer layer and got high quality GaN films in 1991.[11] Simultaneously, he developed a new reactor, which is so called two-flow MOCVD, to grow uniform GaN films. The schematic principle figure is shown in Fig. 1.2. There are two flows that bring gases into the reactor. The main one carries the reactant flowing parallel to the substrate fast while the subflow transports inactive gas perpendicular to the substrate. The purpose of the subflow is to change the direction of the main flow, making the reactant gas contact the substrate uniformly.



1.1.2 Epitaxially laterally overgrowth GaN (ELOG)

Although the high quality GaN films can be obtained by using low-temperature GaN buffer layer, the number of threading dislocation densities is still too large so that they were not good enough to be used in blue LDs. A. Usui et al. hence developed a so called “epitaxially laterally overgrowth GaN” (ELOG) method to get much more quality GaN films in 1997.[12] He etched a SiO₂ mask above the MOVPE-grown GaN layer and then overgrew GaN film, as shown in Fig. 1.3. The mask can stop the threading dislocation in the GaN buffer layer extending into the overgrown GaN film. In the same year, S. Nakamura used ELOG to obtain blue LDs. The lifetime can exceed 10,000 hours under continuous-wave operation. The cross section of the LD and the schematic diagram are shown in Fig. 1.4.[13]

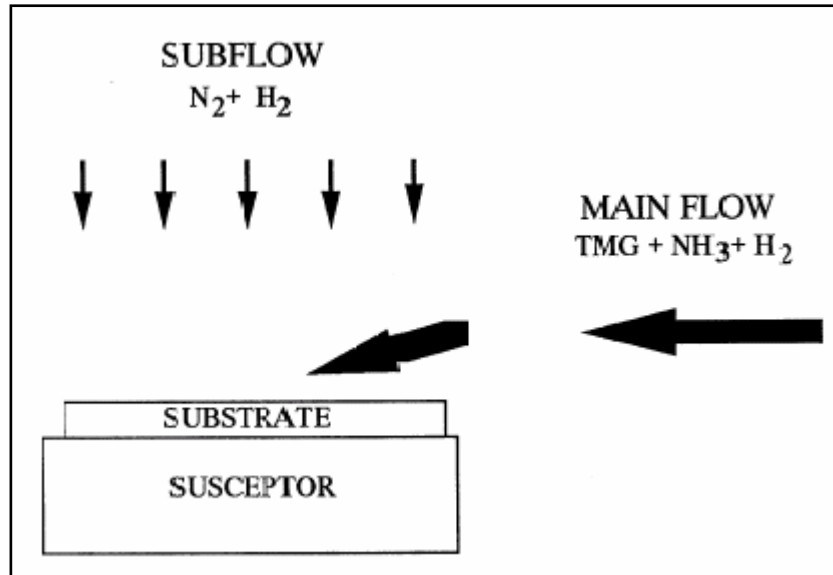


Fig. 1.2 Schematic principle figure of two-flow MOCVD.[11]

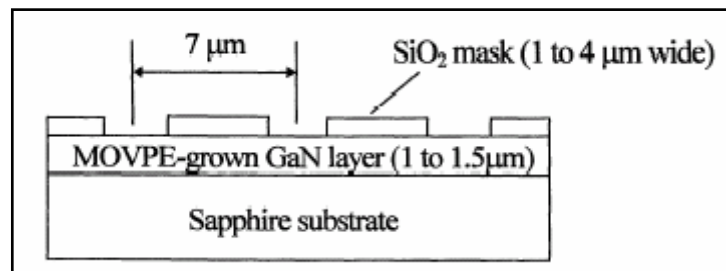
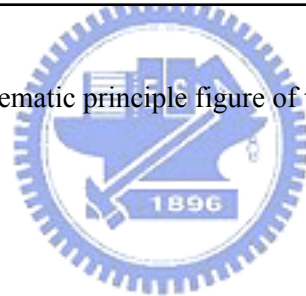


Fig. 1.3 Schematic diagram of the substrate for ELOG. in A. Usui's paper.[12]

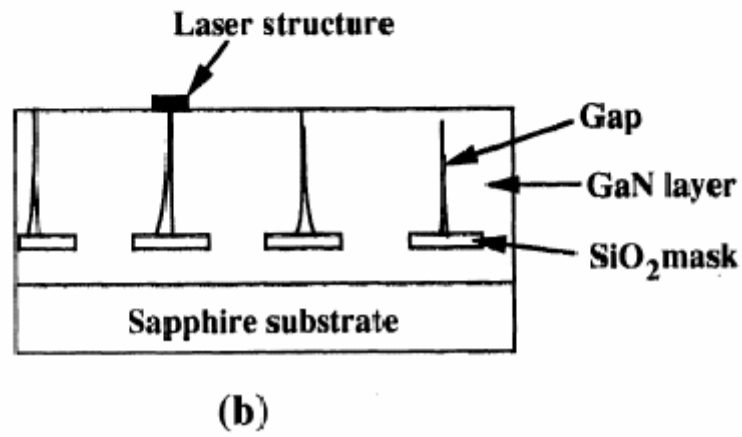
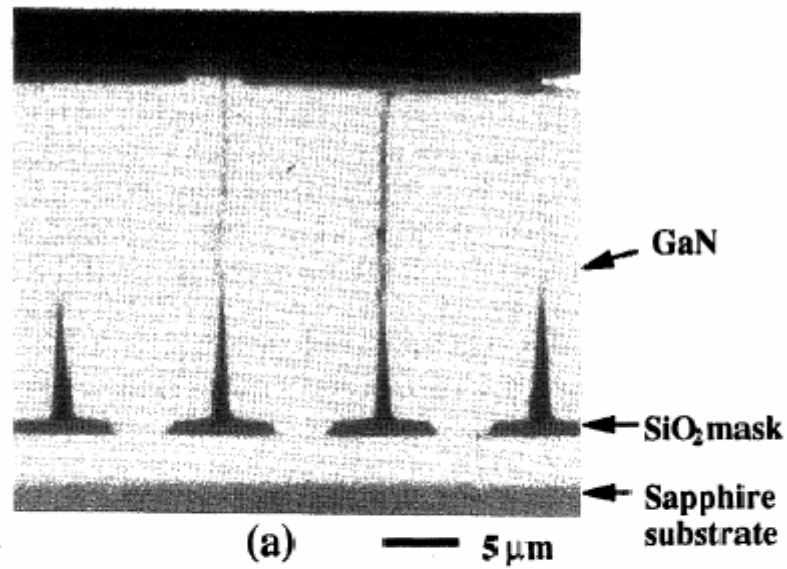


Fig. 1.4 (a) Cross section of the LD fabricated on ELOG substrate. (b) The schematic diagram of (a).[13]

The dislocation densities can be largely reduced in the region above the SiO₂ mask except the center. There are cracks between two neighboring GaN overgrown surface when they meet together.

1.1.3 The activation of Mg doped in GaN

So far, Mg is generally used as the *p*-type dopant in nitrides. But it is easily combined with hydrogen to be the complex Mg-H and can not substitute for Ga in GaN lattice. Hence, the resistivity of Mg-doped GaN is very high if the surrounding is H₂-ambient. In order to activate Mg, H. Amano treated Mg-doped GaN with low energy electron beam irradiation (LEEBI) and then got high hole concentration and low resistivity in 1989.[14] Three years later, S. Nakamura found that the mechanism low energy electron beam can activate Mg is just the heating caused by the impact. So he treated the samples simply with N₂-ambient thermal annealing and got low-resistivity *p*-type GaN, as shown in Fig. 1.5.[15] In Nakamura's experimental results, the resistivity becomes to decrease when the temperature goes beyond 400 °C and then reaches the lowest value at 700 °C.

1.1.4 Modulation-doped strained-layer AlGa_N/Ga_N superlattice

In nitride-based LD structure, the cladding layer is generally composed of AlGa_N. However, due to the large stress (the lattice mismatch between GaN and AlN is about 3.5%), the thickness of AlGa_N film can not exceed a critical value (~ 200 nm, depending on the Al composition), or it will have cracks. In order to prevent the formation of cracks, AlN/GaN strained-layer superlattices (SLSs) were grown by molecular beam epitaxy (MBE) in 1990.[16] Nakamura adopted this idea and used the AlGa_N/Ga_N SLSs as the cladding layer in intride-based LDs to prevent cracking during growth by MOCVD.[13]

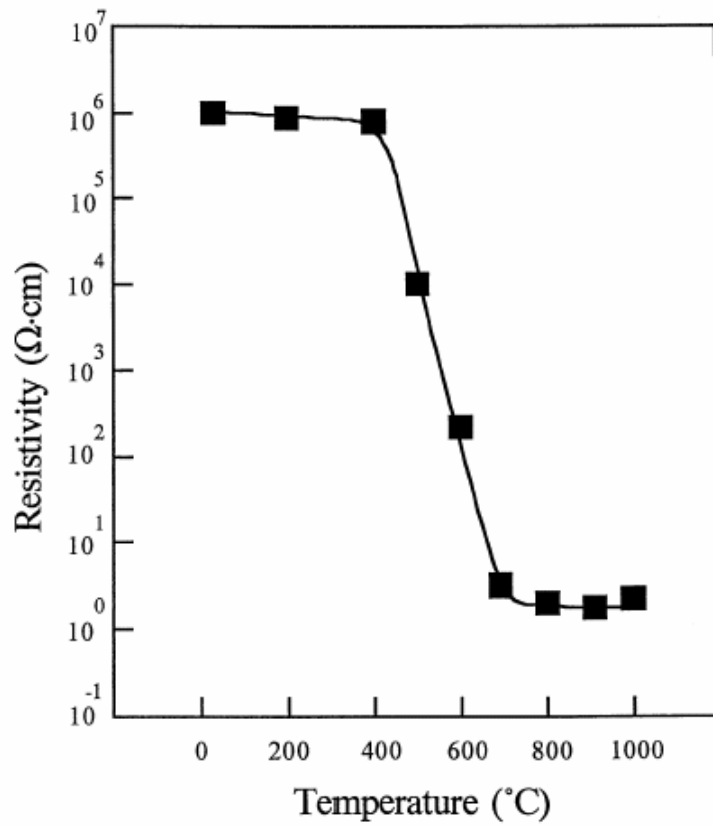
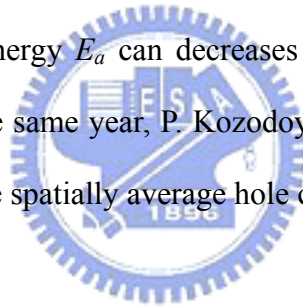


Fig. 1.5 Resistivity of Mg-doped GaN films as a function of thermal annealing temperature.[15]

Besides of improving the crystal quality of cladding layer, AlGa_N/Ga_N SLSs can also reduce the activation energy of the *p*-type dopant Mg and hence can increase the hole concentration in *p*-type cladding layer. This is because the acceptor levels in the barrier region are far below the Fermi level, as indicated by a schematic diagram in Fig 1.6, so that the electrons are easily accepted by the impurity levels, producing holes which will relax to the well region. Since the acceptor levels in the well region are not easily ionized, one can choose not to dope there. This method is so called “modulation-doping”. The decrement of impurities in well regions can also reduce the scattering of the holes moving through the superlattices and hence increases the hole mobility. I. D. Goepfert et al. used modulation-doping in AlGa_N/Ga_N superlattice and got the high concentration, as shown in Fig. 1.7.[17] The activation energy E_a can decrease from 200 meV (*p*-type Ga_N) to 58 meV (Al_{0.2}Ga_{0.8}N/Ga_N). At the same year, P. Kozodoy et al. discussed the influence of the period of the superlattice on the spatially average hole concentration.[18]



1.1.5 Development of group III nitride LEDs and LDs

Based on the key breakthroughs mentioned above, group III nitride LEDs and LDs were realized step by step. The key events are summarized in Table 1.1. Although the blue LDs under the continuous wave (c.w.) operation are already realized in 1996. There are some obstacles existing: for instance, the high threshold current density and operation voltage. Until now, many researchers still make efforts to investigate the physical mechanism in nitride-based LEDs and LDs and hope to improve their performance.

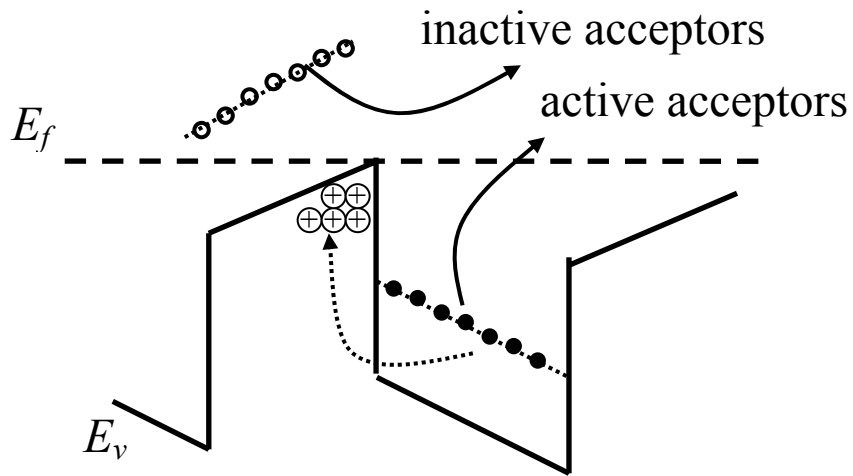


Fig. 1.6 Schematic valence band diagram of a AlGaN/GaN superlattice

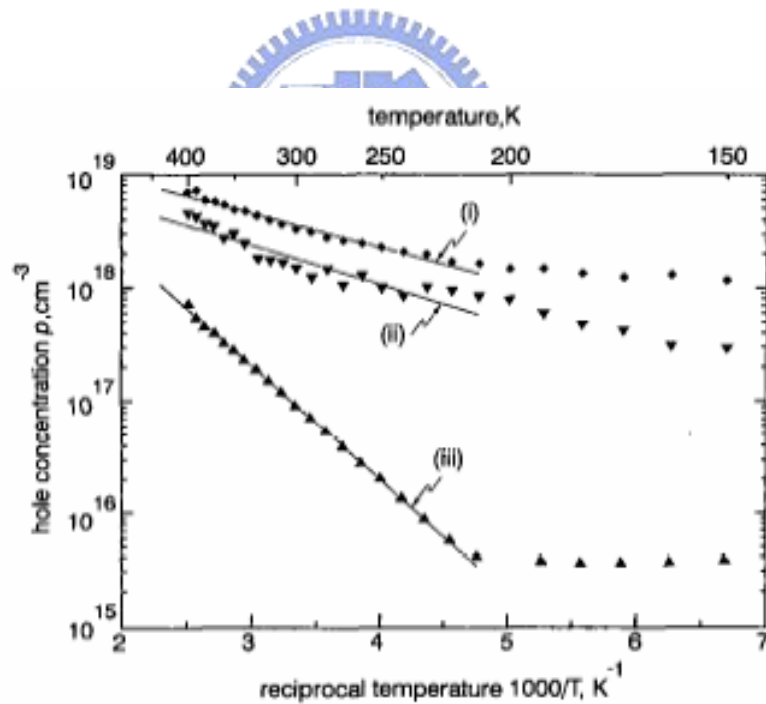


Fig. 1.7 Free hole concentration against reciprocal temperature for $\text{Al}_x\text{Ga}_{1-x}\text{N}/\text{GaN}$ doped superlattices with $x=10$ and 20% aluminium content as well as carrier concentration in p-type bulk GaN sample. (i) $E_a = 58$ meV ($\text{Al}_{0.2}\text{Ga}_{0.8}\text{N}/\text{GaN}$); (ii) $E_a = 70$ meV ($\text{Al}_{0.1}\text{Ga}_{0.9}\text{N}/\text{GaN}$); (iii) $E_a = 200$ meV (p-type GaN).[17]

Table 1.1 Key events of the development of nitride-based LED and LD

Year	Events	Author
1986	AlN buffer layer (MBE)	Amano[9]
1989	<i>p</i> -type doping with Mg treated by LEEBI GaN <i>p</i> -n junction LED	Amano[14]
1990	AlN/GaN SLSs by MBE	Sitar[16]
1991	GaN buffer layer by MOCVD	Nakamura[11]
1992	Mg activation by thermal annealing High-brightness AlGaIn ultraviolet/blue LED	Nakamura[15] Akasaki[19]
1994	InGaIn/AlGaIn DH blue LEDs (1cd)	Nakamura[20]
	InGaIn QW blue, green and yellow LEDs	Nakamura[21]
1995	InGaIn SQW green LEDs (10cd)	Nakamura[22]
	Blue laser diode under pulsed operation	Nakamura[5]
1996	Blue laser diode under c.w. operation	Nakamura[6]
1997	Epitaxially laterally overgrowth GaIn (ELOG)	Usui[12]
	The lifetime of blue laser diode exceeded 10,000 hours.	Nakamura[13]

1.1.6 Nitride-based LD structure

The structure generally used in nitride-based LD is shown in Fig. 1.8. The major parts include: (1) sapphire substrate; (2) GaN buffer layer; (3) SiO₂ mask for ELOG; (4) laterally overgrown GaN; (5) *n*- and *p*-type modulation-doped strained-layer superlattices (MDSLS) as cladding layers; (6) *n*- and *p*-type GaN as guiding layers; and (7) multiquantum well (MQW) as active region. It can be noticed that there is a *p*-type AlGaN sandwiched between the *p*-type guiding layer and the active region. This AlGaN layer is called electron blocking layer (EBL), which can prevent the electrons from leaking to *p*-type side since the electron overflow of the active region is very serious in nitride-based LD.

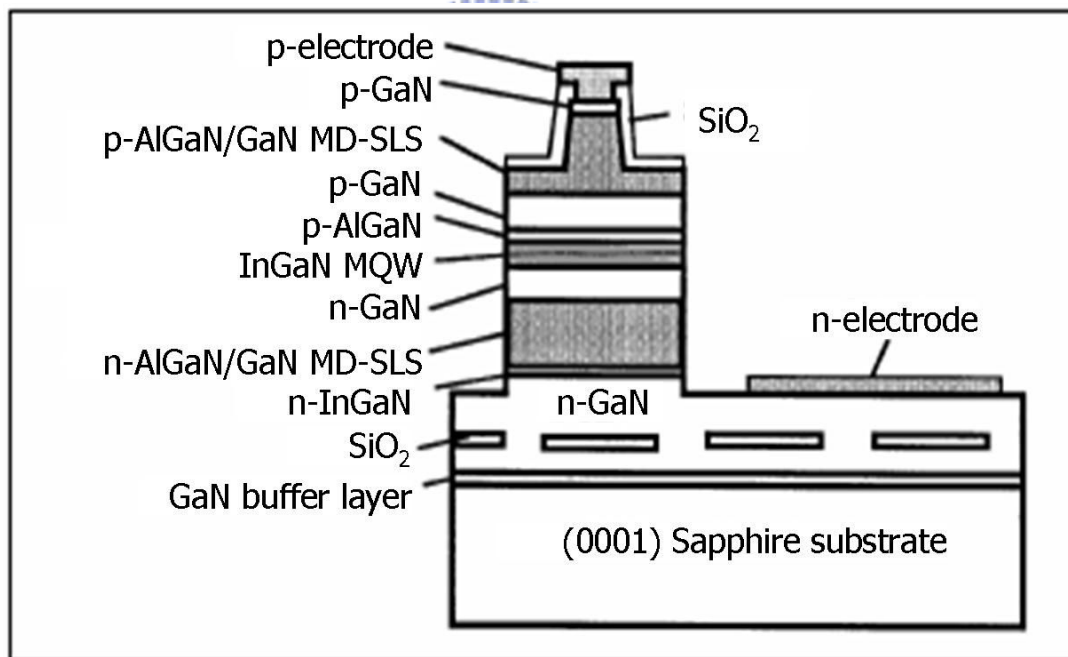


Fig. 1.8 The general structure of nitride-based laser diodes.

1.2 Motivation and background

The reliability of the wide-gap nitride LDs is still an important issue because of their short lifetime caused by high threshold current. In comparison with conventional zinc-blende GaAs-based lasers, the high threshold current of the wurtzite nitride lasers may be attributed to several factors, including immature material preparation, the intrinsic large density of states in the valence bands, and large leakage current in the device structures not yet optimized.

1.2.1 Spillover effects

The leakage current can be regarded as composed mainly of three components according to their different origins: (1) the component caused by nonradiative recombination of electrons and holes in the active region, (2) the one due to electron leakage from the active region to the *p*-type cladding layers,[23] and (3) the one caused by the interband transition of high-energy carriers in the neighborhood of the active region. [23] The leakage current due to nonradiative recombination has been considerably alleviated in the GaN lasers by the reduction of defects with the progress of material growth and device processing technologies.[24,25] As to the electron leakage into the *p*-type cladding layer, it has been commonly found from recent works that such leakage can be reduced significantly by the insertion of an AlGaN electron blocking layer (EBL) between the active region and the *p*-type layer.[26-30] Furthermore, it has been demonstrated that this leakage can be made very low compared to other leakages by optimization on the structure with EBL.[27-30] The hole leakage out of the active region can be neglected because of the large effective mass of the inertial holes.

The EBL, however, cannot suppress the spillover of energetic carriers into the

continuous subband states above the barriers in energy surrounding the quantum wells (QWs) of the active region. Interband transition involving the high-energy spillover carriers usually gives a negligibly small contribution to the optical peak gain of the QW active region, but may cause significant consumption of electric current. Therefore, the recombination of spillover carriers can be regarded as one of the paths for the leakage current. Such a problem of carrier spillover depends on temperature and is particularly serious for electrons in the conduction bands because of the small electron effective mass, the large asymmetry between the densities of states of the conduction and valence bands, and the narrow QWs usually used in the nitride LDs. There are quite few literatures discussing leakage due to the recombination of spillover carriers,[23] and so far, the influences of the optical transitions from the spillover carriers on the shapes of gain and spontaneous emission spectra have not been discussed and analyzed in detail. Furthermore, there has not been any research work on this problem for the short-wavelength nitride LDs.

In this dissertation, we present the calculation results of the carrier spillover effects on the optical gain, the spontaneous emission, and the threshold current for InGaN/GaN QW LDs. The influences of the temperature are also discussed. We found that the electron spillover can broaden the gain and the spontaneous emission spectra, deteriorating the threshold of QW LDs. An optimized multi-QW structure is then proposed to solve the problem.

1.2.2 Modulation *p*-type doping in the active region

In addition to the optimization on the structure of the active region, more efforts can be made for further reducing the threshold current. For example, one can introduce dopants into the active region. Actually, *n*-type doping with Si in the InGaN/GaN quantum wells (QWs) has been performed in some experimental works.[31-34] It is found that the Si

doping can improve the crystalline quality of GaN layers and the InGaN/GaN interface.[35,36] It is well known that the optimized temperature for the high crystalline quality of InGaN wells is lower than that suitable for the growth of GaN barriers. In order to get high quality of InGaN wells, the GaN layers are generally compelled to be grown at low temperature. Hence, this forms the island-like spiral defects initiated by threading dislocations existing in the underlying GaN template. Fortunately, workers found that introducing Si impurities can dramatically suppress these island-like spiral structures of GaN layers.

However, the *n*-type doping causes a large amount of electrons occupying high energy states at threshold and leads to serious spillover of electrons. A high barrier of EBL is then needed to prevent the energetic electrons from leaking into the *p*-type cladding layer, but this gives rise to a reduction in optical confinement within the active region. From this point of view, the *p*-type doping should be a better choice than the *n*-type doping because it can reduce the number of spillover electrons at threshold. However, there are few experimental or theoretical works concerning the optical property of the *p*-type doped active region in InGaN/GaN QW LDs. In order to further improve the performance of the InGaN/GaN QW LDs, it is worthwhile to investigate the influence of *p*-type doping on the optical property of the active region.

So, we also theoretically investigate the influence of different species (the *n*-type and *p*-type) and various levels of doping to the active region on the spontaneous emission rate and the threshold current density of InGaN/GaN LDs. Our results demonstrate that the amount of spillover electrons at threshold can indeed strongly depend on the species and the level of doping. Accordingly, we can obtain a low threshold current by optimizing the doping level with a preferred doping species.

1.2.3 Vertical resistivity of *p*-type AlGaN/GaN superlattices

Besides the high threshold current, some difficulties obstructing further advancement still exist. For example, the *p*-type AlGaN cladding layers for LDs or LEDs have in general a high electric resistivity due to the high activation energy of acceptors doped in GaN and related nitride alloys.[37-41] To reduce the resistivity, one can insert an $\text{Al}_x\text{Ga}_{1-x}\text{N}/\text{GaN}$ superlattice (SL) into the cladding layer.[42-46] In the inserted SLs, the holes are easily ionized from the acceptors in the barriers to the wells since the acceptor levels in the barrier region are far below the Fermi level. Therefore, the spatially averaged density of holes can be much increased by inserting a SL in the cladding layer.[47]

However, the average vertical resistivity across the *p*-type $\text{Al}_x\text{Ga}_{1-x}\text{N}/\text{GaN}$ SL is still large because of the high barriers of the SL. Linearly graded barriers ($\text{Al}_x\text{Ga}_{1-x}\text{N}$) with appropriate doping have been used to reduce the barrier height and hence obtain a low vertical electric resistance.[48,49] However, decreasing the barrier height may also cause a reduction of optical confinement by the cladding layers for light-emitting devices. Furthermore, it is inconvenient to fabricate the graded layers with continuously varying composition.

In this dissertation, we also investigate theoretically the electrical properties of *p*-type SL structures without using the graded layers and find out the key factor that influences the vertical resistance dominantly. Accordingly, we propose a more preferred SL structure than the previous ones.

Chapter 2

Calculation Method

2.1 Piezoelectric and spontaneous polarization

The nature structure of the III-V nitrides is wurtzite, a hexagonal Bravais lattice with a basis of 2 diatomic molecules (for instance, GaN). The wurtzite structure is a noncentrosymmetric compound crystal exhibiting two different sequences of atomic layers laying in two opposite directions parallel to the crystallographic c -axis, and consequently crystallographic polarity along the c -axis can be observed. In wurtzite structure, the [0001] (also defined as the z axis here) is conventionally defined as the direction pointing from the cation to the nearest anion along the c -axis. The polarization mentioned above is so called spontaneous polarization \mathbf{P}_{sp} . The orientation of the spontaneous polarization is defined assuming that the positive direction goes along [0001], which depends on the sequence of the atomic layers. We take GaN as an example. For binary GaN compounds with wurtzite structure, the sequence of the atomic layers of the constituents Ga is along the [0001] direction, which is reversed to that of N along [000 $\bar{1}$], as shown in Fig. 2.1. The corresponding (0001) and (000 $\bar{1}$) faces are respectively the Ga-face and N-face, as indicated in the figure. So, we can define $\mathbf{P}_{\text{sp}} = P_{\text{sp}}\hat{z}$ for Ga-face GaN and $\mathbf{P}_{\text{sp}} = -P_{\text{sp}}\hat{z}$ for N-face GaN. The GaN films grown by MOCVD are generally Ga-face while they are commonly N-face by MBE.

Since the lattice mismatch is an inherent problem in preparing nitrides, the nitride films are generally stressed. The components of the piezoelectric tensor are not all vanished in

wurtzite structure under stress. So, we have piezoelectric polarization as well, and taking GaN as the example, it is expressed as[50]

$$\mathbf{P}_{\text{pz}} = \begin{cases} 2d_{31}(C_{11} + C_{12} - \frac{2C_{13}^2}{C_{33}})\varepsilon_{\parallel}\hat{z} & \text{for Ga-face,} \\ -2d_{31}(C_{11} + C_{12} - \frac{2C_{13}^2}{C_{33}})\varepsilon_{\parallel}\hat{z} & \text{for N-face,} \end{cases} \quad (1.1)$$

where d_{31} is the piezoelectric constant, C_{ij} are the elastic stiffness constants, and ε_{\parallel} is the in-plane component of the strain tensor. Since $d_{31}(C_{11} + C_{12} - 2C_{13}^2 / C_{33}) < 0$ for AlGaIn and InGaIn over the whole range of compositions, the orientation of the piezoelectric polarization is parallel to the spontaneous polarization in the case of tensile strained layers, but anti-parallel in compressive strained ones.

If we consider a epitaxial films grown on the top of a thick relaxed GaN buffer layer, the discontinuity of the polarization ($\mathbf{P}_{\text{sp}} + \mathbf{P}_{\text{pz}}$) induces sheet charge density at the interface, as indicated by σ in Fig. 2.2, and free carriers will be attracted and accumulate[51].

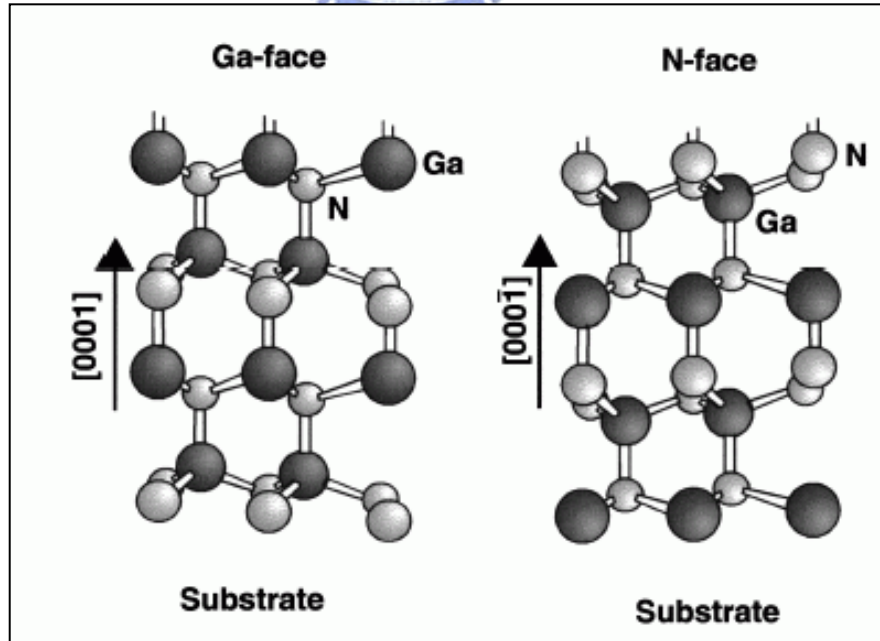


Fig. 2.1 Schematic drawing of the crystal structure of wurtzite Ga-face and N-face GaN

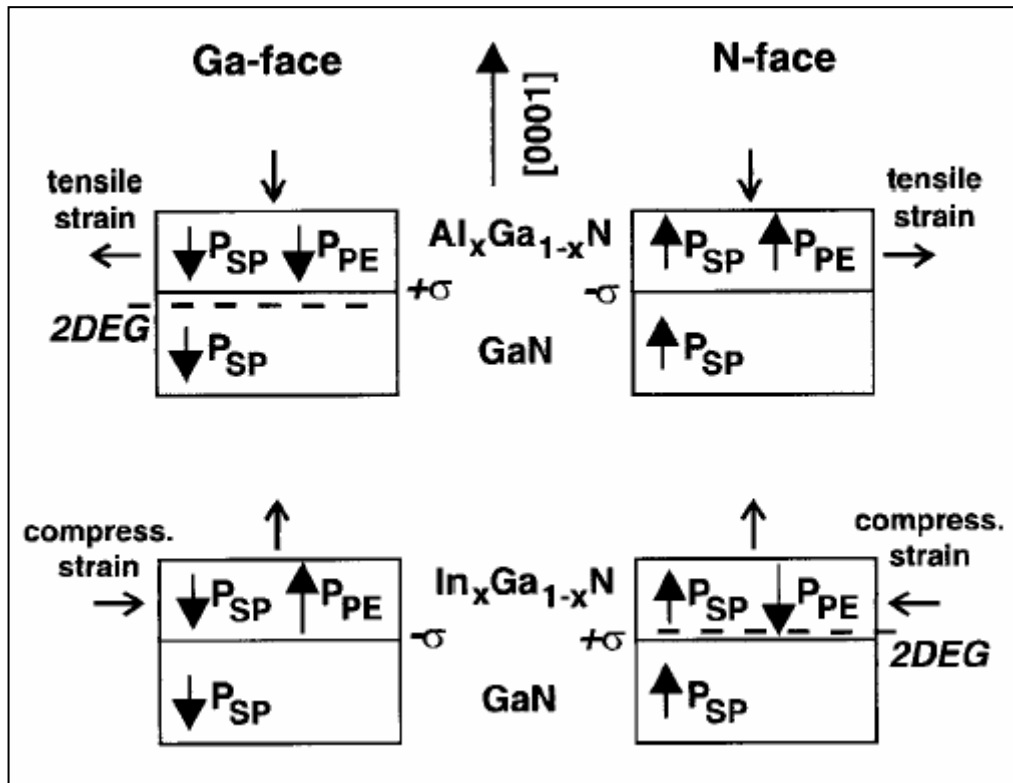


Fig. 2.2 Orientation of the spontaneous and piezoelectric polarization in pseudomorphic grown wurtzite AlGaIn/GaN and InGaIn/GaN heterostructures with Ga- or N-face polarity.[51]

2.2 Band structure of quantized heterojunction

2.2.1 Luttinger-Kohn Hamiltonian for holes

In this section, we derive the Luttinger-Kohn Hamiltonian for holes in the wurtzite structure. The $\mathbf{k} \cdot \mathbf{p}$ method introduced by Bardeen and Seitz is used here.[52,53] Consider the Hamiltonian near the zone center with the spin-orbit interaction,

$$H = H_0 + \frac{\hbar}{4m_0^2c^2} \boldsymbol{\sigma} \cdot \nabla V \times \mathbf{p},$$

$$H_0 = \frac{p^2}{2m_0} + V(\mathbf{r}),$$
(2.1)

where \hbar is the reduced Plank constant, m_0 is the free electron mass, c is the speed of light in free space, \mathbf{p} is the momentum, and $\boldsymbol{\sigma}$ is the Pauli spin matrix. Using the Bloch theorem, the original Schrodinger equation for an electron wave function $\psi_{n\mathbf{k}}(\mathbf{r})$ in the n th band with a wave vector \mathbf{k} will be

$$\left\{ \frac{p^2}{2m_0} + V(\mathbf{r}) + \frac{\hbar}{4m_0^2c^2} [\nabla V \times \mathbf{p}] \cdot \boldsymbol{\sigma} \right\} \psi_{n\mathbf{k}}(\mathbf{r}) = E_n(\mathbf{k}) \psi_{n\mathbf{k}}(\mathbf{r})$$
(2.2)

where

$$\psi_{n\mathbf{k}}(\mathbf{r}) = e^{i\mathbf{k} \cdot \mathbf{r}} u_{n\mathbf{k}}(\mathbf{r}).$$
(2.3)

Here, $u_{n\mathbf{k}}(\mathbf{r})$ is the cell periodic function. Further, we can obtain the Schrodinger equation for $u_{n\mathbf{k}}(\mathbf{r})$:

$$\left[H_0 + \frac{\hbar^2 k^2}{2m_0} + \frac{\hbar}{m_0} \mathbf{k} \cdot \mathbf{p} + \frac{\hbar}{4m_0^2c^2} \nabla V \times \mathbf{p} \cdot \boldsymbol{\sigma} + \frac{\hbar^2}{4m_0^2c^2} \mathbf{k} \cdot \boldsymbol{\sigma} \times \nabla V \right] u_{n\mathbf{k}}(\mathbf{r})$$

$$= E_n(\mathbf{k}) u_{n\mathbf{k}}(\mathbf{r}).$$
(2.4)

Note that the last term on the left-hand side is the \mathbf{k} -dependent spin-orbit interaction. Since the electron velocity in the atomic orbit is much larger than the velocity of the wave packet with the wave vectors near the zone center, the last term is much smaller than the other terms and can be neglected.

For the wide band-gap semiconductors, the coupling of valence bands to the two degenerate conduction bands can be ignored. So we can treat the six valence bands in class A , which we are interested in, and put the other bands in class B . The upper valence bands of bulk wurtzite semiconductors at the zone center ($\mathbf{k} = 0$) are described mostly by p -like functions:

$$\begin{aligned} u_1 &= \left| -\frac{(X+iY)}{\sqrt{2}} \uparrow \right\rangle, u_2 = \left| \frac{(X-iY)}{\sqrt{2}} \uparrow \right\rangle, u_3 = |Z \uparrow\rangle; \\ u_4 &= \left| \frac{(X-iY)}{\sqrt{2}} \downarrow \right\rangle, u_5 = \left| -\frac{(X+iY)}{\sqrt{2}} \downarrow \right\rangle, u_6 = |Z \downarrow\rangle. \end{aligned} \quad (2.5)$$

We choose these six valence-band wave functions as the bases for the states of interest (class A) and write the band-edge wave function as

$$u_{n\mathbf{k}}(\mathbf{r}) = \sum_{j'}^A a_{j'}(\mathbf{k}) u_{j'0}(\mathbf{r}) + \sum_{\gamma}^B a_{\gamma}(\mathbf{k}) u_{\gamma 0}(\mathbf{r}). \quad (2.6)$$

Use Loowdin's method. The six-by-six Hamiltonian matrix for the valence bands can be written as

$$H_{jj'}^{6 \times 6}(\hat{k}) = H_{jj'}^{6 \times 6}(k=0) + D_{jj'}^{6 \times 6}(\hat{k}), \quad (2.7)$$

where the operation version is used. The first term on the right-hand side is corresponds to the Hamiltonian obtained from Kane's model at $\mathbf{k} = 0$. [54] Use the six wave functions in Eq. (2.5) as the bases, the Kane Hamiltonian takes the form

$$H_{Kane}^{6 \times 6} = \begin{bmatrix} \Delta_1 + \Delta_2 + E_v & 0 & 0 & 0 & 0 & 0 \\ 0 & \Delta_1 - \Delta_2 + E_v & 0 & 0 & 0 & \sqrt{2}\Delta_3 \\ 0 & 0 & E_v & 0 & \sqrt{2}\Delta_3 & 0 \\ 0 & 0 & 0 & \Delta_1 + \Delta_2 + E_v & 0 & 0 \\ 0 & 0 & \sqrt{2}\Delta_3 & 0 & \Delta_1 - \Delta_2 + E_v & 0 \\ 0 & \sqrt{2}\Delta_3 & 0 & 0 & 0 & E_v \end{bmatrix}. \quad (2.8)$$

The parameters Δ_i ($i=1, 2, 3$) account for either the crystal-field split energy (Δ_1) or the spin-orbit interactions (Δ_2 and Δ_3). E_v is the reference energy. The second term comes from the Loowdin's perturbation theory. But here, the Burt's exact envelope-function theory (EEFT) is considered to make the envelop function behave smoothly and continuously even

at abrupt interfaces.[55] Using the notation of Stavrinou and van Dalen,[56] the k -dependent second term is given by

$$D_{jj'}^{6 \times 6}(\hat{k}) = \sum_{\alpha, \beta} \hat{k}_\alpha \frac{\hbar^2}{2m_0} \hat{k}_\beta \delta_\alpha \delta_\beta + \frac{\hbar^2}{m_0^2} \sum_{\alpha, \beta=x,y,z} \hat{k}_\alpha \left(\sum_v \frac{\langle j | \hat{p}_\alpha | v \rangle \langle v | \hat{p}_\beta | j' \rangle}{E - E_v} \right) \hat{k}_\beta. \quad (2.9)$$

Note that the \hat{k}_α operators must have the specific ordering indicated here. Use the six wave functions in Eq. (2.5) as the bases, the $D^{6 \times 6}$ matrix takes the form,[57]

$$D^{6 \times 6} = \begin{bmatrix} D_{11} & D_{12} & D_{13} & & & \\ D_{12}^\dagger & D_{22} & D_{23} & & & 0 \\ D_{13}^\dagger & D_{23}^\dagger & D_{33} & & & \\ & & & D_{22} & D_{12}^\dagger & D_{23} \\ & 0 & & D_{12} & D_{11} & D_{13} \\ & & & D_{23}^\dagger & D_{13}^\dagger & D_{33} \end{bmatrix} \quad (2.10)$$

where

$$\begin{aligned} D_{11} &= \hat{k}_x(1-3\sigma-6\delta)\hat{k}_x + \hat{k}_y(1-3\sigma-6\delta)\hat{k}_y + \hat{k}_z(1-6\pi)\hat{k}_z \\ &\quad + i\hat{k}_x(6\delta-3\sigma)\hat{k}_y - i\hat{k}_y(6\delta-3\sigma)\hat{k}_x, \\ D_{12} &= \hat{k}_x(3\sigma)\hat{k}_x - \hat{k}_y(3\sigma)\hat{k}_y - i\hat{k}_x(3\sigma)\hat{k}_y - i\hat{k}_y(3\sigma)\hat{k}_x, \\ D_{13} &= \frac{1}{\sqrt{2}}[\hat{k}_x(6\sigma_{xz})\hat{k}_z + \hat{k}_z(6\pi)\hat{k}_x - i\hat{k}_y(6\sigma_{xz})\hat{k}_z - i\hat{k}_z(6\pi)\hat{k}_y], \\ D_{33} &= \hat{k}_x(1-6\pi_z)\hat{k}_x + \hat{k}_y(1-6\pi_z)\hat{k}_y + \hat{k}_z(1-6\sigma_z)\hat{k}_z, \\ D_{22} &= D_{11}^*, \text{ and } D_{23} = -D_{13}^*. \end{aligned} \quad (2.11)$$

The six real dimensionless parameters σ , σ_z , σ_{xz} , δ , π , and π_z correspond to the nonvanishing inner products of the perturbation.[57] The full Hamiltonian $H^{6 \times 6}(\hat{k})$ is obtained by adding Eq. (2.8) and (2.10). After replacing the operators in $H^{6 \times 6}(\hat{k})$ with their corresponding wave numbers, we can relate the parameters σ , σ_z , σ_{xz} , δ , π , and π_z to the Rashba-Sheka-Pikus (RSP) parameters A_j 's and get

$$\begin{aligned}
A_1 &= 1 - 6\sigma_z, \\
A_2 &= 1 - 6\pi_z, \\
A_3 &= -6(\pi - \sigma_z), \\
A_4 &= -3\sigma - 6(\delta - \pi_z), \\
A_5 &= -3\sigma, \\
A_6 &= -\frac{6}{\sqrt{2}}(\pi + \sigma_{xz}).
\end{aligned} \tag{2.12}$$

2.2.2 Hamiltonian applicable to strained QW along [0001]

We consider a typical III-V nitride QW structure grown along the [0001] direction (also defined as z axis here). In such a case, the potential of hole is only confined along the z axis, and since the structure is perfectly bulklike along the xy plane of the QW structure, \hat{k}_x and \hat{k}_y can be replaced by their wave numbers. Using the essential results from Pikus-Bir Hamiltonian for a strained semiconductor, the strain effects can be easily included by the same symmetry consideration and a straightforward addition of corresponding terms: $k_\alpha k_\beta \rightarrow \varepsilon_{\alpha\beta}$. [58,59] By means of the usual unitary transformation of basis functions with the unitary matrix

$$U = \begin{bmatrix} \alpha^* & 0 & 0 & \alpha & 0 & 0 \\ 0 & \beta & 0 & 0 & \beta^* & 0 \\ 0 & 0 & \beta^* & 0 & 0 & \beta \\ \alpha^* & 0 & 0 & -\alpha & 0 & 0 \\ 0 & \beta & 0 & 0 & -\beta^* & 0 \\ 0 & 0 & -\beta^* & 0 & 0 & \beta \end{bmatrix}, \tag{2.13}$$

where $\alpha = (1/\sqrt{2})e^{i(3\theta/2+3\pi/4)}$, and $\beta = (1/\sqrt{2})e^{i(\theta/2+\pi/4)}$ with $\theta = \tan^{-1}(k_y/k_x)$, the 6×6

Hamiltonian can be block diagonalized into one consisting of two 3×3 blocks, [57]

$$\hat{H}(\hat{k}_z; k_t) = \begin{bmatrix} \hat{H}^+(\hat{k}_z; k_t) & 0 \\ 0 & \hat{H}^-(\hat{k}_z; k_t) \end{bmatrix}, \tag{2.14}$$

with

$$\hat{H}^{\pm} = \begin{bmatrix} \hat{F} & K_t & \mp i\hat{H}_t \\ K_t & \hat{G} & \Delta \mp i\hat{H}_t \\ \mp i\hat{H}_t^{\dagger} & \Delta \mp i\hat{H}_t^{\dagger} & \hat{\lambda} \end{bmatrix}, \quad (2.15)$$

$$\begin{aligned} \hat{F} &= \Delta_1 + \Delta_2 + \hat{\lambda} + \hat{\theta}, \\ \hat{G} &= \Delta_1 - \Delta_2 + \hat{\lambda} + \hat{\theta}, \\ \hat{\lambda} &= \frac{\hbar^2}{2m_0} (\hat{k}_z A_1 \hat{k}_z + A_2 k_t^2) + D_1 \varepsilon_{\perp} + 2D_2 \varepsilon_{\parallel}, \\ \hat{\theta} &= \frac{\hbar^2}{2m_0} (\hat{k}_z A_3 \hat{k}_z + A_4 k_t^2) + D_3 \varepsilon_{\perp} + 2D_4 \varepsilon_{\parallel}, \\ K_t &= \frac{\hbar^2}{2m_0} A_5 k_t^2, \\ \hat{H}_t &= \frac{\hbar^2}{2m_0} \frac{k_t}{\sqrt{2}} [\hat{k}_z (1 + \sqrt{2} A_6 - A_1 - A_3) - (1 - A_1 - A_3) \hat{k}_z], \\ \Delta &= \sqrt{2} \Delta_3, \text{ and } \hat{k}_z = -i\partial / \partial z, \end{aligned} \quad (2.16)$$

where $k_t = \sqrt{k_x^2 + k_y^2}$ is the magnitude of the in-plane wave vector, and the D_i ($i=1-4$) are deformation potential constants. The normal strain components ε_{\perp} and ε_{\parallel} in the QW region are given by

$$\varepsilon_{\parallel} = \frac{a_0 - a}{a} \text{ and } \varepsilon_{\perp} = -\frac{2C_{13}}{C_{33}} \varepsilon_{\parallel}, \quad (2.17)$$

where a_0 and a are the lattice constants of undeformed materials making up the substrate and the QWs, respectively. C_{13} and C_{33} are stiffness constants of the QW material.

2.2.3 Wave function of valence states

Based on the $\mathbf{k} \cdot \mathbf{p}$ model, the wave functions of valence band states can be expressed as

$$\Psi^{\pm}(\mathbf{r}; \mathbf{k}_t) = \frac{1}{\sqrt{A}} e^{i\mathbf{k}_t \cdot \mathbf{r}_t} \sum_{\mu=1}^3 \psi_{\mu}^{\pm}(z; k_t) u_{\mu}^{\pm}, \quad (2.18)$$

which, together with their energy E , can be solved by the effective-mass equation,

$$\sum_{\nu=1}^3 [\hat{H}_{\mu\nu}^{\pm}(\hat{k}_z; k_t) + E_{\nu}^0(z)\delta_{\mu\nu}] \psi_{\nu}^{\pm} = E \psi_{\mu}^{\pm}, \quad \mu = 1, 2, 3, \quad (2.19)$$

where the ψ_{μ}^{\pm} are envelope functions and the u_{μ}^{\pm} are the transformed basis functions according to which the Hamiltonians $\hat{H}_{\mu\nu}^{\pm}$ are built up; [54,57] A is the area of the QWs; \mathbf{r}_t and \mathbf{k}_t are the in-plane position vector and the wave vector of the particle, respectively; $E_{\nu}^0(z)$ is the z -dependent valence band edge of the undeformed materials composing the heterostructure. Again, it is noticed that the order of the operators in Eq. (2.16) is of importance to the correct boundary conditions for matching the envelope functions. [57]

2.2.4 Conduction states and wave functions

For the conduction band states confined in the QW structure along the [0001] direction, we use the single-band effective-mass equation,

$$\begin{aligned} \left[-\frac{d}{dz} \frac{\hbar^2}{2m_z(z)} \frac{d}{dz} + V_{\text{eff}}(z) \right] \varphi = E \varphi, \\ V_{\text{eff}}(z) = \frac{\hbar^2 k_t^2}{2m_t(z)} + E_c^0(z) + P_{c\varepsilon}(z), \end{aligned} \quad (2.20)$$

to solve the envelope function φ and the energy E , where m_z (m_t) is the electron effective mass in the direction along (transverse to) the growth direction; $E_c^0(z)$ is the z -dependent conduction band edge of the undeformed materials composing the heterostructure; $P_{c\varepsilon}$ is the hydrostatic energy shift in the conduction band. Neglecting the small spin-splitting effect, we can write down the wave functions of conduction band states for spin up and spin down as simply a product of the envelope part and the Bloch function part,

$$\Phi^{\pm}(\mathbf{r}; \mathbf{k}_t) = \frac{1}{\sqrt{A}} e^{i\mathbf{k}_t \cdot \mathbf{r}_t} \varphi(z; k_t) u_c^{\pm}, \quad (2.21)$$

where u_c^{\pm} are the conduction band Bloch functions at the Γ point for spin up (+) and spin

down (-).

2.2.5 Carrier concentration

Once the wave functions are explicit, one can obtain the carrier concentrations along the z axis

$$\begin{aligned} n(z) &= \frac{2}{L_w} \sum_i \int |\varphi_i(z; k_t)|^2 f_i^c(F_c, k_t) \frac{k_t}{2\pi} dk_t \\ p(z) &= \frac{1}{L_w} \sum_{\sigma=\pm} \sum_j \int \sum_{\mu=1}^3 |\psi_{\mu j}^\sigma(z; k_t)|^2 [1 - f_j^\sigma(F_v, k_t)] \frac{k_t}{2\pi} dk_t, \end{aligned} \quad (2.22)$$

where the factor 2 in Eq. (2.22) accounts for the spin degeneracy in the conduction band.

L_w is the quantum well width. The functions $f_i^c(F_c, k_t)$ and $f_j^\sigma(F_v, k_t)$ are the

Fermi-Dirac distribution functions for the probabilities of electrons occupying the states

$$\begin{aligned} \Phi_i^\pm(\mathbf{r}; \mathbf{k}_t) &= \frac{1}{\sqrt{A}} e^{i\mathbf{k}_t \cdot \mathbf{r}_i} \varphi_i(z; k_t) u_c^\pm \quad \text{of conduction subband } i \quad \text{and the state} \\ \Psi_j^\sigma(\mathbf{r}; \mathbf{k}_t) &= \frac{1}{\sqrt{A}} e^{i\mathbf{k}_t \cdot \mathbf{r}_i} \sum_{\mu=1}^3 \psi_{\mu j}^\sigma(z; k_t) u_\mu^\sigma \quad \text{of valence subband } j, \quad \text{respectively.} \end{aligned}$$

The sheet carrier concentrations are useful in this dissertation and are shown here as well. For given quasi-Fermi levels of the conduction bands F_c and the valence bands F_v , one can obtain the sheet carrier concentrations as functions of quasi-Fermi levels by the integrals

$$\begin{aligned} n_s &= \frac{2}{L_w} \sum_i \int P_i^c(k_t) f_i^c(F_c, k_t) \frac{k_t}{2\pi} dk_t \\ p_s &= \frac{1}{L_w} \sum_{\sigma=\pm} \sum_j \int P_j^\sigma(k_t) [1 - f_j^\sigma(F_v, k_t)] \frac{k_t}{2\pi} dk_t, \end{aligned} \quad (2.23)$$

$P_i^c(k_t)$ and $P_j^\sigma(k_t)$ are the probabilities of finding the carriers at states $\Phi_i^\pm(\mathbf{r}; \mathbf{k}_t)$ and

$\Psi_j^\sigma(\mathbf{r}; \mathbf{k}_t)$, respectively, in the QW with width L_w and can thus be expressed by

$$\begin{aligned}
P_i^c(k_t) &= \int_{L_w} |\varphi_i(z; k_t)|^2 dz, \\
P_j^\sigma(k_t) &= \sum_{\mu=1}^3 \int_{L_w} |\psi_{\mu j}^\sigma(z; k_t)|^2 dz.
\end{aligned} \tag{2.24}$$

When we consider the charge concentration in the active region, the charge neutrality allows us to write

$$p_s + N_{D,s}^+ = n_s + N_{A,s}^-, \tag{2.25}$$

where p_s , n_s , $N_{D,s}^+$, and $N_{A,s}^-$ are the sheet concentrations of holes, electrons, ionized donors, and ionized acceptors, respectively. Here we use the sheet concentrations instead of the volume concentrations to avoid the complexity arising from the penetration of the bound wave functions into the barriers. The dopants are assumed to be introduced into the barriers around the QW. For convenience, we also assume the carriers released from the dopants are all relaxed to the well region.



2.3 Calculation method for optical properties

2.3.1 Optical gain and spontaneous emission rate

Consider the electron-photon interaction. The Hamiltonian can be expressed as

$$H = \frac{1}{2m_0} (\mathbf{p} - q\mathbf{A})^2 + V(\mathbf{r}), \tag{2.26}$$

where \mathbf{A} is the vector potential of the electromagnetic field. Expanding the square term, neglecting the $q^2\mathbf{A}^2/2m_0$ because of $|e\mathbf{A} \ll \mathbf{p}|$, and using the Coulomb gauge $\nabla \cdot \mathbf{A} = 0$ which makes $\mathbf{p} \cdot \mathbf{A} = \mathbf{A} \cdot \mathbf{p}$, we then have

$$\begin{aligned}
H &= H_0 + H', \\
H_0 &= \frac{\mathbf{p}^2}{2m_0} + V(\mathbf{r}), \\
H' &= -\frac{q}{m_0} \mathbf{A} \cdot \mathbf{p}.
\end{aligned} \tag{2.27}$$

H' can be consider as the perturbation term due to the photon. Assume the vector potential has the time-harmonic form

$$\mathbf{A} = \hat{e} \frac{A_0}{2} e^{i\mathbf{k}_{\text{op}} \cdot \mathbf{r}} e^{-i\omega t} + \hat{e} \frac{A_0}{2} e^{-i\mathbf{k}_{\text{op}} \cdot \mathbf{r}} e^{i\omega t}, \quad (2.28)$$

where \mathbf{k}_{op} is the wave vector, ω is the optical angular frequency, and \hat{e} is a unit vector in the direction of the electromagnetic field. Hence, we get

$$\begin{aligned} H'(\mathbf{r}, t) &= H'(\mathbf{r})e^{-i\omega t} + H'^{\dagger}(\mathbf{r})e^{i\omega t}, \\ H'(\mathbf{r}) &= -\frac{eA_0 e^{i\mathbf{k}_{\text{op}} \cdot \mathbf{r}}}{2m_0} \hat{e} \cdot \mathbf{p}. \end{aligned} \quad (2.29)$$

Use the long wavelength approximation, which means $\mathbf{k}_{\text{op}} \sim 0$, H' becomes

$$H' \sim -\frac{eA_0}{2m_0} \hat{e} \cdot \mathbf{p}. \quad (2.30)$$

According to the Fermi's golden rule, the transition rate per unit volume in the crystal $R_{a \rightarrow b}$ of electrons from state a with energy E_a to state b with energy E_b (assuming $E_b > E_a$) due to the absorption of a photon with energy E_{op} can be expressed as

$$R_{a \rightarrow b} = \frac{2}{V} \sum_{\mathbf{k}_a} \sum_{\mathbf{k}_b} \frac{2\pi}{\hbar} |\langle b | H'(\mathbf{r}) | a \rangle|^2 \delta(E_b - E_a - E_{\text{op}}) f_a (1 - f_b), \quad (2.31)$$

where the prefactor 2 accounts for the spins, V is the total volume of the crystal, and f is the Fermi-Dirac distribution. Similarly, when the electrons transit from state b to state a because of the emission of a photon with energy $\hbar\omega$, the transition rate per unit volume in the crystal $R_{b \rightarrow a}$ has the form

$$R_{b \rightarrow a} = \frac{2}{V} \sum_{\mathbf{k}_a} \sum_{\mathbf{k}_b} \frac{2\pi}{\hbar} |\langle a | H'(\mathbf{r}) | b \rangle|^2 \delta(E_a - E_b + E_{\text{op}}) f_b (1 - f_a). \quad (2.32)$$

Since $\langle a | H'(\mathbf{r}) | b \rangle = \langle b | H'(\mathbf{r}) | a \rangle$ and $\delta(x) = \delta(-x)$, the absorption coefficient α , which is defined as the net number of photons absorbed per second per unit volume divided by the number of total photons injected per second per unit area, can be written as

$$\alpha(E_{\text{op}}) = \frac{1}{(S/\hbar\omega) V} \frac{2}{\hbar} \sum_{\mathbf{k}_a} \sum_{\mathbf{k}_b} |\langle b | H'(\mathbf{r}) | a \rangle|^2 \delta(E_b - E_a - E_{\text{op}}) (f_a - f_b), \quad (2.33)$$

where S is the magnitude of the optical intensity and can be substituted by $n_r c \epsilon_0 \omega^2 A_0^2 / 2$.

Here, n_r is the refractive index, and c is the speed of light in free space. Using the Eq. (2.30), we get

$$\alpha(E_{\text{op}}) = \frac{\pi q^2}{n_r c \epsilon_0 m_0^2 \omega} \frac{2}{V} \sum_{\mathbf{k}_a} \sum_{\mathbf{k}_b} |\hat{\mathbf{e}} \cdot \langle b | \mathbf{p} | a \rangle|^2 \delta(E_b - E_a - E_{\text{op}}) (f_a - f_b). \quad (2.34)$$

Using the \mathbf{k} -selection rule, and letting $\langle b | \mathbf{p} | a \rangle = M_{ba}$, we have

$$\alpha(E_{\text{op}}) = \frac{\pi q^2}{n_r c \epsilon_0 m_0^2 \omega} \frac{2}{V} \sum_{\mathbf{k}} |\hat{\mathbf{e}} \cdot M_{ba}|^2 \delta(E_b - E_a - E_{\text{op}}) (f_a - f_b). \quad (2.35)$$

If α is negative, we have gain in the medium. So we can write

$$g(E_{\text{op}}) = -\alpha(E_{\text{op}}). \quad (2.36)$$

Since the speed of light in material and the density of states for the photons per unit volume per energy interval around E_{op} are c/n_r and $8\pi n_r^3 E_{\text{op}}^2 / h^3 c^3$, respectively, the stimulated and spontaneous emission rates per unit volume per energy interval around E_{op} are respectively given by

$$\begin{aligned} r_{\text{st}}(E_{\text{op}}) &= \frac{8\pi n_r^2 E_{\text{op}}^2}{h^3 c^2} g(E_{\text{op}}), \\ r_{\text{sp}}(E_{\text{op}}) &= \frac{8\pi n_r^2 E_{\text{op}}^2}{h^3 c^2} \frac{1}{1 - e^{[E_{\text{op}} - (F_c - F_v)]/k_B T}} g(E_{\text{op}}) \\ &= \frac{8\pi n_r^2 E_{\text{op}}^2}{h^3 c^2} \frac{\pi q^2}{n_r c \epsilon_0 m_0^2 \omega} \frac{2}{V} \sum_{\mathbf{k}} |\hat{\mathbf{e}} \cdot M_{ba}|^2 \delta(E_b - E_a - E_{\text{op}}) f_b (1 - f_a). \end{aligned} \quad (2.37)$$

2.3.2 Formulas for quantum structure along [0001]

In a wurtzite heterojunction structure quantized along the z axis, the quantum numbers corresponding to the x - y plane for the quantized states can be expressed by \mathbf{k}_t , where

$k_t = \sqrt{k_x^2 + k_y^2}$. The summations over the quantum numbers \mathbf{k} becomes summations over (\mathbf{k}_t, i, j) , where i and j index respectively the i th conduction subband and the j th valence

subband. So we get

$$\alpha(\hbar\omega) = \frac{\pi q^2}{n_r c \varepsilon_0 m_0^2 \omega} \frac{2}{V} \sum_{i,j} \sum_{\mathbf{k}_t} \sum_{\sigma=\pm} |M_{e,ij}^\sigma(k_t)|^2 \delta(E_i^c(k_t) - E_j^\sigma(k_t) - \hbar\omega) (f_j^\sigma - f_i^c). \quad (2.38)$$

where σ corresponds to the upper (+) and lower (-) block Hamiltonian. The functions f_i^c

and f_j^σ are the Fermi-Dirac distribution functions for the probabilities of electrons

occupying the states $\Phi_i^\pm(\mathbf{r}; \mathbf{k}_t) = \frac{1}{\sqrt{A}} e^{i\mathbf{k}_t \cdot \mathbf{r}} \varphi_i(z; k_t) u_c^\pm$ of conduction subband i and the

state $\Psi_j^\sigma(\mathbf{r}; \mathbf{k}_t) = \frac{1}{\sqrt{A}} e^{i\mathbf{k}_t \cdot \mathbf{r}} \sum_{\mu=1}^3 \psi_{\mu j}^\sigma(z; k_t) u_\mu^\sigma$ of valence subband j , respectively. $M_{e,ij}^\sigma$ is

the e -component ($e = x, y, z$) of the momentum-matrix element for interband transition

between the states $\Phi_i^+(\mathbf{r}; \mathbf{k}_t)$ [or $\Phi_i^-(\mathbf{r}; \mathbf{k}_t)$] and $\Psi_j^\sigma(\mathbf{r}; \mathbf{k}_t)$, with a modulus squared given

by[54]

$$|M_{x,ij}^\sigma|^2 = |M_{y,ij}^\sigma|^2 = \frac{m_0 E_{px}}{8} \sum_{\mu=1,2} \left| \langle \varphi_i | \psi_{\mu j}^\sigma \rangle \right|^2, \quad (2.39)$$

for the TE-polarization component, and

$$|M_{z,ij}^\sigma|^2 = \frac{m_0 E_{pz}}{4} \left| \langle \varphi_i | \psi_{\mu=3,j}^\sigma \rangle \right|^2, \quad (2.40)$$

for the TM-polarization component, where the parameters E_{px} and E_{pz} are defined as

$$E_{px} = \left(\frac{m_0}{m_t} - 1 \right) E_g \frac{(E_g + \Delta_1 + \Delta_2)(E_g + 2\Delta_2) - 2\Delta_3^2}{(E_g + \Delta_1 + \Delta_2)(E_g + \Delta_2) - \Delta_3^2}, \quad (2.41)$$

$$E_{pz} = \left(\frac{m_0}{m_z} - 1 \right) \frac{(E_g + \Delta_1 + \Delta_2)(E_g + 2\Delta_2) - 2\Delta_3^2}{E_g + 2\Delta_2}.$$

Change the summation to the integral form by $\frac{2}{V} \sum_{\mathbf{k}_t} \Rightarrow \frac{1}{L} \int \frac{k_t dk_t}{2\pi}$, we have

$$\alpha(\hbar\omega) = \sum_{i,j} \frac{2\pi q^2}{n_r c \varepsilon_0 m_0^2 \omega L_{ij}} \sum_{\sigma=\pm} \int |M_{e,ij}^\sigma(k_t)|^2 \delta(E_i^c(k_t) - E_j^\sigma(k_t) - \hbar\omega) (f_j^\sigma - f_i^c) \frac{k_t}{2\pi} dk_t, \quad (2.42)$$

where L_{ij} is the width of the region in which the interband process occurs between subbands

i and j . When the scattering relaxation is included, the delta function is replaced by a

Lorentzian function with a intraband relaxation time γ , assumed to be 0.1 ps here, and we obtain

$$\alpha(\hbar\omega) = \sum_{i,j} \frac{2\pi q^2}{n_r c \varepsilon_0 m_0^2 \omega L_{ij}} \sum_{\sigma=\pm} \int |M_{e,ij}^\sigma(k_t)|^2 \frac{\gamma / \pi}{(E_{ij}^\sigma(k_t) - \hbar\omega)^2 + \gamma^2} (f_j^\sigma - f_i^\sigma) \frac{k_t}{2\pi} dk_t, \quad (2.43)$$

where $E_{ij}^\sigma \equiv E_i^c(k_t) - E_j^\sigma(k_t)$ is the interband transition energy between the conduction subband state $\Phi_i^+(\mathbf{r}; \mathbf{k}_t)$ [or $\Phi_i^-(\mathbf{r}; \mathbf{k}_t)$] with energy $E_i^c(k_t)$ and the valence subband state $\Psi_j^\sigma(\mathbf{r}; \mathbf{k}_t)$ with energy $E_j^\sigma(k_t)$.

Similarly, we can obtain the optical gain $g(\hbar\omega)$ and the spontaneous emission rate $r_{\text{sp}}(\hbar\omega)$ for the wurtzite quantum well structure as below

$$\begin{aligned} g(\hbar\omega) &= [1 - e^{-\frac{\hbar\omega - (F_c - F_v)}{k_B T}}] \sum_{ij} g_{\text{sp},ij}^e(\hbar\omega), \quad e = x, y, z, \\ r_{\text{sp}}(\hbar\omega) &= \sum_{ij} r_{\text{sp},ij}(\hbar\omega), \\ g_{\text{sp},ij}^e(\hbar\omega) &= \frac{2q^2 \pi}{n_r c \varepsilon_0 m_0^2 \omega L_{ij}} \sum_{\sigma=\pm} \int |M_{e,ij}^\sigma|^2 \frac{f_i^c (1 - f_j^\sigma) \gamma / \pi}{(E_{ij}^\sigma - \hbar\omega)^2 + \gamma^2} \frac{k_t}{2\pi} dk_t, \\ r_{\text{sp},ij}(\hbar\omega) &= \frac{n_r^2 \omega^2}{\pi^2 \hbar c^2} \frac{2g_{\text{sp},ij}^x + g_{\text{sp},ij}^z}{3}. \end{aligned} \quad (2.44)$$

2.3.3 Optical radiative current density

The component $r_{\text{sp},ij}$ of the spontaneous emission rate is due to the recombination of electrons in conduction subband i and holes in valence subband j . It has the meaning of the number of emitting photons due to the recombinations per unit time per unit volume per unit photon energy interval at energy $\hbar\omega$. The corresponding component of the resulting radiative recombination current density can be written as

$$J_{ij} = qL_{ij} \int r_{\text{sp},ij}(\hbar\omega) d\hbar\omega. \quad (2.45)$$

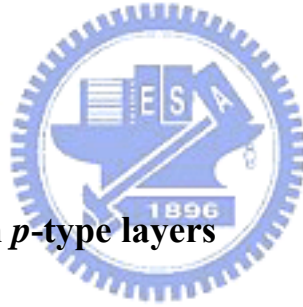
The total current density $J = \sum_{ij} J_{ij}$, which is the sum of all current density components.

2.3.4 Threshold condition

We are mainly interested in the effects of carrier spillover on threshold. For the threshold condition, we use the formula

$$\Gamma \max_{\hbar\omega} g(\hbar\omega) = \alpha, \quad (2.46)$$

where α is the total cavity loss, which includes internal loss and mirror loss, Γ is the optical confinement factor, and $\max_{\hbar\omega} g(\hbar\omega)$ is the peak gain. From the threshold condition, we first obtain the quasi-Fermi levels, F_c and F_v , at threshold. With F_c and F_v , we obtain the carrier distribution in energy space, based on which we further calculate the gain spectra, the spontaneous emission rates, and the recombination current densities at threshold.



2.4 Current transport in *p*-type layers

When we consider the case of current injection in *p*-type layers, three mechanisms are used here, including the drift-diffusion, tunneling and thermionic emission. As illustrated in Fig. 2.3 with valence band profile of GaN/AlGa_N SL as the example, the drift-diffusion model is used for current across the wells (W_1 and W_2) and bulk GaN regions whereas for current through the barriers (B_{12}) we use only the tunneling model for traveling holes with energy between E_2 and E_1 and thermionic emission models for those above E_1 .

2.4.1 Drift-diffusion current

For drift-diffusion current, the conventional model in one dimension form is employed.

$$\begin{aligned}
J_n(z) &= \mu_n n(z) \frac{dF_c(z)}{dz}, \\
J_p(z) &= \mu_p p(z) \frac{dF_v(z)}{dz}, \\
\frac{d[J_n(z) + J_p(z)]}{dz} &= 0.
\end{aligned} \tag{2.47}$$

The relation between the mobility and the doping level at room temperature is considered by the Caughey-Thomas approximation while the temperature dependence of the mobility is assumed to be proportional to $T^{-3/2}$. [60,61]

2.4.2 F-N tunneling current

For the tunneling, we consider only the Fowler-Nordheim (F-N) tunneling for high-energy holes (with energy between E_1 and E_2 , which are the energy levels corresponding to the highest and lowest points of valence-band profile of each barrier, respectively, as indicated in Fig. 2.3) and neglect the direct tunneling due to the small tunneling probability for low-energy holes. Here, we do not consider the defects in the barriers because the amount of defects closely depends on the progress of material growth and device processing technologies. Besides, owing to the large amount of efforts in improving material growth, the quality of nitride film becomes better and better. So, the workers generally do not consider the trap tunneling effect when they studied the electrical properties of AlGaN/GaN superlattices theoretically. [48,49] With the momentum conservation, the tunneling current density, $J_{\text{tunneling}}$, through the barrier B_{12} from well W_1 to the neighboring well W_2 (see Fig. 2.3) can be expressed by [62]

$$J_{\text{tunneling}} = \frac{qm^*}{2\pi^2\hbar} \int_{E_2}^{E_1} \int_{E_2}^E P(E_{\perp}) [f(F_{v1} - E) - f(F_{v2} - E)] dE_{\perp} dE, \tag{2.48}$$

where q is the elementary charge, m^* is the effective mass of holes, [63] \hbar is the reduced Plank constant, E_{\perp} is the energy associated with the transverse motion, P is the

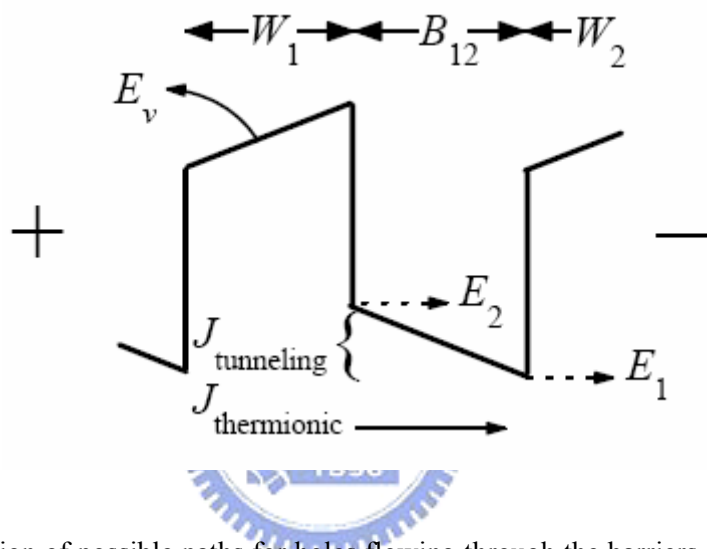


Fig. 2.3 Illustration of possible paths for holes flowing through the barriers. The valence band profile E_v , considering piezoelectric field with Ga-face polarity is drawn as an example. W_1 and W_2 are the symbols for well 1 and well 2, respectively. B_{12} is the barrier between W_1 and W_2 . $J_{\text{tunneling}}$ and $J_{\text{thermionic}}$ are the F-N tunneling and thermionic emission current densities, respectively.

tunneling probability calculated from the well known WKB approximation, f is the Fermi-Dirac distribution function, and F_{v_i} ($i=1,2$) is the valence-band Fermi level at the interface between W_i and B_{12} .

2.4.3 Thermionic emission current density

For thermionic emission, we assume that the carriers in the wells are in quasi-equilibrium so that the Fermi-Dirac distribution and thus the Boltzmann distribution for energetic carriers can be employed. We also assume that the barriers are thin enough so that there should be no scattering during thermionic emission. As a result, the thermionic current density, $J_{\text{thermionic}}$, from well W_1 to the neighboring well W_2 can be written as [64,65]

$$J_{\text{thermionic}} = A^* T^2 \left[\exp\left(\frac{E_1 - F_{v2}}{k_B T}\right) - \exp\left(\frac{E_1 - F_{v1}}{k_B T}\right) \right], \quad (2.49)$$

where A^* is the effective Richardson constant and is taken as $25 \text{ A cm}^{-2} \text{ K}^{-2}$. [66]

2.5 Numerical methods

2.5.1 Basis expansion for multilayer quantum structure

In order to calculate the effective-mass equations in Eq. (2.19) and (2.20), we can choose one set of orthonormal bases to expand the envelope functions. Here, sine functions are employed. Take ψ^+ as an example, we have

$$\psi_v^+(z) = \sqrt{\frac{2}{L}} \sum_{m=1}^M c_m^v \sin\left(\frac{m\pi}{L} z\right), \quad (2.50)$$

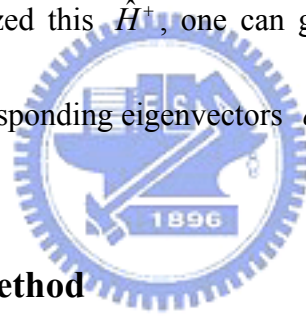
where L is the total length of the system, and $\sqrt{2/L}$ is the normalization factor. The effective-mass equation for the upper block of the Hamiltonian becomes

$$\begin{aligned}
& \sum_{\nu=1}^3 [\hat{H}_{\mu\nu}^+(k_z; k_t) + E_\nu^0(z)\delta_{\mu\nu}] \sqrt{\frac{2}{L}} \sum_{m=1}^M c_m^\nu \sin\left(\frac{m\pi}{L} z\right) \\
& = E \sqrt{\frac{2}{L}} \sum_{m'=1}^M c_{m'}^\mu \sin\left(\frac{m'\pi}{L} z\right), \quad \mu = 1, 2, 3.
\end{aligned} \tag{2.51}$$

Multiplying by $\sqrt{2/L} \sin(n\pi z/L)$ and integrating over z from 0 to L yields

$$\begin{aligned}
& \sum_{\nu=1}^3 \sum_{m=1}^M \hat{H}_{\mu\nu, nm}^+ c_m^\nu = E c_n^\mu, \quad \mu = 1, 2, 3, \\
& \hat{H}_{\mu\nu, nm}^+ = \int_0^L \frac{2}{L} \sin\left(\frac{n\pi}{L} z\right) \hat{H}_{\mu\nu}^+ \sin\left(\frac{m\pi}{L} z\right) dz,
\end{aligned} \tag{2.52}$$

where the z -dependent valence band edge E_ν^0 is dropped for convenience. Note that when integrating over z , the corresponding material parameters should be taken. By the expansion of M sine functions, the upper block of Hamiltonian \hat{H}^+ is then expressed by a $3M \times 3M$ matrix. After linear diagonalized this \hat{H}^+ , one can get the eigenvalues as the quantized state energies E 's and the corresponding eigenvectors c^ν 's for envelop functions ψ_ν^+ 's.



2.5.2 Finite difference method

In order to calculate a banded band profile of the heterostructure grown along the z axis, it is necessary to include the screening potential ϕ by 1-D Poisson equation:

$$\frac{\partial}{\partial z} [\varepsilon(z) \frac{\partial}{\partial z} \phi(z)] = -\frac{q}{\varepsilon_0} [p(z) - n(z) + N_d^+(z) - N_a^-(z)], \tag{2.53}$$

where $\varepsilon(z)$ is the relative permittivity as z -dependence, ε_0 is the permittivity in free space, q is the elementary charge, and $p(z)$, $n(z)$, $N_d^+(z)$ and $N_a^-(z)$ are the concentrations of holes, electrons, ionized donors and acceptors, respectively, and are given by

$$\begin{aligned}
n(z) &= N_c(z) \exp\left(\frac{F_c(z) - E_c(z)}{k_B T}\right), \\
p(z) &= N_v(z) \exp\left(\frac{E_v(z) - F_v(z)}{k_B T}\right), \\
N_d^+(z) &= \frac{N_d(z)}{1 + g_d \exp\left(\frac{F_c - E_d}{k_B T}\right)}, \\
N_a^-(z) &= \frac{N_a(z)}{1 + g_a \exp\left(\frac{E_a - F_v}{k_B T}\right)},
\end{aligned} \tag{2.54}$$

where N_c and N_v are the densities of states for electrons and holes, respectively. g_d and g_a are the ground-state degeneracy of the donor and acceptor levels, respectively. E_d and E_a are the ionization energies for donors and acceptors, respectively. Note that, the electron and hole concentrations at the quantized region should be modified by Eq. (2.22).

By means of the finite difference method, the space is separated into N pieces. If we index the physical quantities at the i th point ($i = 1 \sim N+1$) as ϕ_i , ε_i , p_i , n_i , $N_{d,i}^+$, and $N_{a,i}^-$ in the 1-D system with length of L , the Poisson equation will become

$$\frac{\varepsilon_i \frac{\phi_{i+1} - \phi_i}{h_{i+1,i}} - \varepsilon_{i-1} \frac{\phi_i - \phi_{i-1}}{h_{i,i-1}}}{\frac{h_{i+1,i} + h_{i,i-1}}{2}} = -\frac{q}{\varepsilon_0} [p_i - n_i + N_{d,i}^+ - N_{a,i}^-], \tag{2.55}$$

where $h_{i,j}$ is the distance between i th and j th points. The boundary condition at the interface is

$$\varepsilon_i \frac{\phi_{i+1} - \phi_i}{h_{i+1,i}} = \varepsilon_{i-1} \frac{\phi_i - \phi_{i-1}}{h_{i,i-1}}. \tag{2.56}$$

The potential at i can be obtained from the charge concentration at i and the potential at $i+1$ and $i-1$. A new ϕ_i will change the band profile E_c (E_v) and hence charge concentration at i . Therefore, Newton method is used to find the self-consistent ϕ_i .

Note that the larger N we take, the more accuracy we will get, but more time will be spent. The pieces of the system are not necessarily being uniform. So the points can be taken

densely around the interface, where the potential generally varies obviously, but be taken sparsely at other regions, where the potential varies smoothly.

2.5.3 Jacobian-Newton iteration scheme

The Jacobian-Newton iterative numerical method, which contains an outer-loop Poisson equation by the Jacobian method and an inner-loop Poisson equation by Newton method, is performed here to prevent numerical instability.[67]

We assume the current densities at both edges of the whole system are continuous. Hence, the hole concentration and the energy difference between the quasi-Fermi level and the valence band edge are fixed at both edges of the system. A flow diagram (Fig. 2.4) is drawn to illustrate the iteration steps we used here. From the essential of this method, we first give an initial guess of potential profile. The charge concentrations at each point can be obtained. Solving Eq. (2.55) or (2.56) by Newton method, we will have the self-consistent ϕ_i and charge concentration at i th point. Then, using the current equation, we will find a new Fermi level at i th point. After calculating every point sequentially, we will have a new set of Fermi levels at every point for the next loop of Jacobian iteration. Repeat this loop again and again until the potential at every point is convergent.

Note that the equations for current densities at every region are different. The calculation of current density at the barrier region is not necessary since we assume the holes pass by tunneling and thermionic emission. Besides, the carrier concentration in the quantized regions can be modified by Eq. (2.22).

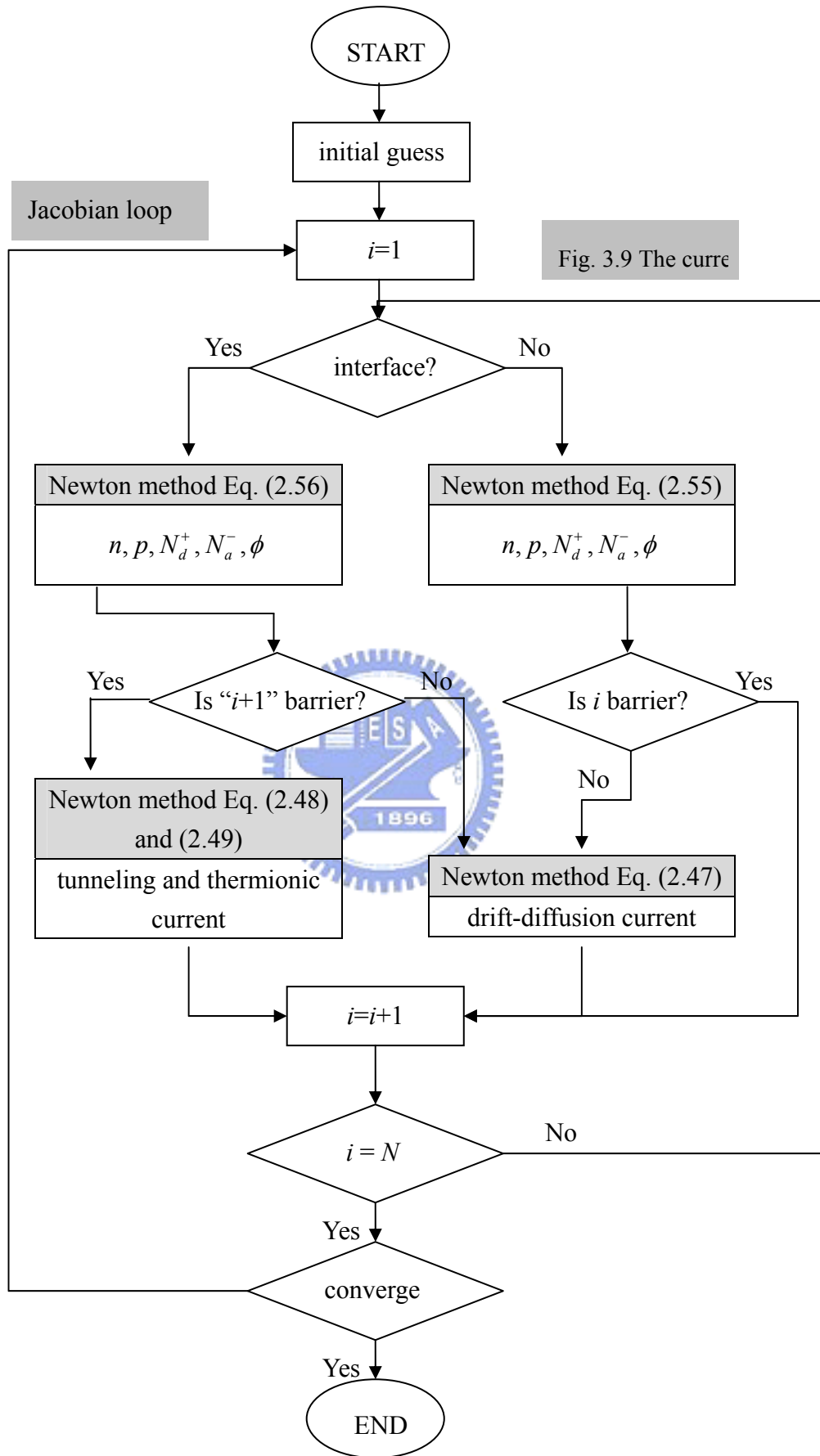


Fig. 3.9 The curre

Fig. 2.4 Flow diagram for Jacobian-Newton iteration

2.5.4 Material parameters

Table 2.1 Material parameters for $\mathbf{k}\cdot\mathbf{p}$ Luttinger-Kohn Hamiltonian used here[8]

Parameters	GaN	AlN	InN
a_{1c} (Å) at 300 K	3.189	3.112	3.545
E_g (eV)	3.510	6.25	0.78
α (meV/K)	0.909	1.799	0.245
β (K)	830	1462	624
Δ_{cr}, Δ_{so} (eV)	0.01, 0.017	-0.169, 0.019	0.04, 0.005
m_e	0.2	0.31	0.07
A_1	-7.21	-3.86	-8.21
A_2	-0.44	-0.25	-0.68
A_3	6.68	3.58	7.57
A_4	-3.46	-1.32	-5.23
A_5	-3.40	-1.47	-5.11
A_6	-4.90	-1.64	-5.96
D_1	-3.7	-17.1	-3.7
D_2	4.5	7.9	4.5
D_3	8.2	8.8	8.2
D_4	-4.1	-3.9	-4.1
C_{11}	390	396	223
C_{12}	145	137	115
C_{13}	106	108	92
C_{33}	398	373	224
d_{31}	-1.6	-2.1	-3.5

Chapter 3

Radiative Leakage Current

We consider the wurtzite III-nitride lasers with a conventional step separate-confinement heterostructure that contains an active region of strained InGaN/GaN QWs and is inserted with an AlGaN EBL immediately near the QWs, as indicated in Fig. 3.1.[28] The layers are considered to be grown on strain-free GaN along the crystallographic c -axis which is defined as the z axis.

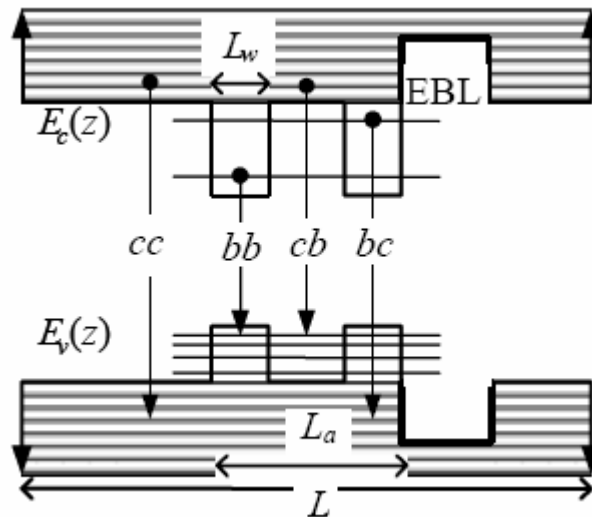


Fig. 3.1 Schematic illustration of the band diagram of the neighborhood of the InGaN/GaN QW active region inside which four different kinds (bb , cb , bc , and cc) of interband processes occur. The cb (bb) process means the interband process between the continuous (bound) conduction and the bound valence subbands while the bc (cc) means the process between the bound (continuous) conduction and the continuous valence subbands. The well has a width L_w and the active region has a width L_a . The continuous subbands are simulated by dense discrete subbands that are discretized using two infinite potential boundaries. An AlGaN EBL is placed immediately near the active region.

3.1 Some assumptions and definitions

3.1.1 Flat-band approximation

We take the flat-band approximation to calculate the band structure of the QWs. This is a good approximation for narrow QWs considered in this study, even if the strain-induced piezoelectric field in the InGaN QWs may be considerable.[68-76] At threshold condition, the piezoelectric field is strongly suppressed by the screening of the large density of carriers (generally in the range of $10^{19} \sim 10^{20} \text{ cm}^{-3}$),[77-79] further justifying the flat-band approximation. It has also been pointed out that in this range of threshold carrier density, there is a small difference from the case of fully screening in the transition energy and the recombination rate between the lowest conduction and valence subbands.[80] Franssen et al., have experimentally demonstrated that the polarization-induced electric field can be almost fully screened in nitride LDs close to lasing threshold, supporting our assumption of the flat-band approximation.[81,82]

3.1.2 Transitions involving continuous states

Besides the discrete subbands bound by the barriers, we also consider the spillover of carriers to the continuous subband states which are above at least one side of the potential barriers in energy. We obtain the wave functions and the energy of the continuous subband states also using equations for the bound subband states, except that we use two infinite boundaries at positions sufficiently far away from each other for the continuous subbands, as illustrated in Fig. 3.1, where we include the EBL in the structure. Consequently, we obtain discrete subbands dense enough to realistically simulate the physical property of the real continuous subbands. Such infinite boundaries have been employed for the calculation

of the continuous subband states in previous articles.[23,83] Justification and detailed discussion for the infinite boundaries can be found there.

Hence, both the conduction and valence states are divided into two groups, the continuous ones and the bound ones. The interband optical transitions in the active region can be therefore categorized into four parts: 1) the bound-to-bound (*bb*), 2) the bound-to-continuous (*bc*), 3) the continuous-to-bound (*cb*), and 4) the continuous-to-continuous (*cc*) transitions, as indicated in Fig. 3.1.

3.1.3 Radiative current density

According to the previous section, the total radiative current density can also be considered as composed of four components, $J = J_{bb} + J_{bc} + J_{cb} + J_{cc}$. As illustrated in Fig. 3.1, the component J_{bb} is caused by the transitions from all the bound conduction subbands to all the bound valence subbands, the J_{bc} one is caused by the transitions from all the bound conduction subbands to all the continuous valence subbands, and J_{cb} (J_{cc}) is caused by the transitions from all the continuous conduction subbands to all the bound (continuous) valence subbands. These current components can be obtained by

$$J_{bb} = \sum_i^b \sum_j^b J_{ij}, \quad J_{bc} = \sum_i^b \sum_j^c J_{ij}, \quad J_{cb} = \sum_i^c \sum_j^b J_{ij}, \quad \text{and} \quad J_{cc} = \sum_i^c \sum_j^c J_{ij}, \quad (3.1)$$

where the symbols b and c over the sigmas mean summations over bound subbands and continuous subbands, respectively. For convenience in later analysis, the optical gain g and the spontaneous emission r_{sp} rate are also considered as composed of four components ($g = g_{bb} + g_{bc} + g_{cb} + g_{cc}$ and $r_{sp} = r_{sp,bb} + r_{sp,bc} + r_{sp,cb} + r_{sp,cc}$) with their expressions similar to Eqs. (3.1).

It has been mentioned above that the electron leakage into the p -type cladding layer can be alleviated by the employment of EBL. Moreover, the main interest here is the

investigation on the radiative current density involving the transitions from the continuous states, so the electron leakage over the EBL is ignored through this work. As for the leakage due to the nonradiative current, it relies on the material quality and processing technologies, and hence we skip this issue.

3.2 Result and Discussion

In this section we present the calculated results and detailed analysis of the optical gains, the spontaneous emission, and the recombination current densities for $\text{In}_{0.2}\text{Ga}_{0.8}\text{N}/\text{GaN}$ QW lasers inserted with a 20 nm $\text{Al}_{0.2}\text{Ga}_{0.8}\text{N}$ EBL under the influence of the carrier spillover. All the values of the material parameters used in our calculation can be found from [8] for wurtzite GaN, InN, and AlN. The values for the ternary compounds InGaN and AlGaN are obtained by linear interpolation between the binary compounds, except for the band gap energy for which a bowing parameter of 1.4 eV is used for InGaN and that of 0.7 eV for AlGaN.[8] The band offset is a factor important in studying the spillover of carriers from the bound subbands. Unfortunately, till now there have been no compelling unambiguous values for the band offset of the nitride heterointerfaces. We thus take the valence band offset (VBO), ΔE_v , or equivalently the valence-band partition ratio Q_v as a variable parameter, where $\Delta E_v = Q_v \Delta E_g$ (ΔE_g is the band gap difference), and investigate the dependence of carrier spillover on the band offset. In the determination of the threshold condition, we assume that the lasers have structures such that the confinement factor $\Gamma = 3 \times 10^{-4} L_a$, where L_a is the active region width in units of Å. This gives $\Gamma = 1.5\%$ for a 50 Å QW, a value reasonable for typical III-nitride LDs. The total loss of the cavity is set at $\alpha = 60 \text{ cm}^{-1}$ for the threshold condition Eq. (2.46) except in the case where the loss α is considered as a variable parameter. The temperature is set at $T = 300 \text{ K}$ except in the

case where we investigate the dependence of carrier spillover on temperature.

The density of carriers at threshold in our calculation is in the range from 2×10^{19} to $6 \times 10^{19} \text{ cm}^{-3}$, depending on the well width, the cavity loss, and the temperature. At the high carrier concentration, it is feasible to employ the flat-band approximation in studying the effects of carrier spillover for InGaN laser diodes here.

3.2.1 Undoped Structure

Figure 3.2 shows the current densities, J , J_{bb} , and J_0 , versus the peak gain for single-QW structures with well widths $L_w = 3.6 \text{ nm}$ and 5.4 nm , assuming the partition ratios $Q_v = 0.33$ in panel (a) and $Q_v = 0.45$ in panel (b). Here, for comparison, we include the current density J_0 which is calculated without considering the continuous subbands; that is, in calculating J_0 we assume all the carriers to be at the bound subband states. In our calculation, it is found that the current-density components J_{bc} and J_{cc} , involving the valence continuous subbands in the transition processes, are negligibly small compared with the other components J_{bb} and J_{cb} . This is because the density of states of the valence bands is much higher than that of the conduction bands. All the holes hence almost lie in the lowest bound subbands. Therefore we do not show the curves for J_{bc} and J_{cc} in Fig. 3.2 and henceforth we will not present calculated results concerning transition processes involving the continuous valence subbands. As a result, the difference $J - J_{bb} \approx J_{cb}$ can reveal the influence of electron spillover into the continuous subbands on the threshold current density. The electron spillover is more prominent as more carriers are injected into the active region. This leads to an increase in the difference $J - J_{bb}$ with the peak gain, as can be seen from the figure. It is also found that the difference $J - J_{bb}$ is larger for larger Q_v since the spillover of electrons is more prominent from a shallower QW. For $Q_v = 0.45$, the difference $J - J_{bb}$ is larger for $L_w = 5.4 \text{ nm}$ in general than for $L_w = 3.6 \text{ nm}$. Since

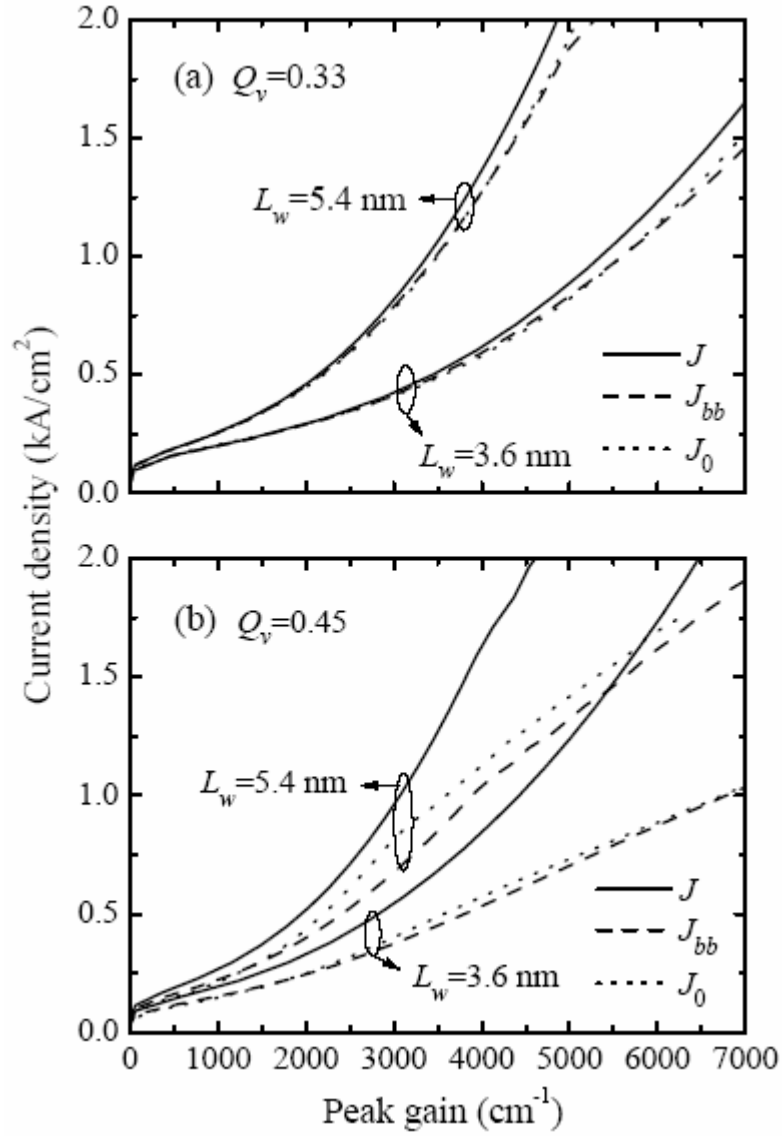


Fig. 3.2 The current densities, J , J_{bb} , and J_0 , versus the peak gain for In_{0.2}Ga_{0.8}N/GaN single-QW LDs with well width $L_w = 3.6$ and 5.4 nm, assuming the partition ratio $Q_v = 0.33$ in panel (a) and $Q_v = 0.45$ in panel (b). The J is the total current density, the J_{bb} is due to the bb process, and the J_0 is calculated without considering the continuous subbands.

the currents also depend on the well width, one cannot conclude that the electron spillover is more considerable in a wider well. Contrarily, more percentage of electrons spill from the narrower well for which the bound subband edges are closer to the barrier. It should be noted that for $Q_v = 0.45$ there is an appreciable difference between J and J_0 both for $L_w = 3.6$ nm at threshold ($\max g \approx 5600 \text{ cm}^{-1}$) and for $L_w = 5.4$ nm at threshold ($\max g \approx 3700 \text{ cm}^{-1}$). This means that one may obtain an incorrect threshold current without the electron spillover effect taken into account, and also may have a misunderstanding of the carrier distribution both in energy and in space. As will be seen later, such an incorrect carrier distribution may cause a significant deviation of gain and spontaneous emission spectra.

To give an insight into the carrier spillover effect on the optical property of QW active regions, we show in Fig. 3.3 the gain spectra g and their components g_{bb} and g_{cb} at threshold for single-QW structures with $L_w = 3.6$ nm, assuming $Q_v = 0.33$ in panel (a) and $Q_v = 0.45$ in panel (b). For comparison, we also show the gain spectra g_0 which are obtained without considering the carrier spillover. By comparing the curves in both the panels, we find that the electron spillover effect can be neglected for $Q_v = 0.33$, but for $Q_v = 0.45$ the component g_{cb} gives a more contribution to the total gain g in the high energy range, resulting in a broader gain spectrum g , due to a larger number of electrons spilling over to the continuous subband states. The spillover also results in a significant blue shift of the peak gain. However, g_{cb} gives only a small contribution to the peak gain although, as has been seen in Fig. 3.2 (b), the cb process can give a significant current density J_{cb} . There is a qualitative difference between the profiles of the gain spectra g and g_0 for $Q_v = 0.45$. The long tail of the g_0 spectrum for $Q_v = 0.45$ is caused by a broad distribution of electrons in the two-dimensional momentum space.

It should be mentioned that among the continuous subbands, the lowest quasi-bound

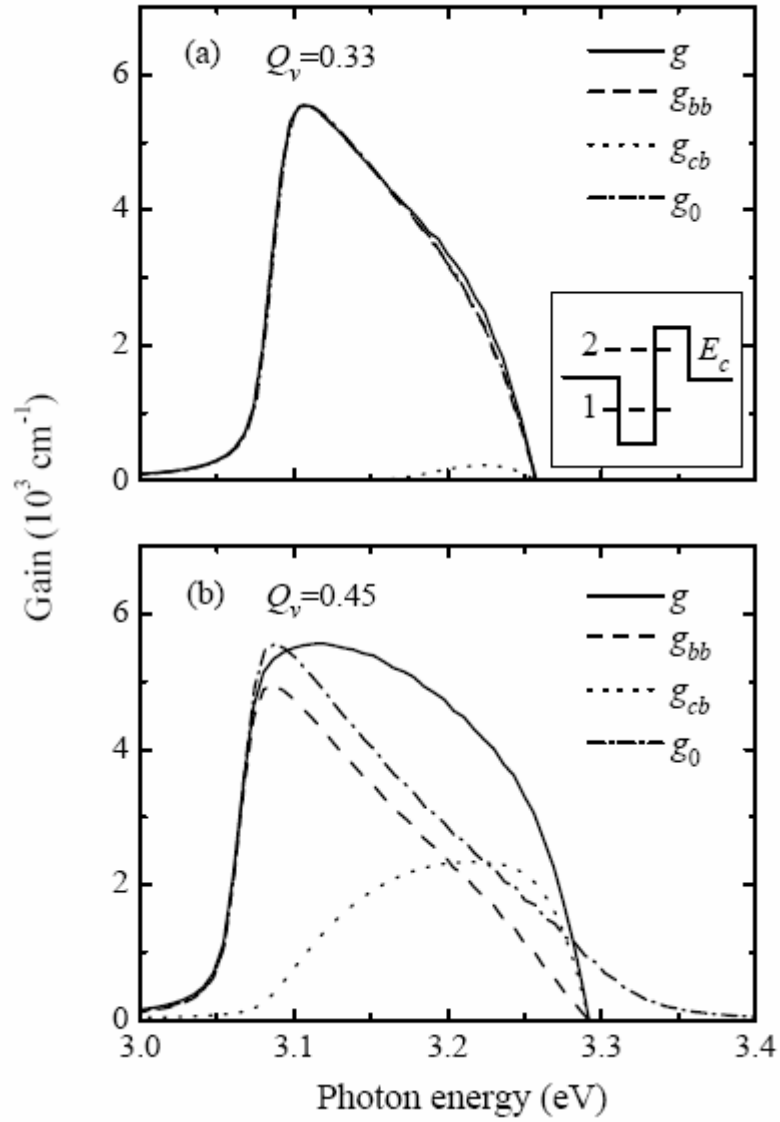


Fig. 3.3 The gain spectra at threshold for $\text{In}_{0.2}\text{Ga}_{0.8}\text{N}/\text{GaN}$ single-QW structures with $L_w = 3.6$ nm, assuming $Q_v = 0.33$ in panel (a) and $Q_v = 0.45$ in panel (b). The spectra g are the total gain, the spectra g_{bb} (g_{cb}) are due to the bb (cb) process, and the ones g_0 are obtained without considering the continuous subbands. Inset is an illustration of the conduction band profile of the QW with the level of the lowest bound subband edge (level 1) and that of the lowest quasi-bound subband edge (level 2).

subband and those around it in energy provide the states for electrons that are dominant in the cb transition process. Inseted in Fig. 3.3 (a) is the conduction band profile of the QW with the level of the lowest bound subband edge (level 1) and that of the lowest quasi-bound subband edge (level 2). The quasi-bound subband states form a standing wave in the z direction and thus have a nature of resonance. Because of the resonance nature, the wave functions of the quasi-bound subbands and their neighbors are much more localized around the QW than those of other subbands. As a result, these more localized subband states give a much larger interband matrix element $M_{e,ij}^\sigma$ than others and hence play a dominant part in the cb process. The cb process can also cause broadening of the spontaneous emission spectrum.

Figure 3.4 shows the spectra r_{sp} of the total spontaneous emission rate and their components $r_{sp,bb}$ and $r_{sp,cb}$ at threshold for single-QW structures with $L_w = 3.6$ and 5.4 nm, similarly assuming $Q_v = 0.33$ in panel (a) and $Q_v = 0.45$ in panel (b). As expected, the spectra r_{sp} are broader for $Q_v = 0.45$ compared to those for $Q_v = 0.33$ because of more contribution from $r_{sp,cb}$ for the shallower electron QW. For the narrower QW ($L_w = 3.6$ nm) the numbers of carriers needed for threshold are larger, giving the higher and broader spectra r_{sp} . It can be found that there is a subordinate peak at photon energy of 3.18 eV in $r_{sp,bb}$ (and r_{sp}) for $Q_v = 0.33$ and $L_w = 5.4$ nm. No distinct subordinate peak is found in the other $r_{sp,bb}$ spectra. Such a subordinate peak is caused mainly by the optical transition from the second bound conduction subband which does not exist in the other QW structures.

As is well known, for QW lasers the threshold current density J increases as the well width L_w decreases in the range of small well width. This is because the number of

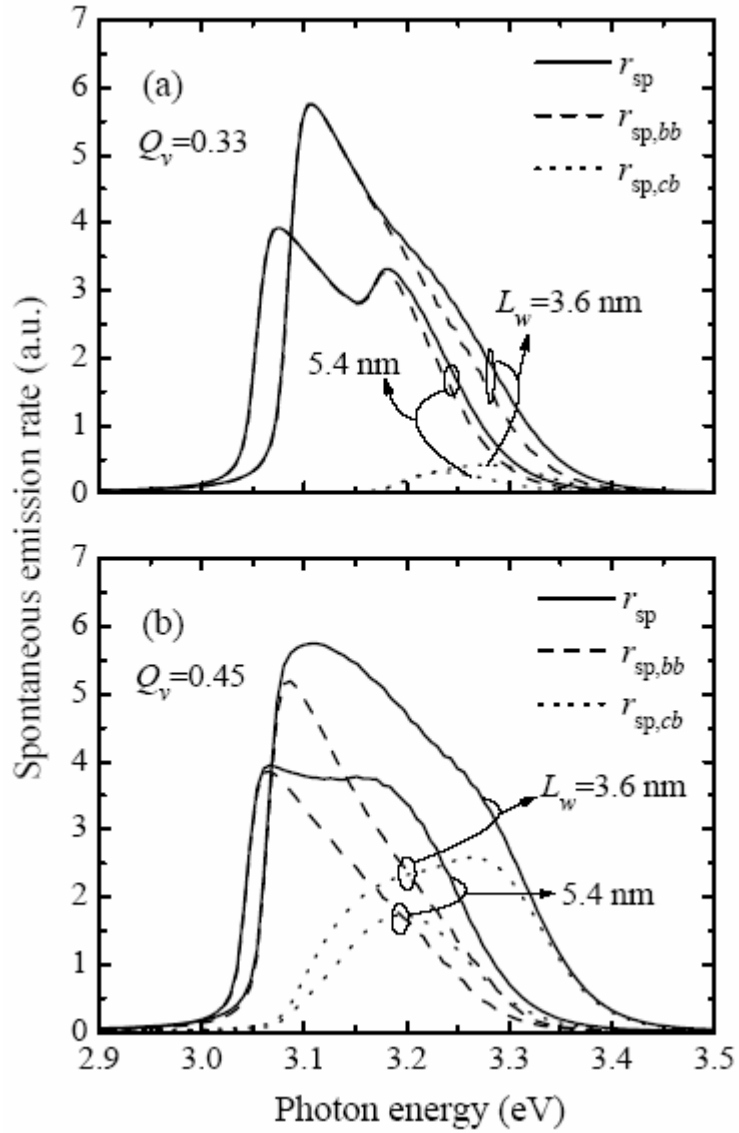


Fig. 3.4 The spectra of spontaneous emission rates at threshold for In_{0.2}Ga_{0.8}N/GaN single-QW structures with $L_w = 3.6$ and 5.4 nm, assuming $Q_v = 0.33$ in panel (a) and $Q_v = 0.45$ in panel (b). The spectra r_{sp} are the total spontaneous emission rate and the ones $r_{sp,bb}$ ($r_{sp,cb}$) are due to the bb (cb) process.

carriers needed for threshold increases superlinearly with decreasing L_w . On the other hand, in the range of large well width, the threshold current also increases with increasing L_w because of the wide active region for carrier recombination. As a result, one expects a minimum value of J in the J - L_w curve at an optimum L_w . Nevertheless, the carrier spillover makes the situation more complicated. To see this, we show in Fig. 3.5 the ratio J_{cb}/J at threshold versus the well width L_w with Q_v as a variable parameter. Such a J_{cb}/J ratio can be considered as a measure of the electron spillover to the continuous subbands. As expected, the spillover (and thus the ratio J_{cb}/J) is more serious for larger Q_v . For a small well width, the spillover is more sensitive to the variation of Q_v when Q_v is larger (for a shallower electron QW). As L_w increases from a small value (2.4 nm), each of the ratios J_{cb}/J first decreases to a local minimum and then goes up. The decrease of J_{cb}/J with increasing L_w is caused by the increase of the optical confinement factor Γ that reduces the carrier density needed for threshold, and then alleviates the spillover of electrons to the continuous subbands. However, with increasing L_w , the lowest quasi-bound subband moves downward and the separation decreases between the bound and the lowest quasi-bound subbands. This increases the electron spillover to the lowest quasi-bound subband and its neighbors. The interplay of the two counteractive effects causes the curves of J_{cb}/J to go down and then up with increasing L_w until the lowest quasi-bound subband has its edge below the barriers in energy and becomes the highest bound subband. Around the critical point at which the subband changes from a quasi-bound to a bound nature, J_{cb}/J reaches a local maximum, as shown in the curves for $Q_v = 0.33$ and 0.37 in Fig. 3.5. To the right of the dashed line in the figure, the second bound subband appears and the curves again go down and then up, governed by the variations of the confinement factor Γ and the position of the new lowest quasi-bound subband. Such going down and then up of J_{cb}/J continues as the L_w increases. Finally, as $L_w \rightarrow \infty$, $J_{cb}/J \rightarrow 0$ which is the value for a three-dimensional active region. It can be found from

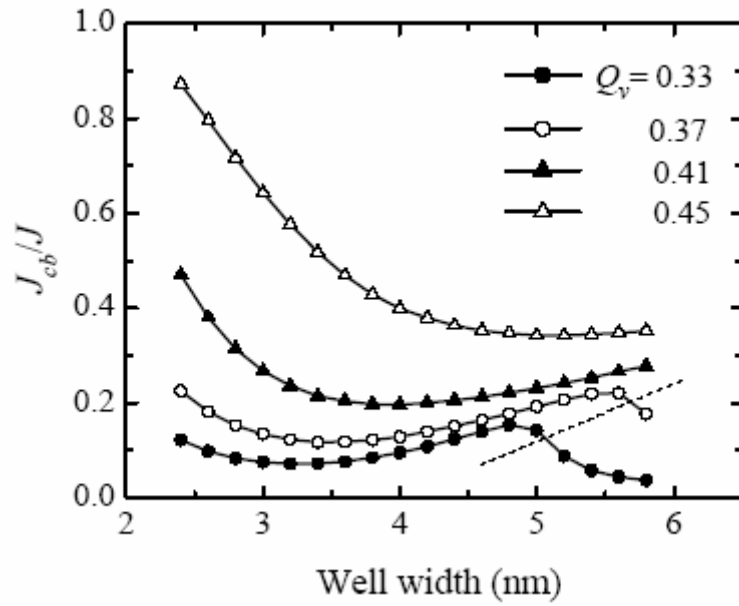


Fig. 3.5 The ratio J_{cb}/J for $\text{In}_{0.2}\text{Ga}_{0.8}/\text{GaN}$ single-QW LDs at threshold versus the well width L_w with Q_v as a variable parameter ($Q_v = 0.33, 0.37, 0.41, \text{ and } 0.45$). The dashed line indicates the boundary across which the lowest quasi-bound subband changes to a bound subband.

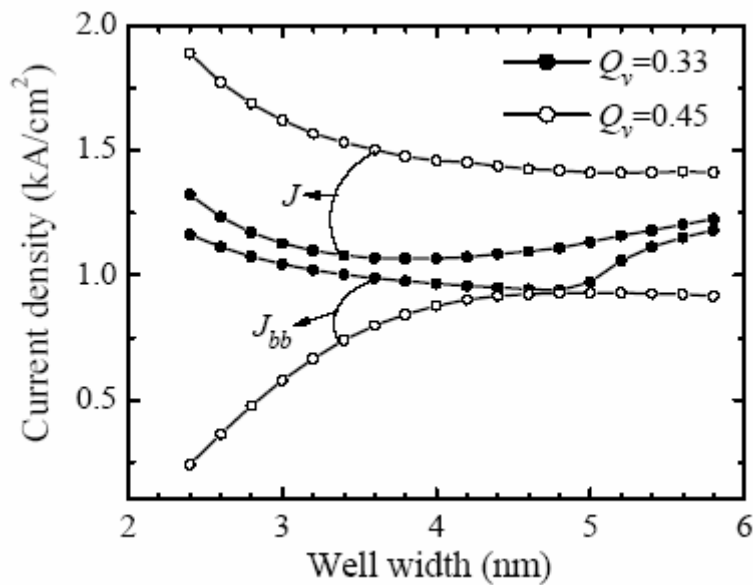


Fig. 3.6 The current densities J and J_{bb} for $\text{In}_{0.2}\text{Ga}_{0.8}/\text{GaN}$ single-QW LDs at threshold as a function of L_w for $Q_v = 0.33$ and 0.45 .

Fig. 3.5 that the cb process may become dominant in the optical properties of the QW structures if L_w becomes small for a large Q_v . This situation should be avoided to take advantage of low threshold in a two-dimensional QW.

Figure 3.6 shows the current densities J and J_{bb} at threshold as a function of L_w for $Q_v = 0.33$ and 0.45. Now we can figure out the variations of the curves with the aid of the explanations for Fig. 3.5. We can take a QW of width in the range of 3~5 nm for $Q_v = 0.33$ and in the range of 4~6 nm for $Q_v = 0.45$ for a low threshold. From the viewpoint of device design, such wide ranges of well width can allow a freedom of choosing a desired emission wavelength from a wide spectral range. As expected, we find a minimum of J_{bb} and a local maximum of $J_{cb} = J - J_{bb}$ for $Q_v = 0.33$ at $L_w = 4.8$ nm around which the lowest quasi-bound subband changes to the highest bound subband.

The carrier spillover depends also on the cavity loss α that determines the carrier density required for threshold. Figure 3.7 shows the ratio J_{cb}/J at threshold versus the well width L_w for $Q_v = 0.33$ and 0.45 with α as a variable parameter. As the figure shows, the spillover can be significantly reduced by decreasing the cavity loss α . This implies that a long cavity is preferred to alleviate the spillover effect, especially when Q_v is large.

As has been pointed out, the carrier spillover and the threshold current can be significantly reduced by increasing the well width L_w for a large Q_v . However, this will cause red shift in the emission wavelength and may sacrifice the purpose of short-wavelength emission. To reduce the electron spillover and simultaneously keep a short-wavelength emission, one can employ a structure of multiple QWs. Figure 3.8 shows the current densities J , J_{bb} , and J_{cb} at threshold versus the number of QWs in the active region for $Q_v = 0.33$ and 0.45. The width of each QW is fixed at $L_w = 3.6$ nm. As can be

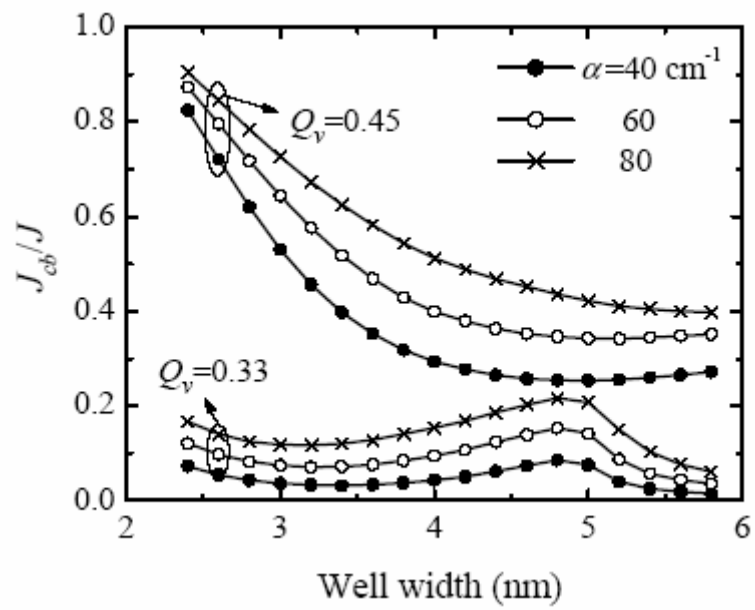


Fig. 3.7 The ratio J_{cb}/J for $\text{In}_{0.2}\text{Ga}_{0.8}/\text{GaN}$ single-QW LDs at threshold versus the well width L_w for $Q_v = 0.33$ and 0.45 with the cavity loss α as a variable parameter ($\alpha = 40, 60,$ and 80 cm^{-1}).

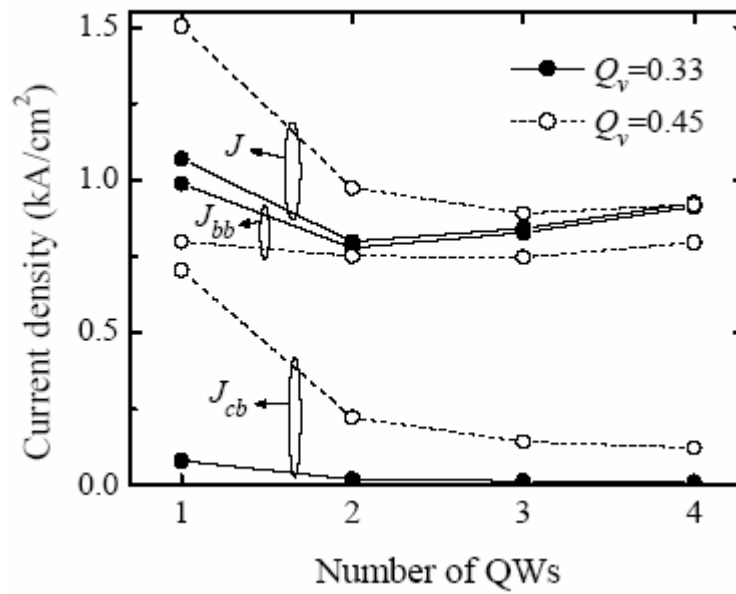


Fig. 3.8 The current densities J , J_{bb} , and J_{cb} of $\text{In}_{0.2}\text{Ga}_{0.8}\text{N}/\text{GaN}$ multi-QW LDs at threshold versus the number of QWs for $Q_v = 0.33$ and 0.45.

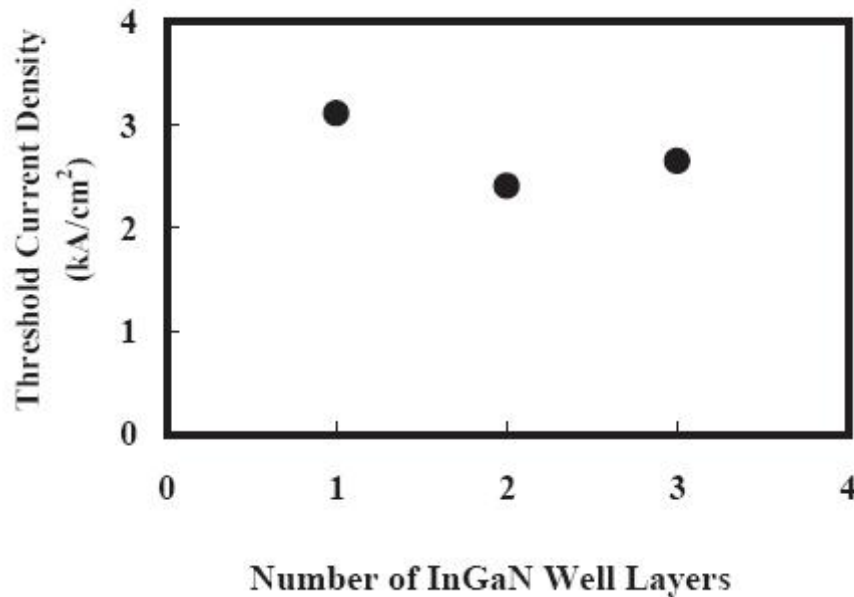


Fig. 3.9 The current densities of InGaN/GaN multi-QW LDs at threshold versus the number of QWs in Nagahama's paper.[84]

seen, the current density J_{cb} is considerably reduced for $Q_v = 0.45$ as the QW number increases from 1 to 2. Consequently, this causes a considerable reduction of the total threshold current density J for $Q_v = 0.45$. As the QW number changes from 2 to 3, there is a slight reduction in J_{cb} but no appreciable change in J_{bb} for $Q_v = 0.45$. Further increasing the QW number does not significantly reduce J_{cb} but causes an increase of J_{bb} , implying that a triple-QW structure is preferred for a low threshold when $Q_v = 0.45$. For $Q_v = 0.33$, a double-QW structure seems preferred for low threshold. The similar tendency is shown experimentally by Nagahama in 2001, as indicated in Fig. 3.9, except the magnitude of the threshold current density, which may result from the poor quality of the crystal, different structure parameters or other kinds of current leakage.[84]

Finally, it is worthwhile to make clear the influence of temperature variation on the electron spillover since the heat dissipation is still a critical issue for the nitride LDs. The rise in temperature causes a broadening of carrier distribution in energy. Therefore, we also expect spectral broadening in the gain g and the spontaneous emission rate r_{sp} with the temperature rising. This can be seen from Fig. 3.10, which is the plot of the g and the r_{sp} spectra of 3.6 nm single-QW structures at two different temperatures $T = 300$ and 400 K for (a) $Q_v = 0.33$ and (b) $Q_v = 0.45$. The broadness of the spectra for $Q_v = 0.45$ at $T = 400$ K in Fig. 3.10 (b) means that the electron spillover is more serious at higher temperature when the QW is shallow.

Figure 3.11 shows the various current densities at threshold as functions of temperature T for the 3.6 nm single-QW structures with $Q_v = 0.33$ and 0.45. With rising T , the J_{cb} at threshold increases more for $Q_v = 0.45$ than for $Q_v = 0.33$ due to a smaller separation between the lowest quasi-bound and the true bound subbands for the shallower QW. Quite differently, the J_{bb} decreases for $Q_v = 0.45$ but increases for $Q_v = 0.33$ with rising T . This can be understood by the fact that the distribution probability function becomes flatter

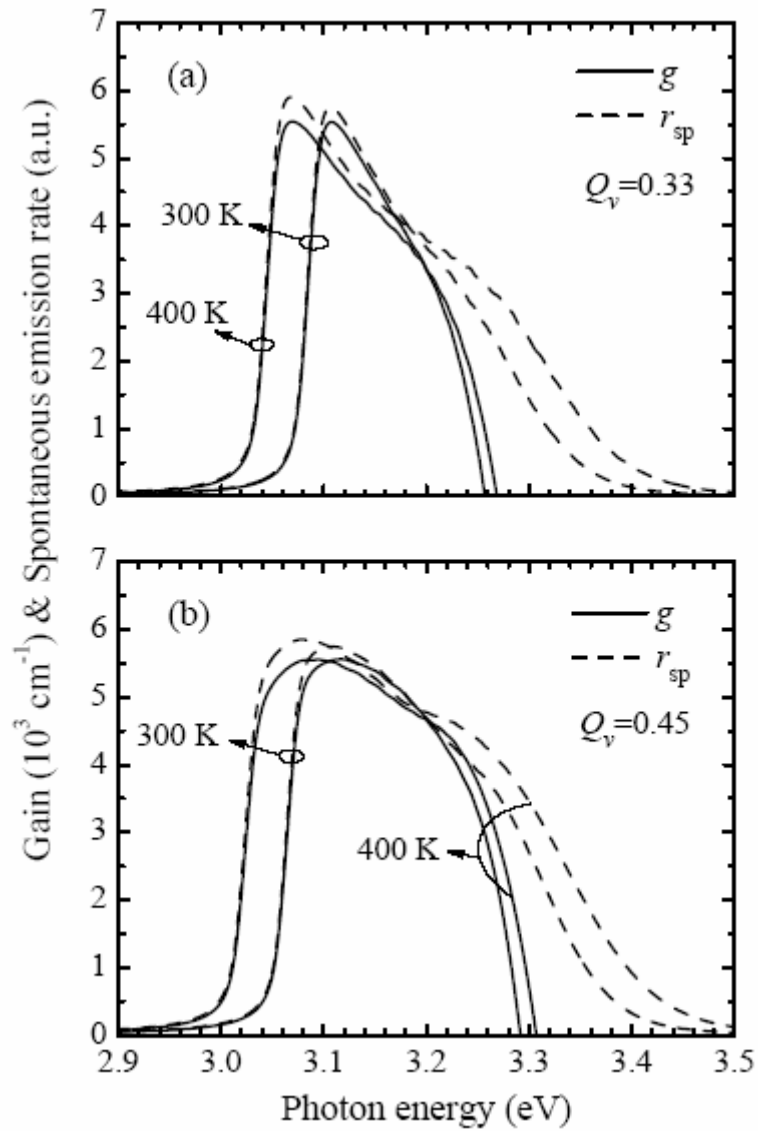


Fig. 3.10 The spectra of the gain g and the spontaneous emission rate r_{sp} at two different temperatures $T = 300$ and 400 K for 3.6 nm $\text{In}_{0.2}\text{Ga}_{0.8}\text{N}/\text{GaN}$ single-QW LDs at threshold with (a) $Q_v = 0.33$ and (b) $Q_v = 0.45$.

for a higher T and that the density of states around the quasi-bound subband edge is much larger than that of the bound subband. As a result, the electron density in the bound subband at threshold decreases for the shallow QW as T rises. However, the increase of the J_{bb} with rising T for the deep QW is due to the gain spectrum broadening that requires a high carrier density at threshold. It is noticed that for $Q_v = 0.45$ the J_{cb} becomes dominant over the J_{bb} as $T > 320$ K, implying that the optical property of the shallow QWs is no longer of pure two-dimensional nature. For deep QWs, the spillover is not serious in the range of $T = 300 \sim 400$ K.

In this study, we have taken the valence-band partition ratio Q_v as a variable parameter because of lack of a compelling value for this parameter. However, in the true case, Q_v must be fixed. It may be 0.33, or 0.45, or more probably another value. Recent published works have come to an agreement that the value of Q_v is small (close to 0.3).[85,86] Even for the small value, the spillover effect is not negligible on the threshold current. Nevertheless, regardless of the value of Q_v , our present work has introduced the important concept of carrier spillover, applicable not only to the nitride LDs but also to other kinds of LDs such as short-wavelength AlGaInP/GaAs LDs.

We have presented the calculated results by assuming quasi-equilibrium for electrons in the conduction band and for holes in the valence band. This means that our calculations are applicable to the case at and below threshold. Above threshold, the high interband transition rate makes the assumption of quasi-equilibrium no longer the case. It causes the spectral hole burning of the distribution function, which may have a reduction of the electron population in the bound subbands and meanwhile an increase of the population in the continuous subbands. Consequently, we expect a sublinear L-I relation above threshold.

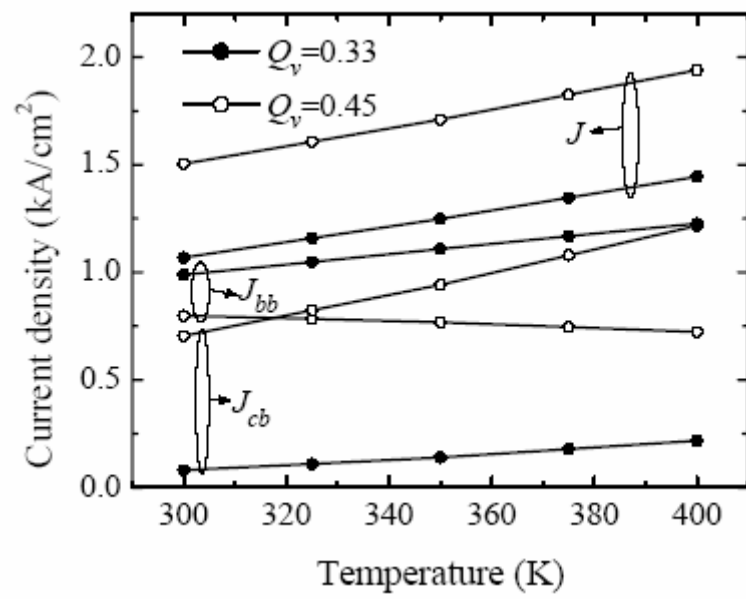


Fig. 3.11 The current densities J , J_{bb} , and J_{cb} at threshold as functions of temperature T for the 3.6 nm $\text{In}_{0.2}\text{Ga}_{0.8}/\text{GaN}$ single-QW LDs with $Q_v = 0.33$ and 0.45.

3.2.2 Doped Structure

In this section we present and discuss the calculated results of the spontaneous emission spectra and the current densities for modulation-doped $\text{In}_{0.2}\text{Ga}_{0.8}\text{N}/\text{GaN}$ QW lasers at threshold. The EBL is an $\text{Al}_{0.2}\text{Ga}_{0.8}\text{N}$ layer. The widths of the QW and the EBL are fixed at 3.6 nm and 20 nm, respectively, for all structures. For the double-QW structure, a 6 nm GaN barrier is inserted between the wells. All the values of material parameters used in our calculation have been mentioned previously.

Figure 3.12 shows the spectra of the total spontaneous emission rate r_{sp} and one of its components, $r_{\text{sp},cb}$, at threshold for single-QW structures with various doping levels, assuming $Q_v = 0.33$ in panel (a) and $Q_v = 0.45$ in panel (b). Because the valence subbands have very high densities of states, all the holes almost lie at the bottom of the well. This leads to a negligibly small amount of holes spilling over from the well. Hence, it is found from our calculated results that the bc and cc transitions are negligible compared with the bb and cb transitions. This permits us to write $r_{\text{sp}} \approx r_{\text{sp},bb} + r_{\text{sp},cb}$. Therefore, henceforth we will not present the calculated results concerning transitions involving the continuous valence subbands. As shown in Fig. 3.12, the shapes of r_{sp} are broadened because of the appearance of $r_{\text{sp},cb}$. This phase space filling effect was observed in a recent experimental work for LEDs, as shown in Fig. 3.13.[87] The shapes of r_{sp} are broader for $Q_v = 0.45$ than those for $Q_v = 0.33$ due to the larger contribution of $r_{\text{sp},cb}$ for $Q_v = 0.45$. For a shallower electron QW, the bound subband is closer to the continuous subbands. Therefore, there are more electrons spilling to the continuous subbands, resulting in the larger $r_{\text{sp},cb}$.

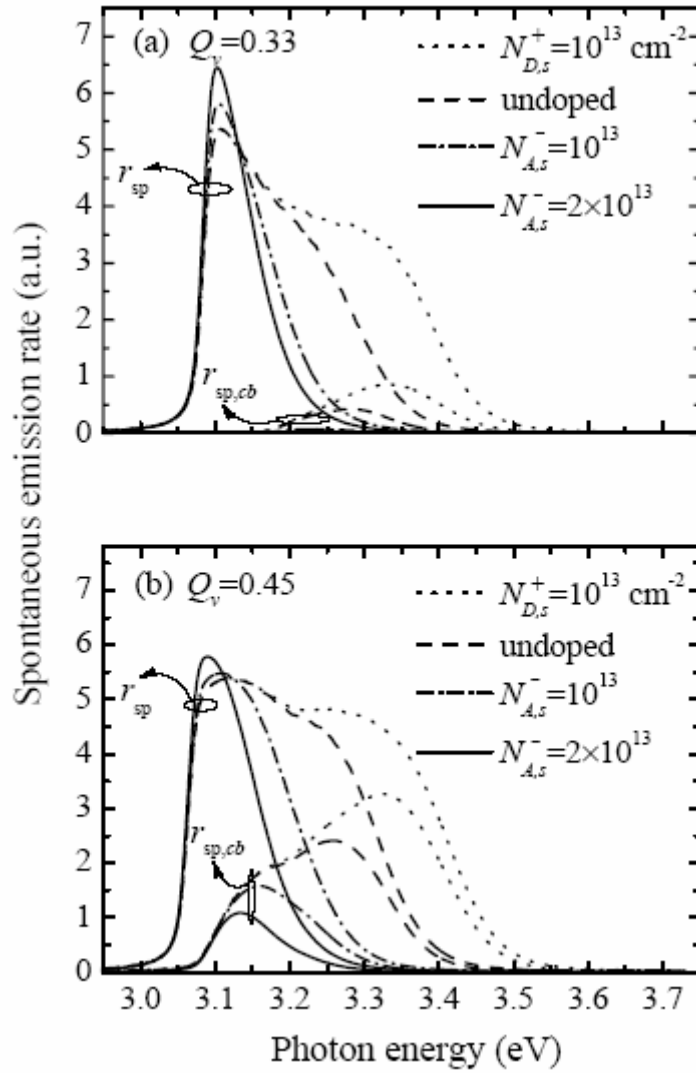


Fig. 3.12 The spectra of the total spontaneous emission rate r_{sp} and one of its components, $r_{sp,cb}$, at threshold for 3.6 nm $\text{In}_{0.2}\text{Ga}_{0.8}\text{N}/\text{GaN}$ single-QW LDs with various doping levels for $Q_v = 0.33$ in panel (a) and $Q_v = 0.45$ in panel (b). The $N_{D,s}^+$ and $N_{A,s}^-$ are the sheet concentrations of ionized donors and acceptors, respectively.

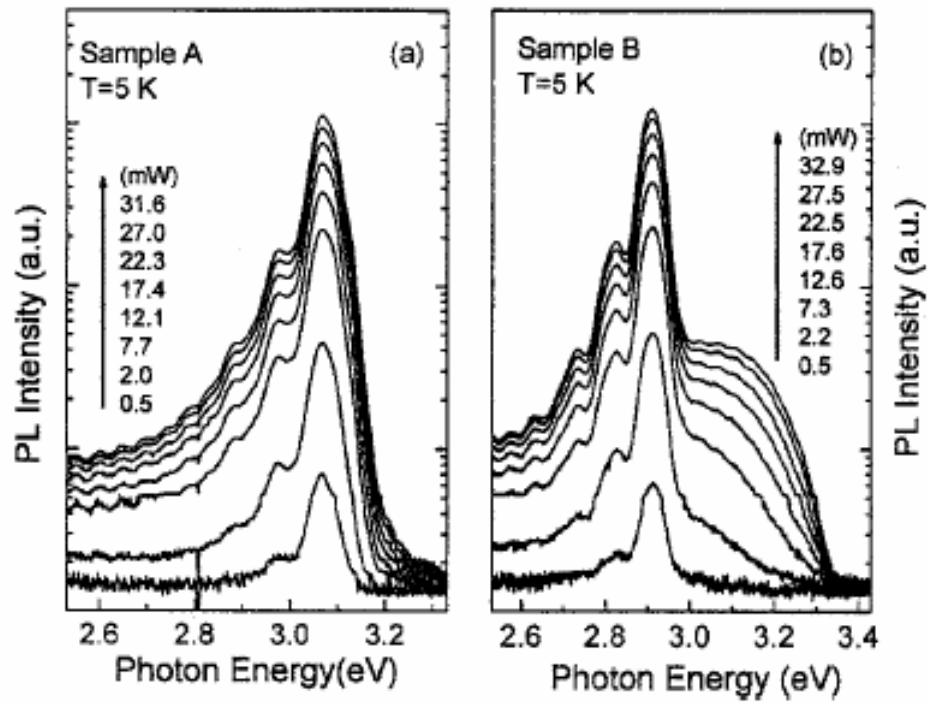


Fig. 3.13 Excitation power dependent PL spectra of InGaN/GaN QW LEDs at 5 K (a) for an undoped structure and (b) for the structure doped with Si at 10^{18} cm^{-3} . [87]

It is noticed that the LDs with p -type doping have smaller $r_{sp,cb}$ at threshold than the undoped one, while the one with n -type doping has a larger $r_{sp,cb}$. This gives rise to the narrowing of r_{sp} for p -type doping and the broadening of r_{sp} for n -type doping, as shown in Fig. 3.12 (a) and (b). As expected, the p -type doping alleviates the electron spillover while the n -type doping worsens it. To further understand the dependence of electron spillover on the doping level and species, we appeal to the diagram in Fig. 3.14, where there are schematically the conduction and the valence bands together with the Fermi level F , and the quasi-Fermi levels F_c and F_v at threshold. The levels F , F_c , and F_v lie at upper positions for n -type doping than for the undoped, while for p -type doping the levels lie at lower positions, as illustrated in Fig. 3.14. Furthermore, because of the large asymmetry in density of states between the conduction and the valence bands, the quasi-Fermi level F_c is much more sensitive to the doping level than F_v . For n -type doping, the high position of F_c implies serious electron spillover at threshold which causes the broadening of r_{sp} , as has been shown in Fig. 3.12. On the contrary, the p -type doping has a lower F_c and hence can diminish the electron spillover. This can also reduce the thermionic emission current leaking across the EBL. Besides, it is difficult for the p -type doping to cause the hole spillover because of the large density of states of the valence bands. As the spillover becomes negligibly small, further increasing the p -type doping level will not be a benefit, but causes an increase in the spontaneous emission rate at threshold. This is reflected by the increase of r_{sp} at energy about the main peak with the p -type doping level, as shown in Fig. 3.12.

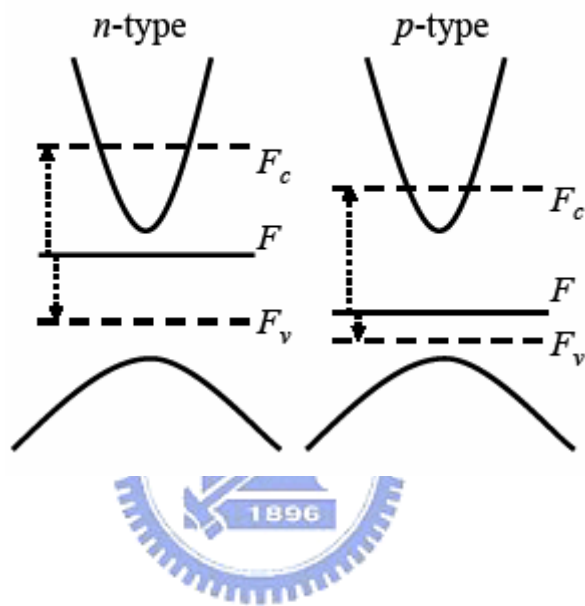


Fig. 3.14 Schematic diagrams of the conduction and the valence bands together with the Fermi level F , and the quasi-Fermi levels F_c and F_v at threshold for the cases of n -type doping (the left) and p -type doping (the right).

Figure 3.15 shows the current densities J , J_{bb} , and J_0 at threshold versus the ionized dopant concentration for single-QW structures, similarly assuming the partition ratio $Q_v = 0.33$ in panel (a) and $Q_v = 0.45$ in panel (b). Here, for comparison, we include the current density J_0 which is calculated with all the carriers occupying the bound subbands. The difference $J - J_{bb} \simeq J_{cb}$ can reveal the influence of electron spillover on the total current density J at threshold. As expected, both J_{bb} and J_{cb} decrease with the p -type doping level but increase with the n -type doping level. As the p -type doping level is very high (about $1.5 \times 10^{13} \text{ cm}^{-2}$ for $Q_v = 0.33$ and about $2 \times 10^{13} \text{ cm}^{-2}$ for $Q_v = 0.45$), the benefit from the p -type doping vanishes and the current density J seems to approach an asymptotic value. In practice, such high p -type doping is difficult to achieve in the nitride compounds due to the large activation energy of acceptors.

It is noticed that the current density J_0 behaves quite differently from J for $Q_v = 0.45$, implying that it is important to consider the electron spillover in calculation of the threshold current for a shallow QW. Peculiarly, the J_0 is almost fixed at a constant value ($\sim 1 \text{ kA/cm}^2$) in the whole range of n -type doping level and also for p -type doping level less than $7 \times 10^{12} \text{ cm}^{-2}$. This can be explained from Eq. (2.20), where we find $m_t(z)$ a function of z . It has a smaller value inside the QW region than outside. With k_t increasing, the effective potential energy V_{eff} increases more inside the QW region than outside. For k_t beyond a certain critical value k_c , the V_{eff} forms a barrier profile with a higher effective potential energy inside the QW region than outside. In this case, the wave function is leaky in nature and has a nearly zero overlap with the wave function of the valence band state. Thus, the electrons at states of $k_t > k_c$ have nothing to do with the interband process. This explains the peculiar behavior of J_0 . This behavior is particularly obvious for a shallow QW (for instance, $Q_v = 0.45$) because of the small value of k_c . In the practical

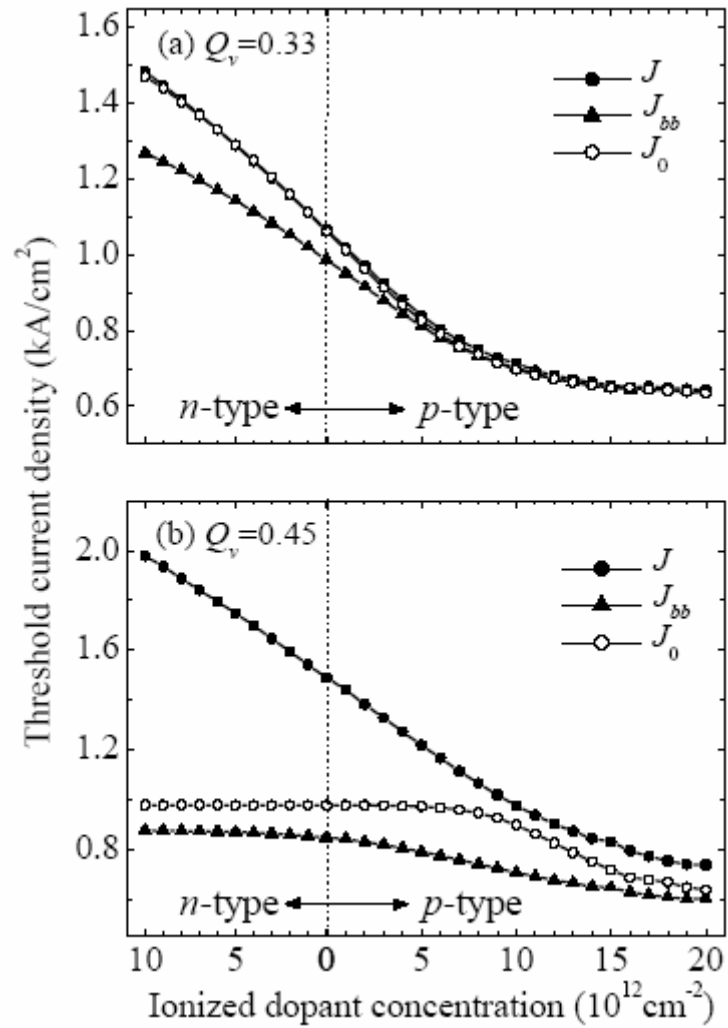


Fig. 3.15 The current densities, J , J_{bb} , and J_0 , at threshold versus the ionized dopant concentration for 3.6 nm $\text{In}_{0.2}\text{Ga}_{0.8}\text{N}/\text{GaN}$ single-QW LDs, assuming $Q_v = 0.33$ in panel (a) and $Q_v = 0.45$ in panel (b). The J is the total threshold current density, the J_{bb} is the current density due to the bound-to-bound process, and the J_0 is the threshold current density calculated without considering the carrier spillover.

case, the threshold current density J varies with the n -type doping level because of the electron spillover to the continuous subbands.

Until now the calculated results have been for LDs with a cavity loss of 60 cm^{-1} . For a higher cavity loss, it requires a higher carrier density in the QW to reach threshold. In this case, the problem of electron spillover becomes more important. Figure 3.16 shows the threshold current density J as a function of the cavity loss α of single-QW LDs with different doping levels for (a) $Q_v = 0.33$ and (b) $Q_v = 0.45$. As expected, the J increases with α . The increase is particularly obvious for the case of n -type doping (as well as for the case of the undoped). Moreover, most of the curves are somewhat superlinear because the spillover electrons play a more and more important role with α increasing in the interband process. As we have learned, the p -type doping can significantly diminish the electron spillover. This is further evidenced by the fact in Fig. 3.16 that the separation between the curve for the undoped and the one for $N_{A,s}^- = 2 \times 10^{13} \text{ cm}^{-2}$ increases with the cavity loss α . By p -type doping, the threshold current density for $\alpha = 80 \text{ cm}^{-1}$ can be reduced by a factor of ~ 2 for $Q_v = 0.33$ ($J = 1.8 \text{ kA/cm}^2$ for the undoped and $J = 0.8 \text{ kA/cm}^2$ for $N_{A,s}^- = 2 \times 10^{13} \text{ cm}^{-2}$) and by a factor of ~ 1.5 for $Q_v = 0.45$ ($J = 2.7 \text{ kA/cm}^2$ for the undoped and $J = 1.8 \text{ kA/cm}^2$ for $N_{A,s}^- = 2 \times 10^{13} \text{ cm}^{-2}$). For the large cavity loss, the reduction in J is more considerable for $Q_v = 0.33$ than for $Q_v = 0.45$ because the electron spillover can almost be eliminated for the deep well by the p -type doping but is not negligible for the shallow well. This reflects the fact that with the p -type doping $N_{A,s}^- = 2 \times 10^{13} \text{ cm}^{-2}$, the $J-\alpha$ curve is almost linear for $Q_v = 0.33$ but obviously nonlinear for $Q_v = 0.45$.

The temperature characteristic is also an important issue for lasers. We plot the threshold current density J versus temperature T with various doping levels for

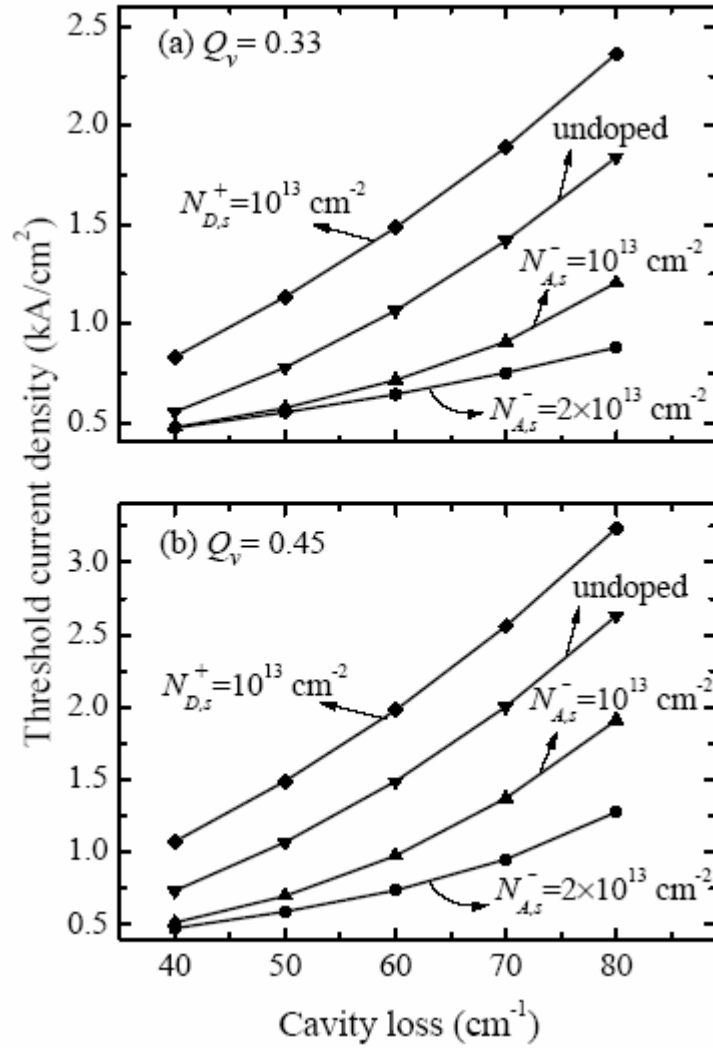


Fig. 3.16 The current density, J , at threshold as functions of the cavity loss for 3.6 nm $\text{In}_{0.2}\text{Ga}_{0.8}\text{N}/\text{GaN}$ single-QW LDs with various doping levels for $Q_v = 0.33$ in panel (a) and $Q_v = 0.45$ in panel (b).

single-QW LDs in Fig. 3.17, assuming $Q_v = 0.33$ in panel (a) and $Q_v = 0.45$ in panel (b). It can be seen that the $J-T$ curves are linear and almost parallel to each other. It seems that introducing dopants to the active region does not significantly influence the temperature characteristic. However, the situation will not be the case if the electron leakage into the p -type cladding layer is considered. As has been pointed out, such leakage is serious for n -type doping[88] and further deteriorates at high temperature. The p -type doping can be used to reduce the electron leakage into the p -type cladding layer as well as the electron spillover.

In Fig. 3.18, the current densities J , J_{bb} , and J_0 at threshold of double-QW LDs are plotted as functions of the ionized dopant concentration for (a) $Q_v = 0.33$ and (b) $Q_v = 0.45$. Similar to the case in Fig. 3.15, the J_{cb} ($\approx J - J_{bb}$) and the amount of spillover electrons increase with the n -type doping level while decrease with the increase of p -type doping level. Compared with the case of single-QW LDs, the electron spillover is smaller for the double-QW LDs because of the smaller carrier density required for threshold. As a result, the J_{bb} has a minimum at a certain p -type doping level and increases as the p -type doping level further increases. In this situation, the drawback of increasing electron-hole recombination goes beyond the advantage of reducing electron spillover. The J_{bb} reaches the minimum at about $2.5 \times 10^{12} \text{ cm}^{-2}$ for $Q_v = 0.33$ and at about $5 \times 10^{12} \text{ cm}^{-2}$ for $Q_v = 0.45$, where the threshold current density J reaches or approaches the minimum value.

Comparing the threshold current densities in Fig. 3.15 and those in Fig. 3.18, one can see that the favorite structure for the lowest J is the single-QW one with heavily p -type doping for both $Q_v = 0.33$ and $Q_v = 0.45$. However, in reality, the high activation energy of acceptors in the wide-gap nitride compounds may make such optimization difficult to achieve. If the heavily p -type doping could not be achieved, the double-QW structure with a lower p -type dopant concentration is a good choice. The optimized p -type doping level is

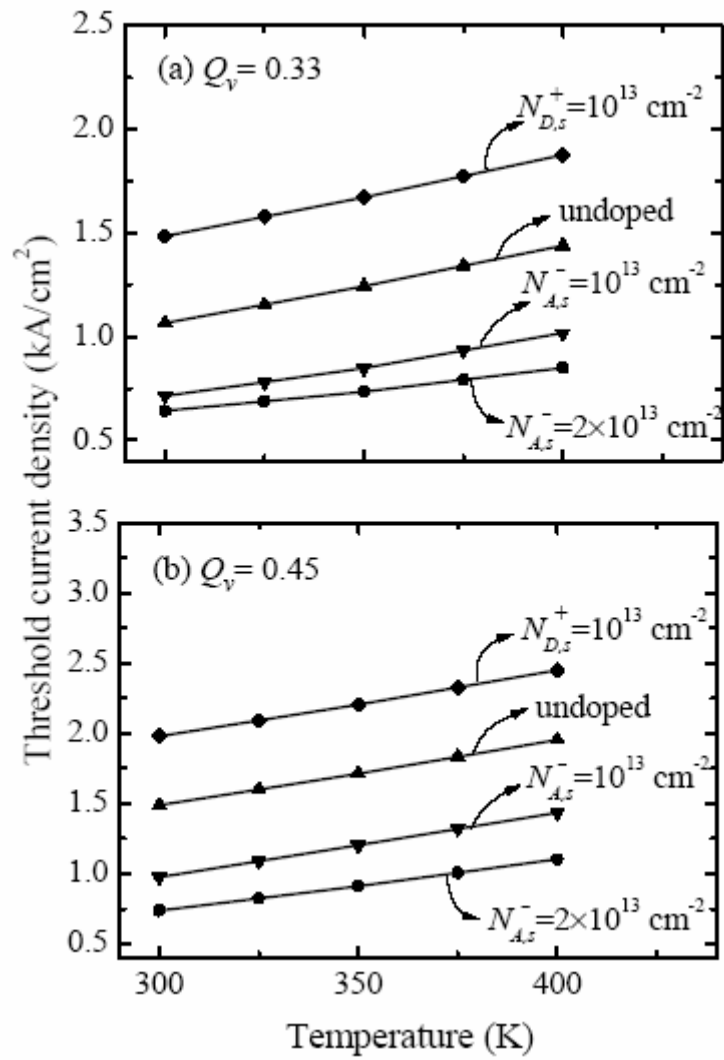


Fig. 3.17 The current density, J , at threshold versus temperature for 3.6 nm $\text{In}_{0.2}\text{Ga}_{0.8}\text{N}/\text{GaN}$ single-QW LDs with various doping levels for $Q_v = 0.33$ in panel (a) and $Q_v = 0.45$ in panel (b).

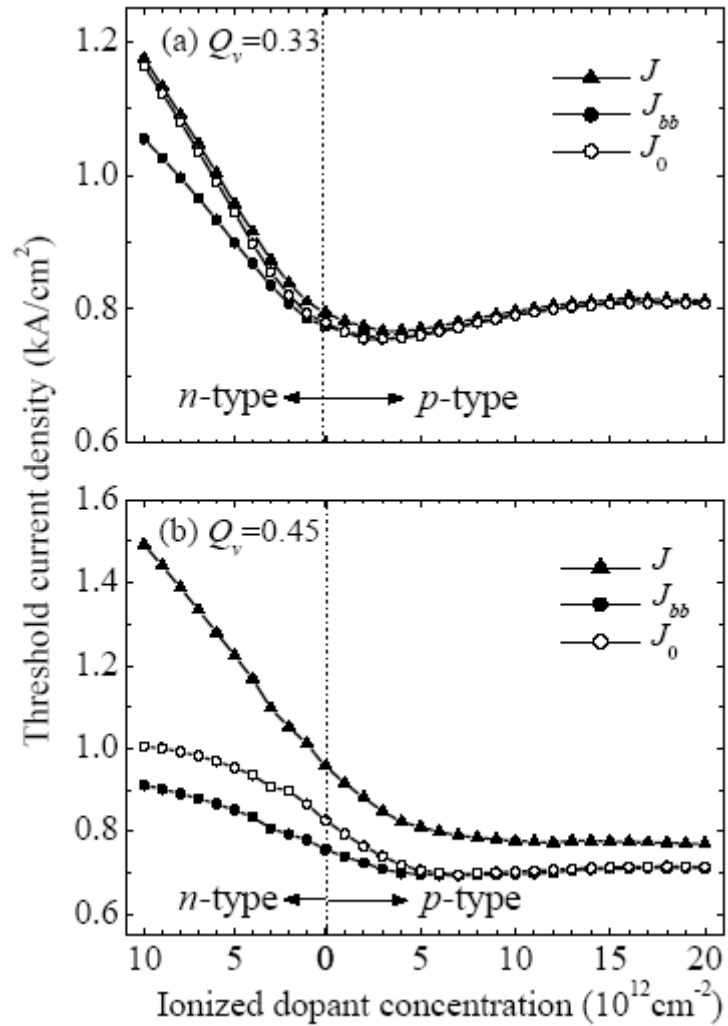


Fig. 3.18 The current densities, J , J_{bb} , and J_0 , at threshold versus the ionized dopant concentration for 3.6 nm $\text{In}_{0.2}\text{Ga}_{0.8}\text{N}$ -60 nm GaN double-QW LEDs, assuming $Q_v = 0.33$ in panel (a) and $Q_v = 0.45$ in panel (b).

about $2.5 \times 10^{12} \text{ cm}^{-2}$ ($\sim 6.9 \times 10^{18} \text{ cm}^{-3}$) for $Q_v = 0.33$ and about $7 \times 10^{12} \text{ cm}^{-2}$ ($\sim 1.9 \times 10^{19} \text{ cm}^{-3}$) for $Q_v = 0.45$. The ionization efficiency depends on the doping level and is still unclear for *p*-type modulation-doped InGaN/GaN QWs. From the experimental work with structures similar to those used here, a uniformly doped 4 nm-In_{0.2}Ga_{0.8}N/4 nm-GaN superlattice with a Mg concentration of $3 \times 10^{19} \text{ cm}^{-3}$ has a spatially averaged hole concentration of about $2.6 \times 10^{19} \text{ cm}^{-3}$. [89] Since the main contribution of released holes is from the acceptors in the GaN barriers, the ionization efficiency of the modulation doping is about 100%. Thus, the optimized carrier concentrations mentioned above are possible to be achieved.

3.3 Summary

The influences of spillover effects on radiative current density, gain spectra, and spontaneous emission spectra in InGaN/GaN QW LDs have been theoretically studied in detail. To this end, the continuous subbands above the barriers in energy are considered for the spillover electrons. It has been shown that there are obvious differences in the radiative current densities and gain spectra between the cases with and without considering the spillover effect. It is shown that the spillover effects are important, especially to shallow QWs. The participation of spillover electrons in interband transitions causes spectral broadening of the gain and the spontaneous emission, and hence increases the threshold current. Such effects become more serious as the cavity loss increases or the temperature rises. To reduce the spillover, one can employ a multi-QW structure for the LDs.

Besides, the radiative current densities and the spontaneous emission spectra in modulation-doped InGaN/GaN QW LDs have been investigated with the electron spillover above the barriers considered. The calculated results indicate that the consideration of

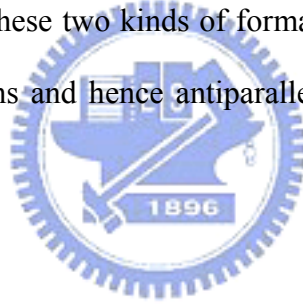
electron spillover is important in studying the effects of modulation doping to the active region especially for shallow electron QW structures. When the influence of introducing impurities on crystal quality is ignored, the threshold current density can be significantly reduced by p -type doping but increased by n -type doping which is conventionally used. The benefit from the p -type doping is particularly obvious for a large cavity loss. An optimized low threshold current can be achieved for single-QW LDs with heavily p -type doping. For double-QW LDs, slightly p -type doping is required to obtain low threshold current.



Chapter 4

Vertical Resistivity of the Superlattice

We consider a wurtzite p -type $\text{Al}_x\text{Ga}_{1-x}\text{N}/\text{GaN}$ SL sandwiched by two strain-free GaN bulks grown along the crystallographic c -axis which is defined as the z axis. The GaN bulk at the bottom side is regarded as the substrate and contacted to the cathode whereas the other is contacted to the anode. In the GaN, the top position of the $\{0001\}$ bilayer could be located by either Ga or N atoms. By convention, the basal surface formed by Ga (N) atoms is defined as Ga-face (N-face). These two kinds of formations result in antiparallel directions of crystallographic polarizations and hence antiparallel piezoelectric fields in the strained layers.[90,91]



4.1 Some assumptions and definitions

Here, we consider the piezoelectric field in the tensile strained AlGa N layer which is parallel (antiparallel) to the z axis in the case of Ga-face (N-face) with a magnitude of [50]

$$F_{\text{pz}} = \left| \frac{2d_{31}}{\varepsilon} (C_{11} + C_{12} - \frac{2C_{13}^2}{C_{33}}) \varepsilon_{\parallel} \right|, \quad (3.1)$$

where d_{31} is the piezoelectric constant, ε is the static dielectric constant, C_{ij} are the elastic stiffness constants, and ε_{\parallel} is the in-plane component of the strain tensor. The values of parameters related to F_{pz} are all given in [8].

The whole structure is uniformly Mg-doped at $5 \times 10^{19} \text{ cm}^{-3}$, and the acceptor ionization

energy is assumed to be $170 + 740x$ meV in $\text{Al}_x\text{Ga}_{1-x}\text{N}$ layer.[92] The band profile of the whole structure is calculated self-consistently by the electric continuity equation and the one-dimensional Poisson equation in an iterative scheme. The bandgap of $\text{Al}_x\text{Ga}_{1-x}\text{N}$ is determined by $E_g(x) = [xE_{g,\text{AlN}} + (1-x)E_{g,\text{GaN}} - 0.7x(1-x)]$ eV, where $E_{g,\text{AlN}}$ and $E_{g,\text{GaN}}$ are the bandgaps of AlN and GaN, respectively.[8] The Varshni relation is used for the temperature dependence of the band gap. [8] The valence band offset between GaN and $\text{Al}_x\text{Ga}_{1-x}\text{N}$ is given by $\Delta E_v = 0.49[E_g(x) - E_{g,\text{GaN}}]$ eV, yielding $\Delta E_v = 0.2$ eV for $x = 0.2$. [93] The dielectric constant is determined by $\epsilon_r(x) = 8.9 - 0.4x$. [94] For the free carrier distribution, we consider the quantization effect through the Luttinger-Kohn Hamiltonian taking into account the coupling of the six hole bands and the strain effect, as has been described in section 2.2. The finite difference method with the Dirichlet boundary condition at both edges of the whole system is used. The Jacobian-Newton iteration, which contains an outer-loop Poisson equation by the Jacobian method and an inner-loop Poisson equation by Newton method, is performed to prevent numerical instability, as described in section 2.5.3.[67] All the material parameters required in the calculation are given by [8] except those mentioned previously.

4.2 Result and Discussion

We study the variation of the vertical resistance with the barrier width for p -type $\text{Al}_{0.11}\text{Ga}_{0.89}\text{N}/\text{GaN}$ superlattice structures having either Ga-face or N-face polarity at room temperature (300 K) and higher (400 K). Three structures with different barrier widths (2, 4, and 6 nm) are considered while their well widths are set the same at 2 nm. We do not consider the cases of barrier width larger than 6 nm since the thermionic emission model may be no longer appropriate due to the nonnegligible scattering effect. The average vertical

resistivity of the SLs can be obtained by V/Jt , where J is the current density under bias voltage V across the SLs with total thickness t . The thicknesses of the SLs t are all fixed at 118 nm, here.

Figure 4.1 shows the valence band diagrams of the three structures under the current density at 3.6 kA/cm² and the temperature at 300 K for the polarity of Ga-face in panel (a) and N-face in panel (b). As can be seen, the voltage bias across the whole structure decreases while the barrier width increases. This is because the holes pass (by thermionic emission and F-N tunneling) through a smaller number of barriers for the structure with wider barriers. The barriers are the bottleneck for the hole flow and thus reducing the number of barriers can significantly reduce the voltage bias for a constant current. However, it is also worthy of note that the voltage bias across each barrier increases with the barrier width. As shown in Fig. 4.1, the total biased voltage across the whole SL is more insensitive to the barrier width variation when the barriers are thicker. For instance, the biased voltage decreases less as the barrier width increases from 4 to 6 nm than as the width increases from 2 to 4 nm. Hence, the biased voltage will be close to a lower bound as the barrier width increase. However, we have excluded the scattering effect in the barrier regions in our calculation. This may underestimate the biased voltage across the SL with wide barriers. A more accurate model considering the scattering effect should be developed for the case of wider barriers in the future. Comparing Fig. 4.1 (a) with (b), the bias voltage across the whole superlattice is larger for the case of N-face polarity than that of Ga-face polarity. This is because the piezoelectric field in the superlattice with N-face polarity is aligned to the external electric field, leading to the increasing of the barrier height. Thus, under the same current density, larger biased voltage will result for the SL with N-face polarity.

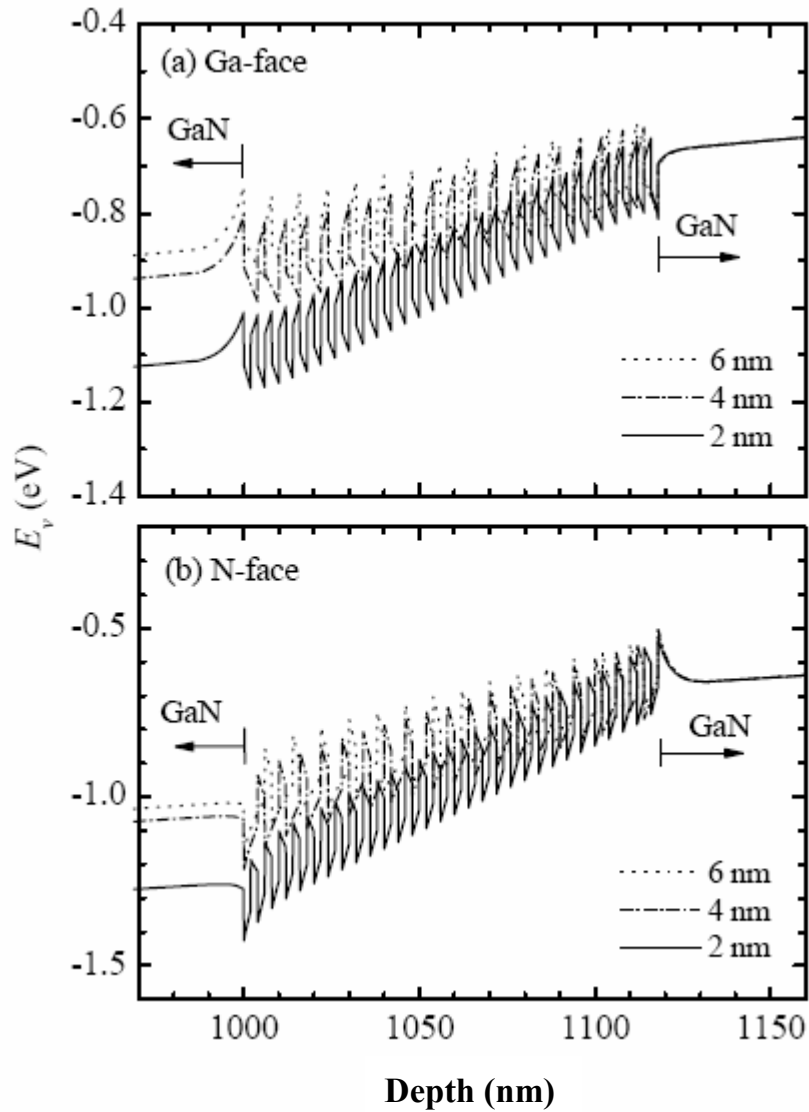


Fig. 4.1 Valence band profile of the three superlattices constructed with equal well width (2 nm) but different barrier widths (2, 4 and 6 nm) under the same current density 3.6 kA/cm² for (a) Ga-face and (b) N-face polarities.

Figure 4.2 (a) and (b) show the proportion of the tunneling current density to the total current density at each barrier under the same conditions as in Fig. 4.2 (a) and (b), respectively. It should be noted that the total current density is the tunneling current density plus the thermionic emission current density. As can be seen in Fig. 4.2 (a) and (b), the dominant mechanism for holes passing through the barriers is the F-N tunneling. One can also notice that the proportion does not increase as the barrier width decreases. This is because such proportion is affected not only by the barrier width, which influences the tunneling probability $P(E_{\perp})$, but also by the energy range in which the holes pass through by F-N tunneling (i.e., the integration limit from E_2 to E_1). The mentioned two factors have opposite contribution to $J_{\text{tunneling}}$. So, even though the 2 nm barriers have the largest tunneling probability among the three structures, the smallest energy range for holes passing by F-N tunneling makes the proportion of tunneling current the smallest in Fig. 4.2 (a). Similar competition is also observed in Fig. 4.2 (b). One may also find that the proportion for each structure decreases to a minimum and then goes up as the barrier index increases. This is because the amount of space charges is large around the edges (due to either ionized acceptors at one side or accumulated holes at the other side), causing large band bending and thus large energy range for F-N tunneling. Comparing Fig. 4.2 (a) with (b), there are larger amounts of holes passing by F-N tunneling in the structure with N-face polarity than with Ga-face. This is because the parallel external electric field makes the band bending of the barriers more serious in the case of N-face polarity.

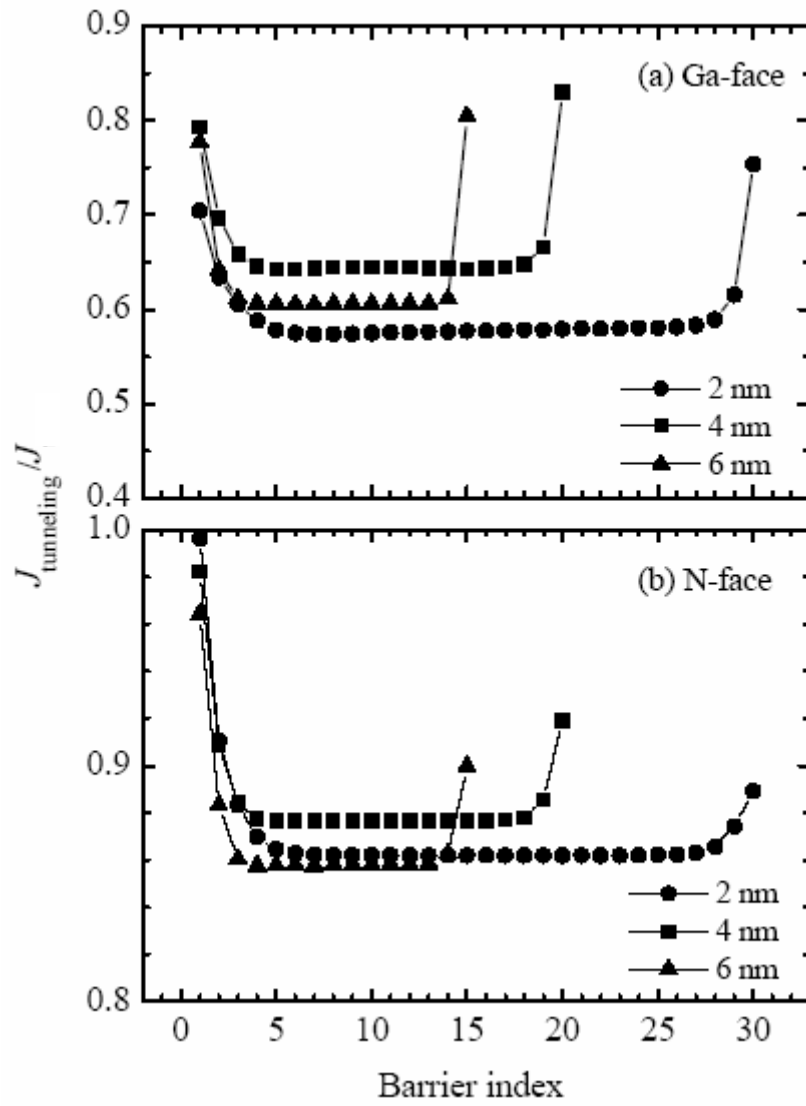


Fig. 4.2 The proportion of the tunneling current density $J_{\text{tunneling}}$ to the total current density flowing through each barrier under the same condition in Fig. 2 for (a) Ga-face and (b) N-face polarities.

Figure 4.3 and 4.4 are the calculation results for the cases similar to Fig. 4.1 and 4.2, respectively, except the temperature at 400 K. Comparing the results between Fig. 4.1 and 4.3, we find that the biased voltage across the whole SL is smaller for higher temperature. The main reason is that there are more energetic holes at higher temperature and, therefore, a smaller biased voltage across each barrier is required for a constant current density. Also, the variation of the biased voltage with the barrier width is smaller at higher temperature. In spite of this, the SL with wider barriers is still more preferable for optical confinement. Besides, comparing the results between Fig. 4.2 and 4.4, we find that the contribution of $J_{\text{thermionic}}$ becomes more important at higher temperature and $J_{\text{thermionic}}$ can even become dominant over the tunneling current for the SL with 2 and 6 nm barrier width in the case of Ga-face polarity, except at the edges of the SLs. This is additional evidence that the biased voltage is more insensitive to the barrier width at higher temperature.

Figure 4.5 shows the average vertical resistivities of the three SLs having different barrier widths (2, 4, and 6 nm) at 300 K and 400K. At 300 K (400 K), when the width of the barrier increases from 2 nm to 6 nm, the resistivities are reduced by 54.7 % (48.9 %) and 48.2 % (50.1 %) for Ga- and N-face, respectively. Therefore, about a 50% decrement in the vertical resistivity can be expected when the barrier width increases from 2 nm to 6 nm.

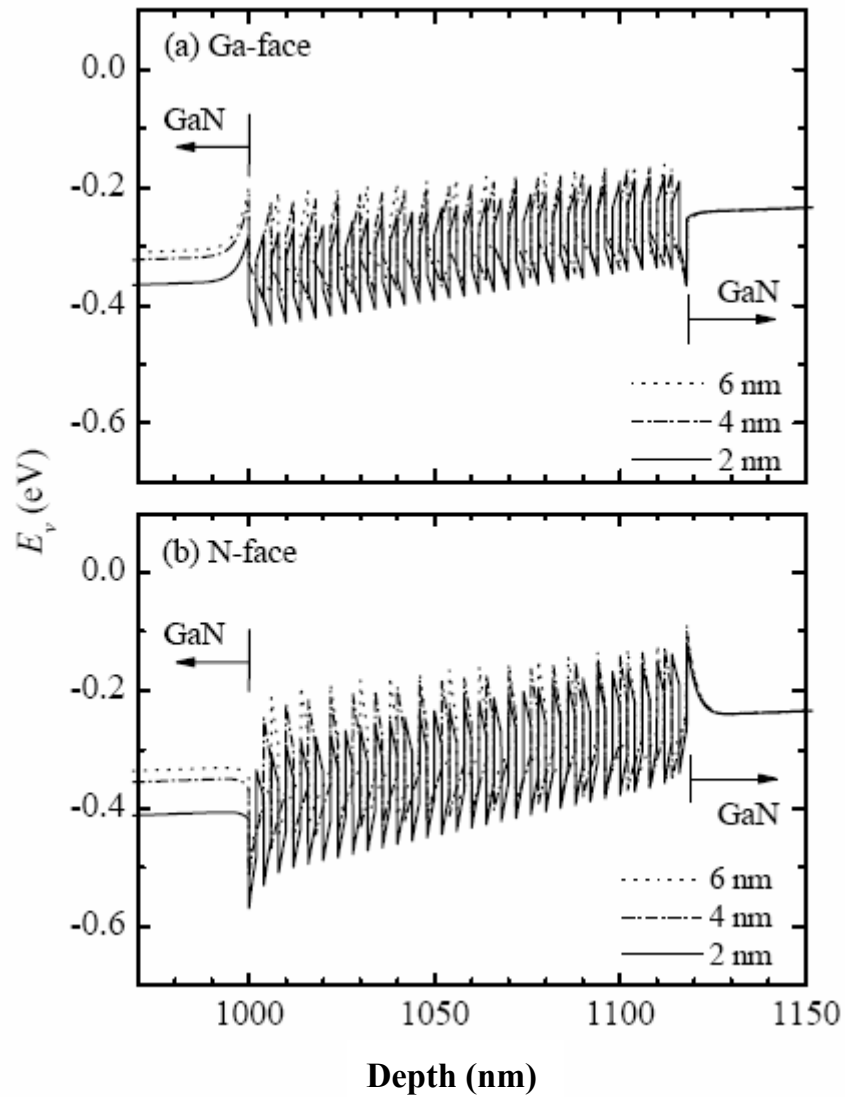


Fig. 4.3 Valence band profile of the three superlattices constructed with equal well width (2 nm) but different barrier widths (2, 4 and 6 nm) under the same current density 3.6 kA/cm^2 for (a) Ga-face and (b) N-face polarities at 400 K.

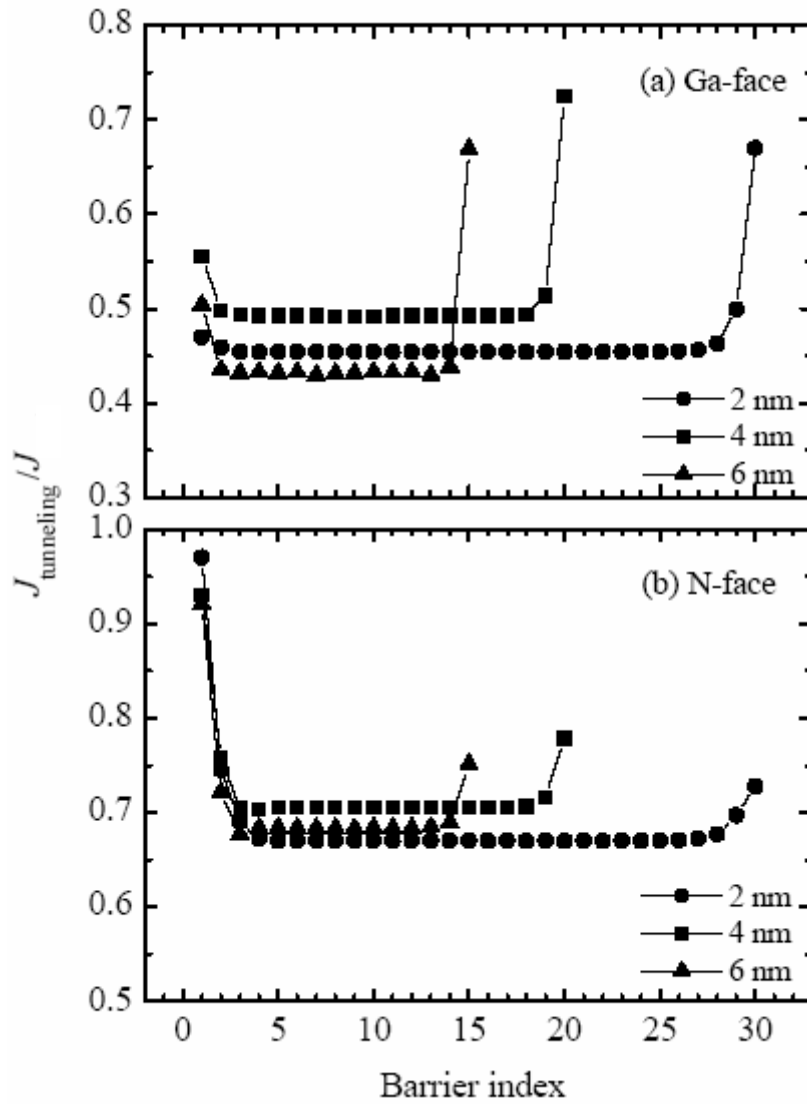


Fig. 4.4 The proportion of the tunneling current density $J_{\text{tunneling}}$ to the total current density flowing through each barrier under the same condition in Fig. 2 for (a) Ga-face and (b) N-face polarities at 400 K.

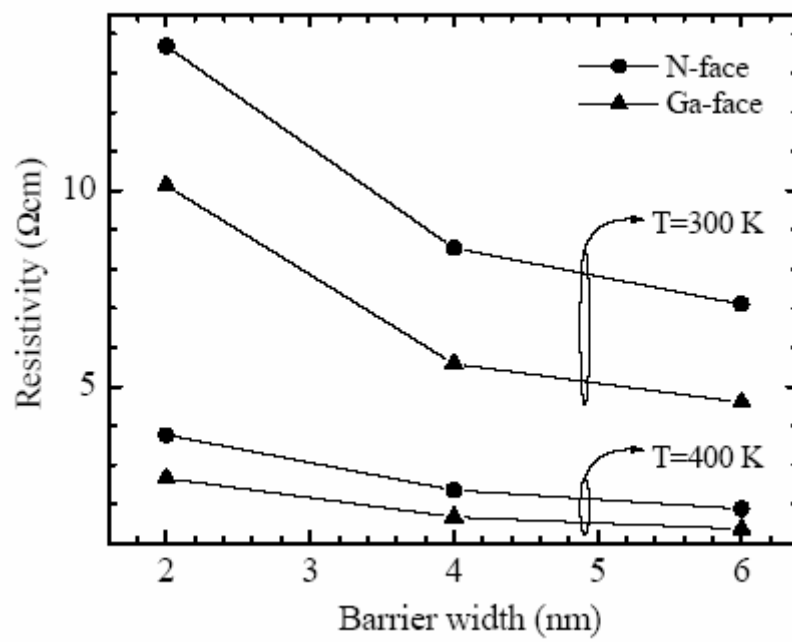
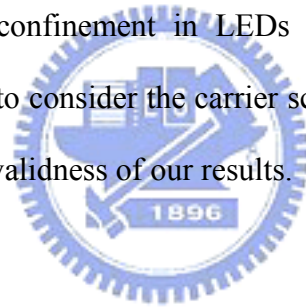


Fig. 4.5 The average vertical resistivities of the three SLs having different barrier widths (2, 4, and 6 nm) at 300 K and 400K.

4.3 Summary

In this chapter, we have calculated and analyzed the band diagrams of *p*-type $\text{Al}_{0.2}\text{Ga}_{0.8}\text{N}/\text{GaN}$ superlattices with both Ga- and N-face polarities and the current density distribution during different mechanisms under constant total bias current at different temperature. Based on our model, we have found that the vertical resistance of the SL can be reduced by increasing the barrier width if it is thin enough. About 50% decrement in the vertical resistivity can be expected when the structure of the SL $\text{Al}_{0.11}\text{Ga}_{0.8}\text{N}(2\text{ nm})/\text{GaN}(2\text{ nm})$ changes to $\text{Al}_{0.11}\text{Ga}_{0.8}\text{N}(6\text{ nm})/\text{GaN}(2\text{ nm})$. This benefit remains even at high temperature. In addition to the low vertical resistivity, the SL with wider barriers is also preferable for better optical confinement in LEDs and LDs. For thick barriers, more accurate calculation is needed to consider the carrier scattering effect. Besides, experiments would be helpful to verify the validness of our results.



Chapter 5

Conclusion and Suggestion

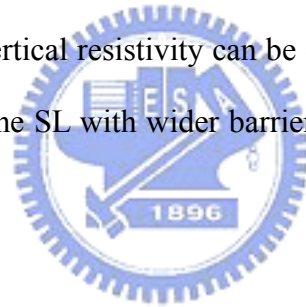
5.1 Conclusion

In order to optimize the InGaN/GaN QW LDs, we investigate the vertical resistivity in the p -type cladding layer composed of a AlGaIn/GaN short period SL and also the optical transition properties in the active region considering the spillover effects and the modulation-doping. The spillover effects in InGaIn/GaN QW LDs are studied through the continuous subbands above the barriers in energy. Their influences on radiative current density, gain spectra, and spontaneous emission spectra are discussed in detail. It is shown that there are obvious differences in the radiative current densities and gain spectra between the cases with and without considering the spillover effects. These effects play an important role in radiative current density and spectra of gain and spontaneous emission rate, especially for shallow QWs. The participation of spillover electrons in interband transitions causes spectra broadening of the gain and the spontaneous emission, and hence increases the threshold current. As the cavity loss or the temperature increases, such effects become even more serious. It is indicated that employing the multi-QW structure for the LDs can obviously reduce the influence of these effects.

The LD structures with modulation-doping around the InGaIn/GaN QWs are also investigated to further reduce the threshold current density. Both p - and n -type doping are studied. It is shown that the threshold current density is significantly reduced by p -type doping but increased by n -type doping which is conventionally used. The benefit from the p -type doping is particularly obvious for a large cavity loss. Our results show that the

optimized low threshold current can be achieved for single-QW LDs with heavily *p*-type doping. For double-QW LDs, only slightly *p*-type doping is required to obtain low threshold current.

In addition to the active region, we also studied the *p*-type cladding layer composed of a $\text{Al}_{0.2}\text{Ga}_{0.8}\text{N}/\text{GaN}$ SL. The band diagrams of such SL are calculated and analyzed under constant bias current at different temperature. The current density distribution during different mechanisms is presented. Based on our calculation model, it is found that the key factor resulting in the vertical resistance in short period SLs is the number of barriers. So, one can increase the barrier width to get smaller number of barriers and hence lower vertical resistance in short period SLs. When the structure of the SL $\text{Al}_{0.2}\text{Ga}_{0.8}\text{N}(2\text{ nm})/\text{GaN}(2\text{ nm})$ changes to $\text{Al}_{0.2}\text{Ga}_{0.8}\text{N}(6\text{ nm})/\text{GaN}(2\text{ nm})$ under the same total length, about 50% decrement in the vertical resistivity can be expected. This benefit remains even at high temperature. Besides, the SL with wider barriers is also preferable for better optical confinement in LEDs and LDs.



5.2 Suggestion for Future Work

In the conclusions, we reported that the employment of *p*-type modulation-doping can obviously reduce the threshold current density. However, one should be noticed that the influence of introducing impurities on crystal quality is ignored here. The investigations on the variation of crystal quality of InGaN/GaN QWs with *p*-type doping did not attract as much research interesting as *n*-type doping and are not yet complete. Due to the potential improvement in the InGaN/GaN QW LDs, we suggest there should be more experimental studies on the crystal quality of *p*-type modulation-doping InGaN/GaN QWs.

Once the spillover electrons are diminished by *p*-type modulation-doping, the barrier height of the AlGaIn EBL can be lowered or even totally removed. As is well known, the

EBL located next to the active region is one of the factors that lower the optical confinement. When the barrier height of the EBL is lower, the optical confinement factor will be increased, and this will further reduce the threshold carrier density. So, how much composition of Al is needed in the EBL after p -type modulation-doping in the active region is now an interesting issue for future theoretical and experimental works.

On the side of p -type SL cladding layer, we have reported the wider barriers are preferable to obtain a lower vertical resistance. However, our model does not include the carrier scattering effect above the barriers, which is important for the energetic carriers passing through the wide barriers by thermionic emission. This may probably make us underestimate the resistance for the SL with wide barriers. More accurate calculation is needed to consider the carrier scattering effect in the future work.

In addition to the electrical property, the optical confinement property of the SL is also an interesting issue. Since the wider barriers are preferable in obtaining higher optical confinement factor, one may wonder how large the barrier widths should be the optimized value not only for the low vertical resistance but also for the high optical confinement factor. Both experimental and theoretical works would be helpful to find the answer.

Reference

1. T. Yamaguchi, Y. Ueda, Y. Matsushita, K. Koga, and T. Niina, "RGB multi-color LED dot-matrix units and their application to large-size flat displays," *Optoelectron., Devices Technol.* **7**, 221 (1992).
2. W. Xie, D. C. Grillo, R. L. Gunshor, M. Kobayashi, H. Jeon, J. Ding, A. V. Nurmikko, G. C. Hua, and N. Otsuka, "Room temperature blue light emitting *p-n* diodes from Zn(S,Se)-based multiple quantum well structures," *Appl. Phys. Lett.* **60**, 1999 (1992).
3. D. B. Eason, Z. Yu, W. C. Hughes, W. H. Roland, C. Boney, J. W. Cook, Jr., J. F. Schetzina, G. Cantwell, and W. C. Harasch, "High-brightness blue and green light-emitting diodes," *Appl. Phys. Lett.* **66**, 115 (1995).
4. J. I. Pankove, E. A. Miller, and J. E. Berkeyheiser, "Electroluminescence in GaN," *J. Lumin.* **4**, 63 (1971).
5. S. Nakamura, M. Senoh, S. Nagahama, N. Iwasa, T. Yamada, T. Matsushita, H. Kiyoku, and Y. Sugimoto, "InGaN-based multi-quantum-well-structure laser diodes," *Jpn. J. Appl. Phys.*, **35**, L74 (1996).
6. S. Nakamura, M. Senoh, S. Nagahama, N. Iwasa, T. Yamada, T. Matsushita, H. Kiyoku, and Y. Sugimoto, "Characteristics of InGaN multi-quantum-well-structure laser diodes," *Appl. Phys. Lett.*, **68**, 3269 (1996).
7. S. Nakamura, "GaN-based blue/green semiconductor laser," *IEEE Selected Topics in Quantum Electronics*, **3**, 435 (1997).
8. I. Vurgaftman and J. R. Meyer, "Band parameters for nitrogen-containing semiconductors," *J. Appl. Phys.* **94**, 3675 (2003).
9. H. Amano, N. Sawaki, I. Akasaki, and Y. Toyoda, "Metalorganic vapor phase epitaxial growth of a high quality GaN film using an AlN buffer layer," *Appl. Phys. Lett.*, **48**, 353 (1986).
10. H. Amano, I. Akasaki, K. Hiramatsu, N. Koide, and N. Sawaki, "Effects of the buffer layer in metalorganic vapor phase epitaxy of GaN on sapphire substrate," *Thin Sol. Films*, **163**, 415 (1988).
11. S. Nakamura, "GaN growth using GaN buffer layer," *Jpn. J. Appl. Phys.*, **30**, L1705 (1991).
12. A. Usui, H. Sunakawa, A. Sakai, and A. A. Yamaguchi, "Thick GaN epitaxial growth with low dislocation density by hydride vapor phase epitaxy," *Jpn. J. Appl. Phys.*, **36**, L988 (1997).
13. S. Nakamura, M. Senoh, S. Nagahama, N. Iwasa, T. Yamada, T. Matsushita, H. Kiyoku, Y. Sugimoto, T. Kozaki, H. Umemoto, M. Sano, and K. Chocho, "InGaN/GaN/AlGaIn-based laser diodes with modulation-doped strained-layer superlattices," *Jpn. J. Appl. Phys.*, **36**, L1568 (1997).
14. H. Amano, M. Kito, K. Hiramatsu and I. Akasaki, "P-type conduction in Mg-doped

- GaN treated with low-energy electron beam irradiation (LEEBI)," *Jpn. J. Appl. Phys.*, **28**, L2112 (1989).
15. S. Nakamura, T. Mukai, M. Senoh, and N. Iwasa, "Thermal annealing effects on p-type Mg-doped GaN films," *Jpn. J. Appl. Phys.*, **31**, L139 (1992).
 16. Z. Sitar, M. J. Paisley, B. Yan, J. Ruan, W. J. Choyke, and R. F. Davis, "Growth of AlN/GaN layered structures by gas source molecular-beam epitaxy," *J. Vac. Sci. & Technol. B*, **8**, 316 (1990).
 17. I. D. Goepfert, E. F. Schubert, A. Osinsky, and P. E. Norris, "Demonstration of efficient p-type doping in $\text{Al}_x\text{Ga}_{1-x}\text{N}/\text{GaN}$ superlattice structures," *Electron Lett.*, **35**, 1109 (1999).
 18. P. Kozodoy, Y. P. Smorchkova, M. Hansen, H. Xing, S. P. DenBaars, U. K. Mishra, A. W. Saxler, R. Perrin, and W. C. Mitchel, "Polarization-enhanced Mg doping of AlGaIn/GaN superlattices," *Appl. Phys. Lett.*, **75**, 2444 (1999).
 19. I. Akasaki, H. Amano, K. Itoh, N. Koide, and K. Manabe, "GaN-based ultraviolet/blue light emitting devices," *Inst. Phys. Conf. Ser.*, **129**, 851 (1992).
 20. S. Nakamura, T. Mukai, and M. Senoh, "Candela-class high-brightness InGaIn/AlGaIn double-heterostructure blue-light-emitting diodes," *Appl. Phys. Lett.*, **64**, 1687 (1994).
 21. S. Nakamura, M. Senoh, N. Iwasa, and S. Nagahama, "High-brightness InGaIn blue, green and yellow light-emitting diodes with quantum well structures," *Jpn. J. Appl. Phys.*, **34**, L807 (1995).
 22. S. Nakamura, M. Senoh, N. Iwasa, S. Nagahama, T. Yamada, and T. Mukail, "Superbright green InGaIn single-quantum-well-structure light-emitting diodes," *Jpn. J. Appl. Phys.*, **34**, L1332 (1995).
 23. S. T. Yen and C. P. Lee, "Theoretical analysis of 630-nm band GaInP-AlGaInP strained quantum-well lasers considering continuum states," *IEEE J. Quantum Electron.*, **33**, 443 (1997).
 24. S. Strite and H. Morkoç, "GaN, AlN, and InN: A review," *J. Vac. Sci. Technol. B*, **10**, 1237 (1992).
 25. H. Morkoç, S. Strite, G. B. Gao, M. E. Lin, B. Sverdlov, and M. Burns, "Large-band-gap SiC, III-V nitride, and II-VI ZnSe-based semiconductor device technologies," *J. Appl. Phys.* **76**, 1363 (1994).
 26. S. Nakamura, M. Senoh, S. Nagahama, N. Iwasa, T. Yamada, T. Matsushita, Y. Sugimoto, and H. Kiyoku, "Optical gain and carrier lifetime of InGaIn multi-quantum well structure laser diodes," *Appl. Phys. Lett.* **69**, 1568 (1996).
 27. J. Y. Chang and Y. K. Kuo, "Simulation of blue InGaIn quantum-well lasers," *J. Appl. Phys.* **93**, 4992 (2003).
 28. M. Hansen, J. Piprek, P. M. Pattison, J. S. Speck, S. Nakamura, and S. P. Denbaars, "Higher efficiency InGaIn laser diodes with an improved quantum well capping configuration," *Appl. Phys. Lett.* **81**, 4275 (2002).

29. S. N. Lee, S. Y. Cho, H. Y. Ryu, J. K. Son, H. S. Paek, T. Sakong, T. Jang, K. K. Choi, K. H. Ha, M. H. Yang, O. H. Nam, Y. Park, and E. Yoon, "High-power GaN-based blue-violet laser diodes with AlGaIn/GaN multiquantum barriers," *Appl. Phys. Lett.* **88**, 111101-1 (2006).
30. S. P. Łepkowski and S. Krukowski, "Theoretical study of current overflow in GaN based light emitters with superlattice cladding layers," *J. Appl. Phys.* **100**, 016103-1 (2006).
31. S. Nakamura, M. Senoh, S. Nagahama, N. Iwasa, T. Yamada, T. Matsushita, Y. Sugimoto, and H. Kiyoku, "Room-temperature continuous-wave operation of InGaIn multi-quantum-well structure laser diodes with a lifetime of 27 hours," *Appl. Phys. Lett.* **70**, 1417 (1997).
32. S. Bidnyk, T. J. Schmidt, Y. H. Cho, G. H. Gainer, J. J. Song, S. Keller, U. K. Mishra, and S. P. DenBaars, "High-temperature stimulated emission in optically pumped InGaIn/GaN multiquantum wells," *Appl. Phys. Lett.* **72**, 1623 (1998).
33. Y.-H. Cho, J. J. Song, S. Keller, M. S. Minsky, E. Hu, U. K. Mishra, and S. P. DenBaars, "Influence of Si doping on characteristics of InGaIn/GaN multiple quantum wells," *Appl. Phys. Lett.* **73**, 1128 (1998).
34. M. Godlewski, V. Y. Ivanov, E. Usakowska, R. Boek, S. Miasojedovas, S. Jurnas, K. Kazlauskas, A. ukauskas, E. M. Goldys, M. R. Phillips, T. Bottcher, S. Figge, D. Hommel, "Influence of *n*-type doping on light emission properties of GaN layers and GaN-based quantum well structures," *Phys. Stat. Sol. (c)*, **2**, 1056 (2005).
35. S. Nakamura, T. Mukai, and M. Senoh, "Si-doped InGaIn films grown on GaN films," *Jpn. J. Appl. Phys.*, **32**, L16 (1993).
36. S. Keller, S. F. Chichibu, M. S. Minsky, E. Hu, U. K. Mishra, and S. P. DenBaars, "Effect of the growth rate and the barrier doping on the morphology and the properties of InGaIn/GaN quantum wells," *J. Cryst. Growth* **195**, 258 (1998).
37. P. Hacke, H. Nakayama, T. Detchprohm, K. Hiramatsu, and N. Sawaki, "Deep levels in the upper band-gap region of lightly Mg-doped GaN," *Appl. Phys. Lett.*, **68**, 1362 (1996)
38. M. Miyachi, T. Tanaka, Y. Kimura, and H. Ota, "The activation of Mg in GaN by annealing with minority-carrier injection," *Appl. Phys. Lett.*, **72**, 1101 (1998).
39. L. Sugiura, M. Suzuki, J. Nishio, K. Itaya, Y. Kokubun, and M. Ishikawa, "Characteristics of Mg-doped GaN and AlGaIn grown by H₂-ambient and N₂-ambient metalorganic chemical vapor deposition," *Jpn. J. Appl. Phys.*, **37**, 3878 (1998).
40. D. H. Youn, M. Lachab, M. Hao, T. Sugahara, H. Takenaka, Y. Naoi, and S. Sakai, "Investigation on the p-type activation mechanism in Mg-doped GaN films grown by metalorganic chemical vapor deposition," *Jpn. J. Appl. Phys.*, **38**, 631 (1999).
41. P. Kozodoy, H. Xing, S. P. DenBaars, Umesh K. Mishra, A. Saxler, R. Perrin, S. Elhamri, and W. C. Mitchel, "Heavy doping effects in Mg-doped GaN," *J. Appl. Phys.*,

- 87, 1832 (2000).
42. E. F. Schubert, W. Grieshaber, and I. D. Goepfert, "Enhancement of deep acceptor activation in semiconductors by superlattice doping," *Appl. Phys. Lett.* **69**, 3737 (1996).
 43. S. Nakamura, "InGaN multiquantum-well-structure laser diodes with GaN-AlGaN modulation-doped strained-layer superlattices," *IEEE Selected Topics in Quantum Electronics*, **4**, 483 (1998).
 44. K. Kumakura, and N. Kobayashi, "Increased electrical activity of Mg-acceptors in $\text{Al}_x\text{Ga}_{1-x}\text{N}/\text{GaN}$ superlattices," *Jpn. J. Appl. Phys.* **38**, L1012 (1999).
 45. P. Kozodoy, Y. P. Smorchkova, M. Hansen, H. Xing, S. P. DenBaars, U. K. Mishra, A. W. Saxler, R. Perrin, and W. C. Mitchel, "Polarization-enhanced Mg doping of AlGaN/GaN superlattices," *Appl. Phys. Lett.* **75**, 2444 (1999).
 46. L. Hsu, and W. Walukiewicz, "Theoretical transport studies of *p*-type GaN/AlGaN modulation-doped heterostructures," *Appl. Phys. Lett.* **74**, 2405 (1999).
 47. P. Kozodoy, M. Hansen, S. P. DenBaars, and U. K. Mishra, "Enhanced Mg doping efficiency in $\text{Al}_{0.2}\text{Ga}_{0.8}\text{N}/\text{GaN}$ superlattices," *Appl. Phys. Lett.* **74**, 3681 (1999).
 48. S. Heikman, S. Keller, Daniel S. Green, S. P. DenBaars, and U. K. Mishra, "High conductivity modulation doped AlGaN/GaN multiple channel heterostructures," *J. Appl. Phys.* **94**, 5321 (2003).
 49. M. Z. Kauser, A. Osinsky, A. M. Dabiran, and P. P. Chow, "Enhanced vertical transport in *p*-type AlGaN/GaN superlattices," *Appl. Phys. Lett.* **85**, 5275 (2004).
 50. A. Bykhovski, B. Gelmont, and S. Shur, "The influence of the strain-induced electric field on the charge distribution in GaN-AlN-GaN structure," *J. Appl. Phys.*, **74**, 6734 (1993).
 51. O. Ambacher, R. Dimitrov, M. Stutzmann, B.E. Foutz, M.J. Murphy, J.A. Smart, J.R. Shealy, N.G. Weimann, K. Chu, M. Chumbes, B. Green, A.J. Sierakowski, W.J. Schaff, and L.F. Eastman, "Role of spontaneous and piezoelectric polarization induced effects in group-III nitride based heterostructures and devices," *phys. Stat. sol. (b)*, **216**, 381 (1999).
 52. J. Bardeen, "An improved calculation of the energies of metallic Li and Na," *J. Chem. Phys.*, **6**, 367-371 (1938).
 53. F. Seitz, *The modern Theory of Solids*, McGraw Hill, New York, 1940, p. 352.
 54. S. L. Chuang and C. S. Chang, " $\mathbf{k} \cdot \mathbf{p}$ method for strained wurtzite semiconductors," *Phys. Rev. B*, **54**, 2491 (1996).
 55. M. G. Burt, "Direct derivation of effective-mass equations for microstructures with atomically abrupt boundaries," *Phys. Rev. B*, **50**, 7518 (1994).
 56. P. N. Stavrinou, and R. van Dalen, "Operator ordering and boundary conditions for valence-band modeling: Application to [110] heterostructures," *Phys. Rev. B*, **55**, 15456 (1997).
 57. F. Mireles and S. E. Ulloa, "Ordered Hamiltonian and matching conditions for

- heterojunctions with wurtzite symmetry: GaN/Al_xGa_{1-x}N quantum wells,” *Phys. Rev. B*, **60**, 13659 (1999).
58. G. E. Pikus and G. L. Bir, “Effects of deformation on the hole energy spectrum of germanium and silicon,” *Sov. Phys.-Solid State*, **1**, 1502 (1960).
 59. G. L. Bir and G. E. Pikus, *Symmetry and Strain-Induced Effects in Semiconductors*, Wiley, New York, 1974.
 60. T. T. Mnatsakanov, M. E. Levinshtein, L. I. Pomortseva, S. N. Yurkov, G. S. Simin, and M. A. Khan, “Carrier mobility model for GaN,” *S. S. Elec.*, **47**, 111 (2003).
 61. K. Kumakura, T. Makimoto, and N. Kobayashi, “Mg-acceptor activation mechanism and transport characteristics in *p*-type InGaN grown by metalorganic vapor phase epitaxy,” *J. Appl. Phys.*, **93**, 3370 (2003).
 62. S. M. Sze, *Physics of semiconductor devices*, 2nd Ed. (John Wiley & Sons, Inc, 1981), p. 520.
 63. B. Santic, “On the hole effective mass and the free hole statistics in wurtzite GaN,” *Semicond. Sci. Technol.*, **18**, 219 (2003).
 64. S. M. Sze, *Physics of semiconductor devices*, 2nd Ed. (John Wiley & Sons, Inc, 1981), p. 255.
 65. K. Horio, and H. Yanai, “Numerical modeling of heterojunctions including the thermionic emission mechanism at the heterojunction interface,” *IEEE Trans. Electron Devices*, **37**, 1093 (1990).
 66. J. S. Jang, T. Y. Seong, and S. R. Jeon, “Formation mechanisms of low-resistance and thermally stable Pd/Ni/Pd/Ru ohmic contacts to Mg-doped Al_{0.15}Ga_{0.85}N,” *Appl. Phys. Lett.*, **91**, 092129 (2007).
 67. C. M. Krowne, “Semiconductor heterostructure nonlinear Poisson equation,” *J. Appl. Phys.*, **65**, 1602 (1989).
 68. G. Martin, A. Botchkarev, A. Rockett, and H. Morkoç, “Valence-band discontinuities of wurtzite GaN, AlN, and InN heterojunctions measured by x-ray photoemission spectroscopy,” *Appl. Phys. Lett.* **68**, 2541 (1996).
 69. S. F. Chichibu, A. C. Abare, M. S. Minsky, S. Keller, S. B. Fleischer, J. E. Bowers, E. Hu, U. K. Mishra, L. A. Coldren, S. P. DenBaars, and T. Sota, “Effective band gap inhomogeneity and piezoelectric field in InGaN/GaN multiquantum well structures,” *Appl. Phys. Lett.* **73**, 2006 (1998).
 70. E. T. Yu, X. Z. Dang, P. M. Asbeck, S. S. Lau, and G. J. Sullivan, “Spontaneous and piezoelectric polarization effects in III-V nitride heterostructures,” *J. Vac. Sci. Technol. B*, **17**, 1742 (1999).
 71. L. H. Peng, C. W. Chuang, and L. H. Lou, “Piezoelectric effects in the optical properties of strained InGaN quantum wells,” *Appl. Phys. Lett.*, **74**, 805 (1999).
 72. H. Jiang, and J. Singh, “Gain characteristics of InGaN-GaN quantum wells,” *IEEE J. Quantum Electron.* **36**, 1058 (2000).

73. C. Wetzel, H. Amano, and I. Akasaki, "Piezoelectric polarization in GaInN/GaN heterostructures and some consequences for device design," *Jpn. J. Appl. Phys.*, **39**, 2425 (2000).
74. M. E. Aumer, S. F. Leboeuf, B. F. Moody, and S. M. Bedair, "Strain-induced piezoelectric field effects on light emission energy and intensity from AlInGaN/InGaN quantum wells," *Appl. Phys. Lett.*, **80**, 3803 (2001).
75. C. Y. Lai, T. M. Hsu, W. H. Chang, K. U. Tseng, C. M. Lee, C. C. Chuo, and J. I. Chyi, "Direct measurement of piezoelectric field in $\text{In}_{0.23}\text{Ga}_{0.77}\text{N}/\text{GaN}$ multiple quantum wells by electrotransmission spectroscopy," *J. Appl. Phys.* **91**, 531 (2002).
76. K. L. Bunker, R. Garcia, and P. E. Russell, "Scanning electron microscopy cathodoluminescence studies of piezoelectric fields in an InGaN/GaN quantum-well light-emitting diode," *Appl. Phys. Lett.* **86**, 082108 (2005).
77. S. Nakamura, "InGaN multiquantum-well-structure laser diodes with GaN-AlGaIn modulation-doped strained-layer superlattices," *IEEE J. Quantum Electron.* **4**, 483 (1998).
78. S. Nakamura, "InGaN-based violet laser diodes," *Semicond. Sci. Technol.* **14**, R27 (1999).
79. M. Vehse, P. Michler, J. Gutowski, S. Figge, D. Hommel, H. Selke, S. Keller and S. P. DenBaars, "Influence of composition and well-width fluctuations on optical gain in (In, Ga)N multiple quantum wells," *Semicond. Sci. Technol.*, **16**, 406 (2001).
80. F. D. Sala, A. D. Carlo, P. Lugli, F. Bernardini, V. Fiorentini, R. Scholz, and J. M. Jancu, "Free-carrier screening of polarization fields in wurtzite GaN/InGaN laser structures," *Appl. Phys. Lett.* **74**, 2002 (1999).
81. J. C. Harris, S. Kako, T. Someya, and Y. Arakawa, "Screening of the polarization field in InGaN single quantum wells," *Phys. Stat. Sol.* **216**, 423 (1999).
82. G. Franssen, T. Suski, and P. Perlin, "Fully-screened polarization-induced electric fields in blue/violet InGaN/GaN light-emitting devices grown on bulk GaN," *Appl. Phys. Lett.* **87**, 041109 (2005).
83. S. T. Yen, "Theory of resonant states of hydrogenic impurities in quantum wells," *Phys. Rev. B*, **66**, 075340 (2002).
84. S. Nagahama, T. Yanamoto, M. Sano and T. Mukai, "Wavelength dependence of InGaN laser diode characteristics," *Jpn. J. Appl. Phys.*, **40**, 3075 (2001).
85. S. H. Wei and A. Zunger, "Valence band splittings and band offsets of AlN, GaN, and InN," *Appl. Phys. Lett.* **69**, 2719 (1996).
86. C. Manz, M. Kunzer, H. Obloh, A. Ramakrishnan, and U. Kaufmann, " $\text{In}_x\text{Ga}_{1-x}\text{N}/\text{GaN}$ band offsets as inferred from the deep, yellow-red emission band in $\text{In}_x\text{Ga}_{1-x}\text{N}$," *Appl. Phys. Lett.* **74**, 3993 (1999).
87. Y. J. Wang, S. J. Xu, Q. Li, D. G. Zhao, and H. Yang, "Band gap renormalization and carrier localization effects in InGaN/GaN quantum-wells light emitting diodes with Si

- doped barriers,” *Appl. Phys. Lett.*, **88**, 041903 (2006).
88. S. T. Yen and C. P. Lee, “Effects of doping in the active region of 630-nm band GaInP-AlGaInP-tensile-strained quantum-well lasers,” *IEEE Quantum Electron.*, **34**, 1644 (1998).
 89. K. Kumakura, T. Makimoto, and N. Kobayashi, “Enhanced hole generation in Mg-doped AlGaIn/GaN superlattices due to piezoelectric field,” *Jpn. J. Appl. Phys.*, **39**, 2428 (2000).
 90. O. Ambacher, J. Smart, J. R. Shealy, N. G. Weimann, K. Chu, M. Murphy, W. J. Schaff, L. F. Eastman, R. Dimitrov, L. Wittmer, M. Stutzmann, W. Rieger, and J. Hilsenbeck, “Two-dimensional electron gases induced by spontaneous and piezoelectric polarization charges in N- and Ga-face AlGaIn/GaN heterostructures,” *J. Appl. Phys.*, **85**, 3222 (1999).
 91. O. Ambacher, B. Foutz, J. Smart, J. R. Shealy, N. G. Weimann, K. Chu, M. Murphy, A. J. Sierakowski, W. J. Schaff, L. F. Eastman, R. Dimitrov, A. Mitchell, and M. Stutzmann, “Two dimensional electron gases induced by spontaneous and piezoelectric polarization in undoped and doped AlGaIn/GaN heterostructures,” *J. Appl. Phys.*, **87**, 334 (2000).
 92. E. L. Waldron, J. W. Graff, and E. F. Schubert, “Improved mobilities and resistivities in modulation-doped *p*-type AlGaIn/GaN superlattices,” *Appl. Phys. Lett.*, **80**, 2737 (2001).
 93. C. T. Foxon, S. V. Novikov, L. X. Zhao, and I. Harrison, “Isoelectronic doping of AlGaIn alloys with As and estimates of AlGaIn/GaN band offsets,” *Appl. Phys. Lett.*, **83**, 1166 (2003).
 94. V. W. L. Chin, T. L. Tansley, and T. Osotchan, “Electron mobilities in gallium, indium, and aluminum nitrides,” *J. Appl. Phys.*, **75**, 7365 (1994).

Vita

Name : Shyh-Jer Huang (黃士哲)

Date of birth : Apr. 8, 1976

Sex : Male

Education :

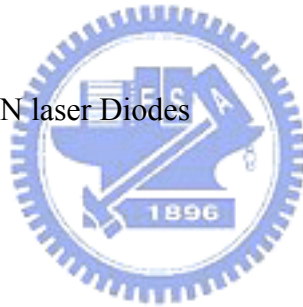
National Chiao Tung University Ph. D. September, 2002 ~ January, 2008
Institute of Electronics Engineering

National Chiao Tung University M. S. September, 1999 ~ June, 2001
Institute of Electronics Engineering

National Chung Cheng University B. S. September, 1994 ~ June, 1998
Department of Electrical Engineering

Title of Ph D. Dissertation :

Theoretical Study of InGaN/GaN laser Diodes



Publication List

Journal papers (SCI):

- [1] C. M. Kwei, **S. J. Hwang**, Y. C. Li, and C. J. Tung, “Energy losses of charged particles moving parallel to the surface of an overlayer system,” *J. Appl. Phys.*, **93**, p.9130 (2003).
- [2] **S. J. Huang**, and S. T. Yen, “Electron spillover effects in InGaN/GaN quantum-well lasers,” *J. Appl. Phys.*, **102**, p.113112 (2007)
- [3] **S. J. Huang**, and S. T. Yen, “Improvement in threshold of InGaN/GaN quantum-well lasers by *p*-type modulation doping,” *J. Appl. Phys.*, **102**, p.113103 (2007).

Letter paper (SCI):

- [1] M. C. Lo, **S. J. Huang**, C. P. Lee, S. D. Lin, and S. T. Yen, “Discrete monolayer light emission from GaSb wetting layer in GaAs,” *Appl. Phys. Lett.*, **90**, 243102 (2007).

Conference paper:

- [1] **S. J. Huang**, Y. C. Chen, and S. T. Yen, “Theoretical analysis of *p*-type $\text{Al}_x\text{Ga}_{1-x}\text{N}/\text{GaN}$ superlattices for low vertical resistivity,” ODF’06, Japan (2006).

Submitted paper (SCI):

- [1] **S. J. Huang**, S. T. Yen, and Y. C. Chen, “Theoretical analysis of *p*-type AlGaIn/GaN superlattices for low vertical resistivity,” *J. Appl. Phys.*

